People's Democratic Republic of Algeria
Ministry of Heigher Education and Scientific Research
University of Kasdi Merbah Ouargla
Faculty of Mathematics and Matter Sciences
Department of Physics

**THESIS**
**To obtained the diploma of:**
**3rd cycle DOCTORATE**
**Specialty: Physics**
**Option: Physics of materials**
**Presented by :**
**Noura MEBROUKI**
**Entitled**

# Synthesis of new piezoelectric materials based on natural resources (rocks) of Ouargla region

**Discussed publicly on: 24/10/2023**

**The jury composed of:**

| | | |
|---|---|---|
| Mohammedi Lazhar / Pr. | Kasdi Merbah University - Ouargla | President |
| Achouri Abderrahim /MCA | Kasdi Merbah University - Ouargla | Examiner |
| Mefteh Nassima /MCA | Hamma Lakhdar University - Eloued | Examiner |
| Benkrima Yamina /MCA | ENS – Ouargla | Examiner |
| Benmebrouk Lazhar /Pr. | Kasdi Merbah University - Ouargla | Supervisor |
| Zenkheri Louiza /Pr. | Kasdi Merbah University - Ouargla | Co-Supervisor |

**Academic year: 2022/2023**

# Dedication

To

My dearest people in my life,

My parents and Aymen,

My brother Taruk,

My brother Rayan,

My sister Afaf,

My sister Sabah,

My sisters Soulaf, and Soudjoud,

My niece Ritaj,

The whole family,

All my friends,

Noura Mebrouki

# Ackownldegment

*A doctoral thesis is often described as an individual work.*

*But*

*the long list below definitely proves the contrary!*

First of all, I thank God, Almighty, for giving me the strength to survive and the courage to overcome all difficulties, to have guided me to this adventure a stimulating and enriching experience at the professional and personal. Almighty God said, **"If you count the blessings of Allah, you cannot to stop the number! Allah is Absolutor and All Merciful" (AN-NAHL 18).**

It is my duty to express my deep gratitude to thank everyone who has helped this work come to fruition

Words of recognition…

My gratitude goes first to Mr. Lazhar Benmebrouk, for having accepted the supervision of my doctoral thesis as director of this work and professor teacher and responsible for our training from the Magisterium (Material physics 2018). I would like to thank him for his advice, his humanism, the clarity of his ideas help me to get through this work.

To my co-supervisor Louiza Zenkhri, Professor at the department of chemistry at Kasdi Merbah Ouargla University, for its encouragement and his advice, and for her explanations that helped me to develop the method of this research, her incessant encouragement and especially its great availability throughout the realization of this work.  I thank her for the trust she has shown me and especially for her wise advice, which contributed to my reflection. It is my duty to show my gratitude.

I am extremely grateful to Mr. Mohammed Lakhder Belfar Professor and boss of chemistry department at Kasdi Merbah Ouargla University, for his wise advice, and made me the honour and the courage to develop this work for having responded to my correspondence and for his invaluable help.

A deep thank also to Mr. Salah Tlili Lecturer Class A at Kasdi Merbah Ouargla University, for his encouragement, and his explanations and orientations on several aspects of this research that helped me to develop the method of my study. His wise advice regarding the various techniques of characterization samples, may he find here an expression of my great respect and gratitude.

« *I am grateful to all those*

*who*

*told me no. It's thanks to them I am myself»*


*Albert Einstein*

# Contents

# Contents

# Abreviations list

| List of acronymes | |
|---|---|
| OH | Ouargla-Hassi Messaoud |
| FT-IR | Fourier-transform infrared |
| EDS | Energy dispersive X-ray |
| SEM | Scanning electron microscopy |
| XRD | X-ray diffraction |
| Kv | Kilo Volts |
| CuKα | Anode radiation |
| Nm | Nanometer |
| °C | Celsius |
| A° | Angström |
| Ө | The diffraction angle |
| Λ | The used wavelength |
| N | The order of diffraction |
| $d_{hkl}$ | Inter-planar spacing |
| (h k l) | The Miller indexes |
| 'a', 'b', 'c' | The lattice constants |
| B | The width full at half maximum (FWHM) |
| D | The crystallite size |
| COD | Crystallography Open Database |
| ICSD | Inorganic Crystal Structure Database |

# List of Tables

## List of Figures

## Abstract

The piezoelectric thin films were prepared by hydrothermal synthesis in using sandstones (OH1-OH7) as source of metallic cations as a precursor which collected from the southeast part of Algeria (Ouargla). First we investigated a quantative and qualitative analytical study of sandstones. The seven sample's Fourier-transform infrared (FT-IR) spectra showed the distinctive vibration bond peaks proving the existence of quartz and calcite. Whereas, Raman measurements indicated only the maximum acute values in intensity appeared at approximately 500 cm$^{-1}$ before 600 cm$^{-1}$ of the rotation of a part containing carbon atoms. Additionally, the chemical composition of sandstones was examined by energy dispersive X-ray (EDS) and X-ray diffraction (XRD), which generally revealed a composition with an average major content of 86.86% quartz in α-phase and a minor content of 13.14% calcite (CaCO$_3$). Six samples of sandstones containing trace amounts of Fe, Al, Ag, Na, and K, these samples characterize by a solid solution in the crystal lattice, according to the EDS analysis. To create the thin films, silicon and calcium were extracted from the rock samples using the aqua regia digestion technique. As for the characterization of thin films, we used the same techniques but with a various type of devices. The thin films characterization were found mainly consist of about 9.33% quartz in α-phase and calcite mineral (about 90.66%). Finally, the piezoelectric measurements gave the strongest piezoelectric coefficients values of crystal quartz in rocks and thin films which are $d_{33} = 2.55 \pm 0.1$ pC/N for (71% of SiO$_2$), $d_{33} = 4.18 \pm 0.1$ pC/N for (69% of SiO$_2$), respectively. The obtained results shown here are very compatible with that was determined in previous studies.

**Keywords:** Sandstones, piezoelectric thin films, hydrothermal synthesis, X-rays diffraction, SEM-EDS spectroscopy, FT-IR spectroscopy.

# Résume

Les couches minces piézoélectriques ont été préparées par synthèse hydrothermale en utilisant des grès (OH1-OH7) comme source de cations métalliques comme précurseur qui se sont recueillis dans la partie sud-est de l'Algérie (Ouargla). Nous avons d'abord étudié une étude analytique quantitative et qualitative des grès. Les sept spectres infrarouges à transformation de Fourier (FT-IR) de l'échantillon ont montré les pics de liaison vibratoire distinctifs prouvant l'existence du quartz et de la calcite. Alors que les mesures Raman indiquaient seulement les valeurs aiguës maximales en intensité apparaissaient à environ 500 cm$^{-1}$ avant 600 cm$^{-1}$ de la rotation d'une partie contenant des atomes de carbone. De plus, la composition chimique des grès a été examinée par diffusion d'énergie aux rayons X (EDX) et par diffraction aux rayons X (DRX), qui ont généralement révélé une composition avec une teneur majeure moyenne de 86.86% de quartz en phase α et une teneur mineure en calcite à 13.14% ($CaCO_3$). Six échantillons de grès contenant des traces de Fe, Al, Ag, Na et K, ces échantillons se caractérisent par une solution solide dans le réseau cristallin, selon l'analyse EDX. Pour créer les couches minces, le silicium et le calcium ont été extraits des échantillons de roche en utilisant la technique de digestion aqua regia. En ce qui concerne la caractérisation des couches minces, nous avons utilisé les mêmes techniques mais avec différents types de dispositifs. La caractérisation des couches minces se compose principalement d'environ 9.33% de quartz en phase α et minéral de calcite (environ 90.66%). Enfin, les mesures piézoélectriques ont donné les coefficients piézoélectriques les plus élevés de quartz cristallin dans les roches et les couches minces sont $d_{33}$ = 2,55 ± 0,1 pC/N pour (71% de $SiO_2$), $d_{33}$ = 4,18 ± 0,1 pC/N pour (69% de $SiO_2$), respectivement. Les résultats obtenus présentés ici sont très compatibles avec ceux déterminés dans les études précédentes.

**Mots-clés :** Grès, couches minces piézoélectriques, synthèse hydrothermale, diffraction des rayons X, spectroscopie MEB-EDX, spectroscopie FT-IR.

**الملخص**

تم إعداد الأغشية الرقيقة الكهروضغطية عن طريق التخليق الحراري المائي باستخدام الأحجار الرملية (OH1-OH7) كمصدر للكاتيونات المعدنية كسلائف تم جمعها من جنوب شرق الجزائر (ورقلة). قمنا أولاً بدراسة تحليلية كمية ونوعية للأحجار الرملية. أظهرت أطياف الأشعة تحت الحمراء لتحويل فورييه (FT-IR) للعينات السبعة قمم الارتباط الاهتزازي المميزة التي تثبت وجود الكوارتز والكالسيت. في حين أن قياسات رامان أشارت فقط إلى القيم الحادة القصوى في الشدة ظهرت حوالي 500 سم $^{-1}$ قبل 600 سم $^{-1}$ من دوران جزء يحتوي على ذرات الكربون. بالإضافة إلى ذلك، تم فحص التركيب الكيميائي للأحجار الرملية عن طريق انتشار طاقة الأشعة السينية (EDS) وحيود الأشعة السينية (XRD)، والتي كشفت عمومًا عن تكوين بمتوسط محتوى رئيسي يبلغ 86.86٪ كوارتز في المرحلة α ومحتوى ثانوي من الكالسيت يقدر بـ 13.14 ٪ (CaCO$_3$). تتميز ست عينات من الحجر الرملي تحتوي على آثار Fe و Al و Ag و Na و K، بمحلول صلب في الشبكة البلورية، وفقًا لتحليل EDS. لإنشاء الأغشية الرقيقة، تم استخراج السيليكون والكالسيوم من عينات الصخور باستخدام تقنية هضم الريجيا المائية. فيما يتعلق بتوصيف الأغشية الرقيقة، استخدمنا نفس التقنيات ولكن مع أنواع مختلفة من الأجهزة. يتكون توصيف الأغشية الرقيقة بشكل أساسي من حوالي 9.33٪ كوارتز في المرحلة α ومعدن الكالسيت (حوالي 90.66٪). أخيرًا، أعطت القياسات الكهروضغطية أعلى معاملات كهروضغطية للكوارتز البلوري في الصخور والأغشية الرقيقة (71٪ SiO$_2$) لـ $d_{33} = 2.55 \pm 0.1$ pC/N، $d_{33} = 4.18 \pm 0.1$ pC/N، (69٪ SiO$_2$)، على التوالي. النتائج التي تم الحصول عليها و الموضحة هنا متوافقة جدا مع ما تم تحديده في الدراسات السابقة.

**الكلمات الرئيسية:** الأحجار الرملية، الأغشية الرقيقة الكهروضغطية، التركيب الحراري المائي، حيود الأشعة السينية، التحليل الطيفي SEM-EDS، التحليل الطيفي FT-IR

# General Introduction
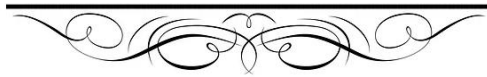
# General Introduction

Humans have always had a relationship with rocks since the beginning of time as they used them to create many useful things like: knives, plates … etc and they are found everywhere. In the vast deserts, there are numerous minerals and natural resources (rocks) with a unique geological source, which have been seen; these minerals have undergone geomorphological geological investigations that have looked at the types and shapes of rocks [1]. Rocks come in a limitless range of hues from shiny dazzling to dreary dark, they have a wide range of hues as a result of several reasons [2]. The earth's crustal rocks, which are essentially a collection of different minerals, are thought to be the source of minerals. Depending on their way of origin, they can be generally divided into three groups: the rocks that are igneous, metamorphic, and sedimentary [3]. Similar to igneous rocks, sedimentary rocks are composed of a fairly limited number of minerals, including quartz, carbonates, clay and feldspar. Construction, industry, agricultural technology and cosmetics are all supported by minerals [4].

Why is general rock science fascinating? In an effort to pique interest in the most recent area of research. In the fields of geophysics, geology or earth sciences, studying rocks for a variety of purposes is interesting. To determine how specific regions were formed or to determine a region's stability, such as if it is susceptible to environmental issues like radiation, scientists study the rocks [5]. To measure the concentration of naturally occurring radionuclides in rock samples, many investigations have been conducted in numerous nations [6]. The characteristics of rocks have been studied using a variety of techniques in materials science or material physics [7-9] in both microstructure and macrostructure, which can describe the physical characteristics of rocks [10, 11] and structural properties [5, 12-14]. Additionally, knowledge of rock minerals will reveal the characteristics of rocks [15].

Calcite, aragonite and vaterite are three distinct crystalline forms of calcium carbonate ($CaCO_3$), one of the most prevalent substances in the world [16]. Scientists are still interested in the orthorhombic polymorph of $CaCO_3$ 95 years after W. L. Bragg determined its first structure in 1924 [17]. This is caused by aragonite's widespread abundance and significant function in geochemistry, particularly in the process of biomineralization [18]. The space group of calcite structure is R3c [19]; descriptions on the fabrication of its thin film can be found in [20-22]. Calcite is a mineral that can be found in hydrothermal and secondary mineralization as well as metamorphic and igneous rocks, is significant in sedimentary contexts. Due to their occurrence in many geological contexts, aragonite and calcite are of interest [23].

Silicon and oxygen are two of the most prevalent elements in the Earth's crust, which together make up quartz ($SiO_2$). Quartz can be found as either the α-quartz or β-quartz polymorph [24]. Quartz is a mineral that occurs in subsurface hydrothermal veins at temperatures between 250 and 450°C and molten magma at approximately 800°C. The literature states that there are numerous ways to create quartz thin films [26-28]. Since quartz is chemically very near to being 100% $SiO_2$, its crystal lattice can only included a few elements [29-32]. To employ trace elements for genetic interpretations due to the widespread presence of quartz in igneous, metamorphic and sedimentary rocks, numerous attempts have been made [33-36].

In particular, α-quartz is frequently employed in electronic applications because of its piezoelectric capabilities, which enable the creation of extremely selective filters and excellent frequency control in oscillators [37]. The piezoelectric property of quartz is one of its attributes [27] and it has been researched by looking at the opposite piezoelectric effect. Quartz has had its piezoelectric constant measured across the specimen from point to point [38]. Additionally, M.P. Volarovich and E.1. Parkhomenko found the piezoelectric effects in rocks in 1954 [39]. On the basis of the idea put out [40], A. V. Shubnikov also provided an explanation for the piezoelectric action in polycrystals (rocks). In geophysics, the piezoelectric effect of rocks is frequently employed. Currently, to our knowledge, there is no theory or statistical model that describes how piezoelectric active texturized rocks are created. This is due to a dearth of experimental data and a lack of knowledge on the relationships between the circumstances and processes involved in the formation of rocks and the piezoclectric properties of rocks [41].

## Research objectives

In this study, we did a quantitative and qualitative analytical study of a group of rocks collected from Ouargla region. After identifying their chemical components, we worked to extract their elements in the synthesize of $CaCO_3/SiO_2$ thin films on glass substrate using a hydrothermal reactor at different temperatures, took place using electric oven for 2 hours, in order to prepare new piezoelectric materials in thin films form that may be used in electronic fields, due to its pricey chemical components, which are also safe for human health and the environment. In this work, we will carry out a complementary study of the measurements piezoelectric coefficient of the quartz phase in rocks and in thin films.

To comprehend the variations seen in the experimental work more fully, a certain number of samples were carried out at the level of Radiation and Plasmas and Surface Physics

Laboratory (LRPPS), Kasdi Merbah University of Ouargla, the center for Scientific and Technical Research in Physico-Chemical Analysis (CRAPC) Ouargla, Algeria. Thin film laboratory, Mohamed Khider University of Biskra, Algeria; Sahara geology Laboratory (E1521600) Address BP 511 avenue of Ghardaia, Ouargla, Algeria; DAC-HR University of Setif 1, Algeria. These samples were characterized also at Applied Physics Laboratory, Faculty Sciences of Sfax (Tunisia).

## The chosen method

Hydrothermal reactor (synthesis) is most often used to synthesis thin films, that uses reactions in homogeneous or heterogeneous phase in aqueous medium at high temperature and pressure to crystallize materials directly from solution.

The experimental measurement method used in our study, known as hydrothermal method, the thin films synthesis was carried out in the autoclave (Figure II.6, Annex 1). The advantages of this method are a higher synthesis temperature (our maximum hydrothermal temperature is 500°C) and temperature control, but its disadvantages are the internal pressure, which depends on the nature of the solvent and a significant temperature gradient.

## Potential applications

From the point of view of technical and economic requirements, the focus of the research work and production at lower cost, are at the origin of the discovery of new high-performance materials. The results of this work will certainly help to produce new materials for future use in science research.

Calcium carbonate ($CaCO_3$), which is produced in huge quantities by living things and is an essential building block for the development of innovative materials in a variety of industries, is one of the most explored systems [42-44]. $CaCO_3$ is one of the most prevalent biological minerals in nature, also $CaCO_3$ has a wide range of industrial uses, including the production of pigments, paper, plastics, rubbers and other materials [45].

Additionally, calcium carbonate ($CaCO_3$) thin films have the potential to be used as models for biosensors, photo-catalysts and bone replacement biomaterials. $CaCO_3$ is used extensively in industry, particularly as a filler and in the production of lime and cement as well as construction aggregates. $CaCO_3$ is one of the most promising materials for bone regeneration and replacement, according to Green et al., compared to calcium phosphate, calcium carbonate is quickly resorbed and replenished by natural bone [46]. $CaCO_3$ has been shown by Westbroek et al., to increase osteoblast activity, which aids in the growth of new

bone [47]. As bone replacement materials, calcium carbonate thin film has been reported by Sommerdijk et al. [48]. Despite the widespread use of calcite thin films, little attention has been paid to them and there are very few reports in the literature that study them. The current work's scope is widened by this.

Due to its numerous of potential physical and chemical characteristics, including its biocompatibility, low bulk density, hydrophobicity, electrical insulation, high thermal stability and large surface area over the past two decades, silica material ($SiO_2$) has drawn particular attention. A wide variety of applications, including glass, optics, photonics …. use quartz [49-51]. High purity siliceous materials ($SiO_2 > 99\%$) are now used in a variety of industries, including semiconductors, high-temperature lamp tubing, telecommunications and optics, microelectronics and particularly photovoltaic silicon applications [52].

The non-crystallized silica used to make optical instruments, laboratory equipment and glass fiber is known as "silica glass." One of the best electrical isolators now in use is silica. This is why it is frequently used on silicon electrical circuits by simply oxydating the desired layers. [53]. Contrarily, due to its superior properties, quartz single crystal has been widely used for a variety of electronic and optical devices, including oscillators and wave guides [54-58].

Quartz thin films have great potential technological thanks to their specific properties (high chemical stability, high refraction, transparency in the visible …..) which allow their use as optical, optoelectronic components, electronic support, integrated amplifiers and in alternating multilayer structure ($TiO_2$-$SiO_2$) in the manufacture of optical microcavities with Bragg mirrors [59]. (These about quartz)

Piezoelectric quartz crystal oscillators have had broad utilization in applied physics, chemistry, surface science, and many other areas of technology. Piezoelectric quartz crystals are used by periodic mechanical surface profiling to measure the melting kinetics of thin films [60]. Whereas, piezoelectric quartz-crystal resonators use to the viscoelastic characterization of thin organic layers [61], also an important application of quartz crystal resonators is the quartz crystal microbalance (QCM)[62], in addition low α-quartz piezoelectric thin films use in the fields of sensors and information technologies [63].

## Thesis structure

There are three parts in this thesis, the first part can be considered as a general introduction that gives general information on rocks and their types,

calcite and quartz and their application, the objectives of our research, the methodology used, the second part is dedicated to the theoretical study rock types and thin films of calcite/quartz and their previous study, also the piezoelectricity and piezoelectric materials and finally the last part is divided to experimental procedures and characterization techniques and concluded with the investigation of the characterization.

We have listed a quick summary of what each chapter covers below.

## Chapter I | Definition and Literature Review

In the first chapter, we provide the theoretical background necessary for the understanding of this thesis. We began with an overview of the definitions of rocks and piezoelectric materials. After a brief introduction to the type of rocks, we discussed the formation of sandstone, specifically the quartz-calcite and their physical properties. Finally, we reviewed mechanism of the production of thin films and process of thin films growth.

## Chapter II | Material and Methods

This chapter is divided to the material and methods, experimental procedure, media touls and characterization techniques.

## Chapter III | Characterization of rocks

This chapter review of the third part of this thesis, we will present the different characterization methods applied to study and characterize the rock samples by using Raman spectroscopy, Fourier-transform infrared spectroscopy (FT-IR), energy dispersive X-ray (EDS) and X-ray diffraction (XRD) and their piezoelectric properties. Then we discussed the results.

## Chapter IV | Synthesis and characterization of thin films

In this last chapter, we will present the method of elaboration by hydrothermal synthesis and we will present a complete description of the assembly experimental used. The most important part of our contribution 'the results and their discussions' will come next. The latter is divided into several sections, including the raw results obtained by using Fourier-transform

infrared spectroscopy (FT-IR), scanning electron microscopy (SEM-EDS) and X-ray diffraction (XRD) of synthesis thin films based on rocks, and their piezoelectric properties. Finally, we conclude this thesis and identify possible research perspectives.

# Reference
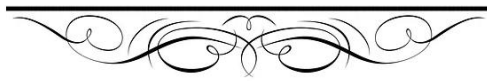
# Reference

[1] Nayak, P. S. and B. Singh (2007). "Instrumental characterization of clay by XRF, XRD and FTIR." Bulletin of materials science 30(3): 235-238.

[2] Sabri, M. M. (2020). "Chemical and structural analysis of rocks using X-ray fluorescence and X-ray diffraction techniques." ARO-The Scientific Journal of Koya University 8(1): 79-87.

[3] J. A. Aidekoya, J. A. (1995) Negative Environmental Impact Of Mineral Exploitation In Nigeria. International Journal of Physics Science (613).

[4] King, H. "Mineral and chemical composition of pure limestone-Missouri Department of Natural Resources., 2005-2015." Geology. com.

[5] Al-Ghamdi, A. (2019). "X-ray diffraction and gamma-ray analysis of rock samples from Haradh Region in Saudi Arabia." Journal of Radiation Research and Applied Sciences 12(1): 87-92.

[6] Masok, F., P. Masiteng, et al. (2018). "Measurement of radioactivity concentration in soil samples around phosphate rock storage facility in Richards Bay, South Africa." Journal of Radiation Research and Applied Sciences 11(1): 29-36.

[7] Rahman, T., M. Lebedev, et al. (2017). "Influence of rock microstructure on its electrical properties: an analysis using X-ray microcomputed tomography." Energy Procedia 114: 5023-5031.

[8] Al-Yaseri, A. Z., M. Lebedev, et al. (2015). "Pore-scale analysis of formation damage in Bentheimer sandstone with in-situ NMR and micro-computed tomography experiments." Journal of Petroleum Science and Engineering 129: 48-57.

[9] Zandomeneghi, D., M. Voltolini, et al. (2010). "Quantitative analysis of X-ray microtomography images of geomaterials: Application to volcanic rocks." Geosphere 6(6): 793-804.

[10] Arif, M., A. Barifcani, et al. (2017). "Impact of solid surface energy on wettability of $CO_2$-brine-Mineral systems as a function of pressure, temperature and salinity." Energy Procedia 114: 4832-4842.

[11] Rahman, T., M. Lebedev, et al. (2016). "Residual trapping of supercritical $CO_2$ in oil-wet sandstone." Journal of colloid and interface science 469: 63-68.

[12] AL-Homadi, R. I. and I. S. Al-Okli (2018). "The Effect of Dolomitization on Mergi Formation Sequences (Cenomanian-Early Turonian) at The Type Section, Northern Iraq." مجلة دراسات موصلية: 149-164.

[13] Mohammed, T. A. M. (2012). "Composition and phase mineral variation of Portland cement in Mass Factory Sulaimani Kurdistan Region NE-Iraq." International Journal of Basic and Applied Sciences 12: 109-118.

[14] McKeown, D. A. and J. E. Post (2001). "Characterization of manganese oxide mineralogy in rock varnish and dendrites using X-ray absorption spectroscopy." American Mineralogist 86(5-6): 701-713.

[15] Setiawan, M. R., M. Iqbal, et al. (2019). "Mineral analysis in rocks using XRD and Petrography." Journal of Science and Applicative Technology 2(1): 206-214.

[16] Bang, J.H. and Jang, Y. N, et al.(2011). Effects Of Sodium Laurylsulfate On Crystal Structure Of Calcite Formed From Mixed Solutions. Journal of colloid and interface science ( 1) 356.

[17] Bragg, W. L. (1924). "The structure of aragonite." Proceedings of the Royal Society of London. Series A, Containing Papers of a Mathematical and Physical Character 105(729): 16-39.

[18] Caspi, E. a. N., B. Pokroy, et al. (2005). "On the structure of aragonite." Acta Crystallographica Section B: Structural Science 61(2): 129-132.

[19] Maslen, E., V. Streltsov, et al. (1993). "X-ray study of the electron density in calcite, $CaCO_3$." Acta Crystallographica Section B: Structural Science 49(4): 636-641.

[20] Miyauchi, S., H. Imoto, et al. (2016). "Fabrication of polymer-calcite composite thin films by phase transition of vaterite composite particles with octacarboxy-terminated T8-caged silsesquioxane." Polymer Journal 48(10): 1019-1027.

[21] Gower, L. B. (2008). "Biomimetic model systems for investigating the amorphous precursor pathway and its role in biomineralization." Chemical reviews 108(11): 4551-4627.

[22] Tanaka, Y. and K. Naka (2010). "A carbonate controlled-addition method for size-controlled calcium carbonate spheres by carboxylic acid-terminated poly (amidoamine) dendrimers." Polymer Journal 42(8): 676-683.

[23] Antao, S. M. and I. Hassan (2010). "Temperature dependence of the structural parameters in the transformation of aragonite to calcite, as determined from in situ synchrotron powder X-ray-diffraction data." The Canadian Mineralogist 48(5): 1225-1236.

[24] Spearing, D. R., I. Farnan, et al. (1992). "Dynamics of the $\alpha$-$\beta$ phase transitions in quartz and cristobalite as observed by in-situ high temperature $^{29}$Si and $^{17}$O NMR." Physics and Chemistry of Minerals 19: 307-321.

[25] Mason, B. and L. G. Berry (1968). Elements of mineralogy.

[26] Okudera, H. and A. Hozumi (2003). "The formation and growth mechanisms of silica thin film and spherical particles through the Stöber process." Thin Solid Films 434(1-2): 62-68.

[27] Carretero-Genevrier, A., M. Gich, et al. (2013). "Soft-chemistry–based routes to epitaxial $\alpha$-quartz thin films with tunable textures." Science 340 (6134): 827-831.

[28] Drisko, G. L. and Genevrier, A. C, et al. (2014). Advanced Function Mater(24) 5494.

[29] Götze, J., M. Plötze, et al. (2004). "Trace element incorporation into quartz: A combined study by ICP-MS, electron spin resonance, cathodoluminescence, capillary ion analysis, and gas chromatography." Geochimica et Cosmochimica Acta 68(18): 3741-3759.

[30] Rusk, B. G., M. H. Reed, et al. (2006). "Intensity of quartz cathodoluminescence and trace-element content in quartz from the porphyry copper deposit at Butte, Montana." American Mineralogist 91(8-9): 1300-1312.

[31] Jourdan, A.-L., T. W. Vennemann, et al. (2009). "Evidence of growth and sector zoning in hydrothermal quartz from Alpine veins." European Journal of Mineralogy 21(1): 219-231.

[32] Lehmann, K., A. Berger, et al. (2009). "Growth related zonations in authigenic and hydrothermal quartz characterized by SIMS-, EPMA-, SEM-CL-and SEM-CC-imaging." Mineralogical Magazine 73(4): 633-643.

[33] Bambauer, H. v. (1961). "Spurenelementgehalte und Ɣ-Farbzentren in Quarzen aus Zerrkluften der Schweizer Alpen."Schweizerische mineralogische und petrographische Mitteilungen 41: 335-369.

[34] Dennen, W. (1967). "Trace elements in quartz as indicators of provenance." <u>Geological Society of America Bulletin</u> 78(1): 125-130.

[35] Walenczak, Z. (1969). "Geochemistry of minor elements dispersed in quartz (Ge, Al, Ga, Fe, Ti, Li and Be)." <u>Archiwum Mineralogiezne</u> 28: 189-335.

[36] Lyakhovich, V. (1972). "Trace elements in rock-forming minerals of granitoids." <u>Izd. Nedra, Moscow</u> 200.

[37] Bottom, V. (1982). "Introduction to quartz crystal unit design Van Nostrand Reinhold Co." <u>New York</u>.

[38] Fox, G. W. and G. A. Fink (1934). "The piezoelectric properties of quartz and tourmaline." <u>Physics</u> 5(10): 302-306.

[39] Volarovich, M. and E. Parkhomenko (1954). <u>Piezoelectric effect of rocks</u>. Dokl. Acad. Sci. USSR.

[40] Shubnikov, A. V. (1946). Piezoelectric Textures, Moscow-Leningrad : Izd-Vo An Ussr, 99.

[41] Nikitin, A. N. and Ivankina, T. I. (1995). On the possible mechanisms of the formation of piezoelectric active rocks with crystallographic textures. Textures and microstructures, (25) 33 (1995).

[42] Kato, T., A. Sugawara, et al. (2002). "Calcium carbonate–organic hybrid materials." <u>Advanced Materials</u> 14(12): 869-877.

[43] Naka, K. and Y. Chujo (2001). "Control of crystal nucleation and growth of calcium carbonate by synthetic substrates." <u>Chemistry of Materials</u> 13(10): 3245-3259.

[44] Sommerdijk, N. A. and G. d. With (2008). "Biomimetic CaCO3 mineralization using designer molecules and interfaces." <u>Chemical reviews</u> 108(11): 4499-4550.

[45] Dalas, E., P. Klepetsanis, et al. (1999). "The overgrowth of calcium carbonate on poly (vinyl chloride-co-vinyl acetate-co-maleic acid)." <u>Langmuir</u> 15(23): 8322-8327.

[46] Green, D., D. Walsh, et al. (2002). "The potential of biomimesis in bone tissue engineering: lessons from the design and synthesis of invertebrate skeletons." <u>Bone</u> 30(6): 810-815.

[47] Westbroek, P. and F. Marin (1998). "A marriage of bone and nacre." Nature 392(6679): 861-862.

[48] Sommerdijk, N. A., E. N. van Leeuwen, et al. (2007). "Calcium carbonate thin films as biomaterial coatings using DNA as crystallization inhibitor." CrystEngComm 9(12): 1209-1214.

[49] Platias, S., K. Vatalis, et al. (2014). "Suitability of quartz sands for different industrial applications." Procedia Economics and Finance 14: 491-498.

[50] Hajjaji, W., K. Jeridi, et al. (2009). "Composition and properties of glass obtained from Early Cretaceous Sidi Aich sands (central Tunisia)." Ceramics International 35(8): 3229-3234.

[51] Saikia, B., G. Parthasarathy, et al. (2008). "Fourier-transform infrared spectroscopic characterization of naturally occurring glassy fulgurites." Bulletin of materials science 31: 155-158.

[52] Meftah, N., A. Hani, et al. (2021). "A holistic approach towards characterizing the El-Oued siliceous sand (eastern Algeria) for potential industrial applications." Arabian Journal of Geosciences 14: 1-14.

[53] Legrand-Buscema, C., C. Malibert, et al. (2002). "Elaboration and characterization of thin films of TiO2 prepared by sol–gel process." Thin Solid Films 418(2): 79-84.

[54] Takahashi, N., M. Hoshogi, et al. (2002). "Catalyst-enhanced vapor-phase epitaxy of quartz thin films under atmospheric pressure." Journal of Materials Chemistry 12(3): 719-722.

[55] Roccaforte, F., S. Dhar, et al. (1999). "Epitaxial crystallization of amorphous SiO 2 films deposited on single-crystalline α-quartz." Applied physics letters 75(19): 2903-2905.

[56] Bertone, J. F., J. Cizeron, et al. (2003). "Hydrothermal synthesis of quartz nanocrystals." Nano Letters 3(5): 655-659.

[57] Hervey, P. and J. Foise (2001). "Synthetic quartz crystal—A review." Mining, Metallurgy & Exploration 18: 1-4.

[58] Hosaka, M. and T. Miyata (1993). "Hydrothermal growth of α-quartz using high-purity α-cristobalite as feed material." Materials research bulletin 28(11): 1201-1208.

[59] Attallah, M. and R. Bensaha (2010). "Elaboration et caractérisation des couches minces d'oxyde de silicium obtenues par voie sol gel."

[60] Hinsberg, W., C. Willson, et al. (1986). "Measurement of Thin-Film Dissolution Kinetics Using a Quartz Crystal Microbalance." Journal of The Electrochemical Society **133**(7): 1448.

[61] Johannsmann, D., K. Mathauer, et al. (1992). "Viscoelastic properties of thin films probed with a quartz-crystal resonator." Physical Review B **46**(12): 7808.

[62] Lucklum, R. and P. Hauptmann (2001). Thin film shear modulus determination with quartz crystal resonators: a review. Proceedings of the 2001 IEEE International Frequncy Control Symposium and PDA Exhibition (Cat. No. 01CH37218), IEEE.

[63] Carretero-Genevrier, A., M. Gich, et al. (2013). "Soft-chemistry–based routes to epitaxial α-quartz thin films with tunable textures." Science **340**(6134): 827-831.

# Chapter one

# Definition and Literature Review

## I.1 Introduction

Finding sources of raw materials is one of the interests of scientists or researchers, and these raw materials have different importance depending on the substance or use, such as: a meteorite, wood, the breakdown of biological materials and rocks, with the latter being one of the most significant sources of raw materials because it makes up the earth's crust and inner layers because to its abundance. What are rocks? What is the composition of rocks? What are their types?

## I.2 Definition of rock

Rock is a naturally hard substance that is derived from the Earth, as is usually known. Everyone would understand the usage of rock or as it is more often called, stone, in large slabs or pieces for ornament or construction or both, and in little bits as an aggregate for use as a material for roads or in concrete. The obvious desirable qualities—hardness, durability and in some cases a beautiful appearance can not be easily achieved in other man-made materials, the majority of which still depend heavily on natural stone. Only a few number of remote quarries would provide stone of the required quality; rock might also be found in some road cuts, along riverbanks and shorelines, as well as in hilly and mountainous terrain. Similar to how soil, clay, sand and gravel are typically regarded as different types of materials rather than rocks [1].

## I.3 Classification of rocks

The earth's crustal rocks, which are essentially a collection of different minerals, are thought to be the source of minerals. Depending on their way of origin, they can be generally divided into three groups: the rocks that are igneous, metamorphic and sedimentary [2]. Similar to igneous rocks, sedimentary rocks are composed of a fairly limited number of minerals, including quartz, carbonates, clay and feldspar. Construction, industry, agricultural technology and cosmetics are all supported by minerals [3].

### I.3.1 Metamorphic rocks

Any rock that is formed from previously existing igneous, sedimentary and metamorphic rocks through significant changes in temperature, deep under the Earth's crust, pressure, shearing stress and chemical environments are considered to be metamorphic. The process excludes weathering and diagenesis. Normally, igneous intrusions are linked to thermal metamorphism. Intense localized pressures present during dynamic metamorphism

tend to break up the rocks, frequently to a very fine-grained condition. A large area of metamorphism that involves directed pressures, shearing stress, a wide range of temperatures and confining pressures is referred to as regional metamorphism [1].
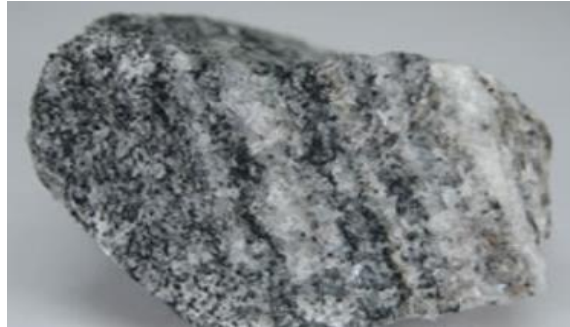


**Figure I.1:** Metamorphic rocks [4]

## I.3.2 Igneous rocks

The igneous rocks are a magmatic origin, which involves the emergence from a molten liquid and subsequent crystallization—distinguishes them. With a few glassy or amorphous exceptions, they are crystalline and primarily made of silica or silicates. They have a less variable texture than sediments, which is influenced by the content of the magma as well as the method of transit for molten or semi-molten magma, but mostly by the pace of cooling. The idea of "magmatic evolution" is the best way to describe the genetic factors that regulate igneous rocks' chemical and mineral composition, this forms the basis for their classification, as well as the innate connections that exist between them [5].



**Figure I.2:** Igneous rocks [4]

## I.3.3 Sedimentary rocks

A sedimentary rock is more difficult to define as there is a great variation in mode of origin and in the nature of the materials involved. Broadly there are two main groups, the detrital sediments and the chemical sediments; the latter include the biochemical or organic sediments. The shattered fragments (clastic texture) that come from any pre-existing rock or from the solid byproducts created during chemical weathering of such rocks and that have been physically moved to their areas of deposition make up the majority of the fragmented or detrital rocks. The majority of an organic or inorganic substance in a chemical sedimentary rock is created by direct precipitation from a solution or colloidal suspension. It usually has a non-clastic, frequently crystalline, texture. There are detrital rocks with a significant non-detrital content and vice versa. Finally sediments are subject to physical and chemical changes after they have formed, so that original minerals, textures and structures may be greatly modified after the formation of the sediment. These diagenetic changes, as they are called, take place under near-surface temperatures and pressures and result finally in lithification [1].



**Figure I.3:** Sedimentary rock [4]

The whole types of sedimentary rocks are:

**Clastic sedimentary rocks** form from the accumulation and lithification of mechanical weathering debris. Examples include: **breccias, conglomerate, sandstone, and shale.**



**Figure I.4:** Breccia



**Figure I.5:** Conglomerate



**Figure I.6:** Sandstone

**Figure I.7:** Silstone          **Figure I.8:** Shale

**Chemical sedimentary rocks** form when dissolved materials preciptate from solution. Examples include: **chert,** some **dolomites, flint, iron, ore, limestones, and rock salt.**



**Figure I.9:** Chert          **Figure I.10:** Dolomites          **Figure I.11:** Flint



**Figure I.12:** Iron ore          **Figure I.13:** Limestones          **Figure I.14:** Rock salt

**Organic sedimentary rocks** form from the accumulation of plant or animal debris. Examples include: **chalk, coal, diatomite,** some **dolomites,** and some **limestones**[4].



**Figure I.15:** Chalk          **Figure I.16:** Coal          **Figure I.17:** Diatomite

**Table I.1:** Rock classification was streamlined in 1957, following the British Code of Practice CP2001 [5]

| Group | Rock type | |
|---|---|---|
| **Sedimentary** | Sandstones (Including Conglom-erates) | Silicious |
| | | Calcarous |
| | | Ferruginous |
| | | Argiliaceous |
| | Some hard shales and tuffs | |
| | Massively Limestone Thinly bedded | bedded (Including chalk) |

Metamorphic { Some hard shales / Slates / Schists / Gneisses

Igneous { Granite / Dolcrite / Basalt
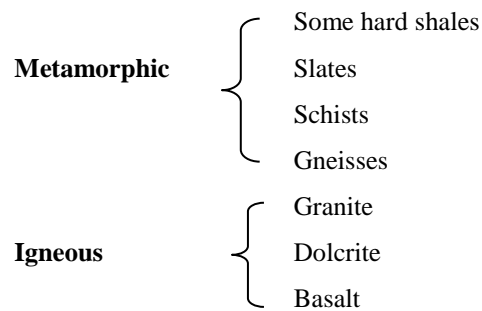
## I.4 Formation of sedimentary rocks

Feldspars, clay, carbonates and quartz make up the majority of the minerals that are present in sedimentary rocks [6].

### I.4.1 Feldspars

A category of alumino silicate minerals known as feldspars contain the elements potassium, sodium, and calcium as well as, sporadically, barium, cesium, and is amorphous forms of these elements [7]. The presence of surface charges as well as variations within the crystal lattice result from the substitution of Al-Si with varying proportions of silica tetrahedra, which are members of the mineral feldspar family [8]. Contrary to orthoclase, which normally has $K^+$ as its counterion, members of the plagioclase family typically have $Na^+$ and $Ca2^{2+}$ [9-12]. China is second in terms of feldspar production and consumption worldwide [13]. Unfortunately, the majority of Chinese feldspar resources consist primarily of quartz, mica and iron minerals with good liberation size [14, 15]. The creation of certain polymers, enamel frits, paints, glazes, welding electrodes, rubber and ceramics and glass, all need feldspar as a crucial raw material [16].

**Figure I.18:** Feldspar [17]

### I.4.2 Clay

Other silicate minerals on the surface of the earth, which themselves belong to a group of clay minerals, are commonly chemically weathered to produce phyllosilicates. Clay

19

minerals are often divided into three layer types based on the quantity and arrangement of tetrahedral and octahedral sheets in their basic structure [18]. According to the characteristics of layer type (1:1, or 2:1), the magnitude of net layer charge (x) per formula unit and the type of interlayer species, clay minerals can also be divided into seven groups: kaolin-serpentine, pyrophyllite-talc, smectite, vermiculite, mica, chlorite and interstratified clay minerals [19]. There are numerous uses for layered clay minerals because of their widespread dispersion and the vast range of reactions they undergo in nature [20, 21]. Depending on the layer structure and particular properties, such as high specific surface area, ion exchange capacity or hydration property, clay minerals were widely used in ceramics and building materials, oil drilling, pharmaceuticals, paper industries, foundry moulds and as adsorbents, catalysts or catalyst supports, ion exchangers and decolorizing agents [22-25].



**Figure I.19:** Clay [26]

## I.4.3 Calcium carbonate (calcite)

One of the most prevalent substances in the world is calcium carbonate ($CaCO_3$), which can be found in the crystal forms calcite, aragonite and vaterite [27]. 95 years after W. L. Bragg determined the orthorhombic polymorph of $CaCO_3$'s structure for the first time in 1924 [28], researchers are still interested in this form of the compound. This is brought on by aragonite's ubiquitous availability and crucial function in geochemistry, particularly during the biomineralization process [29]. The space group of calcite structure is R3c [30] and several fabrication techniques have been used to create its thin film, according to reports in [31-33]. Calcite is a mineral that can be found in hydrothermal and secondary mineralization as well as metamorphic and igneous rocks, is significant in sedimentary contexts. Due to their occurrence in many geological contexts, aragonite and calcite are of interest [34]. For the purpose of examining structural origins of optical anisotropy, these minerals that resemble calcite are widely used as model compounds [29].

**Figure I**.20: Calcite [4]

## I.4.4 Quartz

The composition of quartz within the Earth has been a subject of debate as old as geology, since silicon and oxygen are two of the most common elements in the Earth's crust make up quartz ($SiO_2$) [35]. In the earth's crust, it is the second most frequent mineral after alumino-silicates that is used to make basic rocks. Two examples of rocks with a high quartz content are sandstone and quartzite. Additionally, igneous rocks contain significant amounts of quartz. A dielectric mineral with a very high electrical resistance is quartz ($SiO_2$) [36]. There are two polymorphic phases of quartz: α-quartz and β-quartz [37]. As molten magma at 800°C and subsurface hydrothermal veins at 250 to 450°C generate quartz, which is found in rocks, soils and sands [38].

Only a small number of elements can be introduced into quartz's crystal lattice since it is chemically extremely close to being 100% $SiO_2$ [39-42]. Due to the extensive abundance of quartz in sedimentary, igneous and metamorphic rocks, numerous attempts have been made to use trace elements for genetic interpretations [43-46].

Sands and gravels made of quartz are extensively mined for use in hydraulic fracturing, glassmaking, abrasion and foundries. For a variety of high-value applications, including microelectronics and telecommunications, highly treated monocrystalline quartz plates are sought [47].



**Figure I.21: C**rystal quartz [4]

The four varieties of quartz, which are polymorphism minerals are listed in Table I.2 [35].

**Table I.2:** Quartz polymorphs at atmospheric pressure

| Stability' s temperature range | Polymorph | System of class of symmetry |
|---|---|---|
| To 573 | α-quartz | Trigonal (3 :2) |
| 573-870 | β-quartz | Hexagonal (6 :2) |
| 870-1470 | α-tridimite | Rhombic |
| 1470-1710 | α-cristobalite | Tetragonal (4 :2) |
| Above 1710 | Vein quartz | |

## I.5 Properties of rocks

One of the most prominent and accessible characteristics of rocks is their color, which is also one of the hardest characteristics to measure. Color variations should not be discounted as descriptors because they can frequently be caused by mechanically insignificant changes in rock chemistry, although having little meaning as a mechanical index. It is occasionally possible to discern marker horizons using color variations, which is helpful for stratigraphic correlation. They are also linked to significant alterations in a rock's mechanical properties.

The 'hue' (a combination of primary colors), the 'saturation' and the 'depth' are the three characteristics needed to quantify rock color. How dazzling or vivid a color is described using the terms value and chromium. The most recent source for the nomenclature of rock hues is the Geological Society of America's (1963) color chart, which was based on the Munsell Color Notation (1941). Chayes (1956) goes into considerable detail about the modal analysis of a rock. Assuming that the different mineral or pore phases can be visually identified, the modal analysis of a rock and the determination of the mineral volumetric composition are measured using metrological techniques on a microscopic image of the rock [5].

## I.6 Thin films

A thin film is a material layer that ranges in thickness from a nanometer (monolayer) to several micrometers. The carefully controlled synthesis of materials as thin films (a process known as deposition) is a vital step in many applications.

Thin film of the piezoelectric materials have a number of benefits in microelectromechanical systems (MEMS) due to the large motions that can be produced, frequently with low hysteresis, the high available energy densities, as well as the high sensitivity sensors with wide dynamic ranges and low power requirements [48].

## I.6.1 Mechanism of the production of thin films

Three fundamental phases can be distinguished in the thin films deposition process:

- The preparation of the atoms, molecules and clusters that form films.

- The particles move, from the source to the substrate.

- The adherence of particles to the surface of the substrate and ultimately, the development of thin films.

These stages can be regarded as independent or as influencing one another depending on the individual deposition procedure and/or the selection of the deposition [49] parameters. The thin film is created by the phase-changed atom-by-atom deposition of the film's constituent elements (metals, semiconductors, insulators, dielectrics, etc.) on a substrate. The two subsequent depositions of atoms and layers must be separated by an acceptable amount of time. All atoms (or molecules) in thermodynamically stable films will adopt locations and orientations that are energetically comparable to the nearby atoms of the substrate or to the earlier layers and over time, the influence of the substrate or the first layers will diminish.

## I.6.2 Process of thin film growth

A typical thin film deposition process is made up of the major steps listed below [49]:

1. Thermal accommodation;

2. Atomic/molecular adsorption (physisorption);

3. Diffusion of the surface;

4. The development of atoms- atoms and substrate- atoms bondings (chemisorption);

5. Nucleation: the gathering of individual molecules or atoms;

6. Creation of structure and microstructure (such as single crystals, polycrystalline structures, amorphous materials, roughness and defects, etc.);

7. Modification to the bulk of the film, such as grain growth or diffusion, depending on the strength of the interaction between the film's growing atoms and the atoms that are deposited in the substrate., there are three distinct mechanisms for thin film condensation in thin film production. Which are:

a) Layer-by-layer development,

b) The formation, expansion and coalescence of islands in three dimensions,

c) The absorption of a monolayer and subsequent nucleation on top of that layer most often brief.

## I.7 Piezoelectricity

The Greek words "piezein" (pressure) and "elektron" (electron) are combined to form the word "piezoelectricity." Piezoelectricity is the capacity of some materials (crystals, ceramics, polymers, or composites) to convert mechanical energy into electrical energy and vice versa. In 1817, Abbé René Just Haüy provided the first qualitative analysis of piezoelectricity.

The discovery is still attributed to Peter and James Curie, who were the first to investigate these materials in 1880. There are differences between direct and indirect piezoelectric effects. A direct effect is when electrical charges appear as a result of mechanical stress being applied to a substance. The material appears to deform mechanically when subjected to an electric field, which is an example of the indirect effect [50]. (Figure I.22, Annex ).

## I.7.1 Symmetry and piezoelectricity

Piezoelectricity reveals itself on a crystalline scale by polarizing the mesh. At the mesh level, it occurs from the separation of the centers of gravity of positive loads and negative loads as a result of deformations brought on by stresses. The existence or nonexistence of piezoelectricity depends critically on the symmetry features of crystals. Crystals without a center of symmetry can be piezoelectric, whereas any body with one is not.

Twenty-one of the 32 crystal classes lack a center of symmetry. Twenty of them are piezoelectric. According to the organization depicted, there are ten pyroelectric and polar classes, which exhibit electric polarization even when no external electric field is present. The preferred direction of polarization is along the crystal's polar axis [51]. (Figure I.23, Annex ).

## I.7.2 Piezoelectric Materials

Piezoelectric materials can be [52]:

1. Crystals with a non-centrosymmetric structure but no permanent dipolar moment in their elemental mesh, such as quartz ($SiO_2$) or langasite ($La_3Ga_5SiO_{14}$),

2. Crystals with a non-centrosymmetric structure but an elementary mesh with a persistent spontaneous dipolar moment, producing a monodomain "polar" crystal. Examples include the materials mentioned above: $ZnO$, $LiIO_3$, $Fe(IO_3)_3$,

3. Ferroelectric ceramics or crystals that have been polarized (poling), such as $BaTiO_3$ and $LiNbO_3$,

4. Ferroelectric polymers such as PVDF.

Depending on the case, these materials can exist in different forms such as monocrystalline, ceramic, thin layer and finally composite.

## I.8 Previous Studies

## I.8.1 Rocks

Many researchers studied rocks in many parts of the world including:

In (2007) F. Arikan et al., [53] made a research that determined the weathering characteristics of acidic volcanic rocks (dacite and andesite) from northwest Turkey and their effects on some engineering properties of the rocks. A series of simple and multiple regression and factor analyses suggested that porosity, indirect tensile strength, block punch strength and P wave velocity were the most suitable parameters for a quantitative estimation of weathering grades for engineering purposes. In addition, a weathering classification system based on visual descriptions and Schmidt hammer rebound values is also suggested for the rock masses studied.

In (2012) M. TAM, [54] made a research on the raw materials, clinker and cement from the Mass cement factory in Sulaimani City- Kurdistan Region NEIraq have been investigated using polarizing microscopy, X-ray diffraction (XRD), Scanning Electron Microscopy SEM and chemical analysis. This study discussed the composition and phases mineral variation from different sample type of the factory. The analyzed local limestone from Sinjar formation is almost pure, consist mainly of CaO 52. 35 % with a small amount impurities of $SiO_2$, and MgO 4.46 %, 0.06 %, respectively.

In (2017) B. L. Penuel et al., [55]  gave a study that confirms Adamawa State  (Kenya) characterised by sedimentary rock varieties which include calcareous sandstones, feldspathic sandstones, limestones and shales with sandstone intercalations as well as shelly limestones. From the research findings/analysis, there was a high qualitative presence of carbonate ions in all the rock samples. The XRD confirmed the presence of calcite, quartz, rutile, augite srebrodolskite, sanidine and plagioclase in the rock samples in most of the locations.

In (2019) A. H. Al-Ghamdi, [56] collected ten granite rock samples randomly from different locations in Haradh region, Saudi Arabia; in order to study the natural radioactivity of U-238, Th-232, and K-40. The samples were analyzed by HPGe-based gamma-ray spectrometer. The results indicated that all the concentration values of $^{226}Ra$, $^{232}Th$, and $^{40}K$ are below the world average values and are comparable to similar studies carried out

previously. , meaning that the area under study is radiologically safe for habitation and can be used as construction materials.

In (2020) M. Abdelhedi et al., [57] used an ultrasonic technique which is non-destructive to characterize mechanical strength of carbonate rock aggregates, mainly defined with Los Angeles (L.A.) and Micro-Deval (M.D.E.) measurements. Through the results obtained we can see that they indicated the ability of this technique to elaborate an accurate approach for prediction of mechanical performances determined with laborious experiments on rock aggregates.

In (2020) M.M. Sabri, [58] collected 28 samples of rocks from three different places of Kurdistan region-Iraq: Haybat Sultan (HS) region in Koya city as well as TaqTaq (TA) and Garmuk (GT) district nearby Koya city. Throughout the analysis which was done, 34 major and trace elements were detected in the rocks collected from HS region, whereas 40 major and trace elements were detected in the rocks collected from TA district and GT district. In addition, it was found that the structures of these rocks were crystalline in nature, also all rocks contain   Ca-oxide and Fe-oxide such as in HS and TA rocks, whereas they related to silica and Fe-oxide in GT rocks. In addition, alumina ($Al_2O_3$) is also a major trace in all the three rock samples of HS, TA, and GT.

In (2021) Z. Bazzine et al., [59] studied the alteration of petrophysical properties of sandstone reservoir rocks due to the adsorption of oil-based mud surfactants and wettability of drilling cutting samples from sandstone reservoirs were investigated through relative permeability, wettability index and adsorption measurements at standard conditions in a micromodel device. The drilling cutting samples from sandstone reservoir formation have characterized by the predominance of quartz 71.9% with clay mineral, dolomite and calcite content.

## I.8.2 Review of prior CaCO$_3$/SiO$_2$ research

Many researchers have examined numerous deposition strategies to create $CaCO_3$/$SiO_2$ and their thin films, and different environmental conditions with various characterization approaches were also accomplished.

## I.8.2.1 Calcite

In (1980) D. Wolfgang, [60] presented a study theoretically treating the processes involved in the deposition of $CaCO_3$ from thin films of supersaturated calcareous solutions include: (a) diffusion of carbon dioxide from the solution where the gradual chemical reaction

$H_2CO_3= CO_2 + H_2O$ occurs; (b) surface-controlled $CaCO_3$ deposition; (c) $Ca^{2+}$ ions diffuse to the calcite surface; and (d) production of $CO_2$ at the calcite surface via deposition of $CaCO_3$. Rate-determining turns out to be the final procedure. Calculations are done to demonstrate how the deposition rate depends on the temperature, water film thickness, and calcareous solution content.

Using the accurate information for these parameters, this theory is applied to the formation of stalagmites and wall sinters in caves. For the first time, there is a great deal of agreement between the computed values and the observed data. They were able to quantitatively forecast speleothem growth rates using this theory for the first time in concordance with the collected data. They had theoretically proven that $CaCO_3$ had been deposited on stalagmites.

According to their theory, precipitation rates as a function of film thickness depend on the conditions of the impinging solution and time, and can be used as a starting point for additional computations. They have begun these calculations in an effort to simulate stalagmite formation on computers under various settings. The initial positive outcomes have been obtained and will be published later.

In (1998) G. Xu et al., [61] were created macroscopic-scale continuous calcium carbonate thin films with a thickness ranging from 0.4 to 0.6 ím by combining a semirigid template with a soluble inhibitor, two of the critical controls used in the mineralization of organisms. Under mild conditions, the applied strategy offers a new perspective for thin film synthesis and biomimetic processing. By witnessing the transition from the precursor phase of amorphous calcium carbonate to the crystalline phase, it was shown that the multistage crystallization process is feasible in a biomimetic environment.

Also during the phase transformation, by structurally correlating the orientated crystal plane with the porphyrin template, the organic matrix can control crystallization.

In (2000) T. Kato, [62] provided a study on how to build multilayer polymer/calcium carbonate composites by simulating the production of nacre in a shell. To cause thin-film crystallization of $CaCO_3$ on the solid matrices, they mixed insoluble chitin or chitosan solid matrices with soluble acidic macromolecules, such as poly (acrylic acid). The polymorph that is created using this way can also be managed.

Organic/inorganic composite materials with organized and/or hierarchical structures can lead to materials with unique functions and significantly improved mechanical properties on the nanometer or micrometer scale. Calcium carbonate and organic polymers derived from biomolecules are an example of inorganic substances whose constituents impart environmental friendliness to the resulting materials. The results reported offer approaches to a new type of hybrid material.

In (2001) N. Hosoda and T. Kato, [63] were utilized cellulose, chitosan, and chitin as solid matrixes to create thin films of calcium carbonate ($CaCO_3$) crystals in the presence of an acidic macromolecule. On these solid matrixes, thin film $CaCO_3$ crystals with a thickness of about 0.8 m grew as a result of crystal formation from a $CaCO_3$ solution that contained poly (acrylic acid) as a soluble acidic polymer. According to X-ray measurements and SEM observations, the crystallite size is around 30 nm. Using hydrogen bonds between the OH or NH groups of the polymer matrix and the COO-units of the soluble ingredient. Poly-(acrylic acid), a soluble additive, is adsorbed on the polymer matrix's surface. The acidic polymer that has been adsorbed on the solid matrix and the acidic polymer that is still in solution are both necessary for the creation of the $CaCO_3$ thin film crystals. The acidic polymer's nucleation and inhibitory effects must be balanced for crystallization to occur. The findings of this study present opportunities for the creation of novel organic/inorganic composite materials that are both highly functional and environmentally friendly.

In (2003) P. K. Ajikumar et al., [64] created thin films of calcium carbonate polymorphs using a demineralized eggshell membrane and Nylon 66 fiber weave, while vaterite or aragonite mineral phases were deposited on the surface of PAsp- and PGlu-adsorbed eggshell membranes, respectively. On Nylon 66 fiber knit surfaces with PAsp spreadsorbed, calcite thin layers favored development. Nylon 66 knits and eggshell membranes were allegedly used as templates for the creation of biocompatible calcium carbonate thin films for the first time in this study's biomimetic method.

This strategy has implications for comprehending the complementary function of acidic polymers and template molecules in the biomineralization process. Utilizing scanning electron microscopy, X-ray diffraction, and energy-dispersive X-ray scattering studies, the mineral films were characterized.

In (2004) X. Xu et al., [65] used the development of large-area and continuous calcium carbonate films under benign conditions was achieved by stopping the crystallization process where ACC generation occurs and ACC transformation is halted. Films of amorphous calcium carbonate (ACC) have developed both with and without a poly (acrylic acid) inhibitor. Using optical microscopy, it has been discovered that ACC transforms into crystalline vaterite or calcite. External reflection infrared spectroscopy has confirmed this discovery. The transition of ACC is inhibited by substrates and inhibitors, which leads to the creation of high-quality $CaCO_3$ films. According to their findings, ACC precipitates are first created from extremely supersaturated solutions, which then deposit as films thanks to the collaboration between an insoluble matrix and a soluble inhibitor. It was discovered that the matrix and inhibitor also affected the growth, shape, and structure of the $CaCO_3$ crystal by altering the phase change of ACC into crystalline forms. The biomineralization and crystallization of calcium carbonate have both been found to be significantly influenced by ACC.

In (2007) S. K. Medeiros et al., [66] presented a study on the $CaCO_3$ calcite polymorph that was carried out utilizing calculations of the electrical and optical properties based on density functional theory within the local density (LDA) and generalized gradient (GGA) approximations, respectively. The dielectric function does not significantly change with light polarization, the effective masses of the carriers are estimated, and the indirect nature of the energy gap is demonstrated, with EG (D LDAZ) = 4.95 eV and EG (D GGAZ) = 5.07 eV (for comparison, the experimental value is 6.0 0.35 eV).

In (2008) Y. Oaki et al., [67] successfully used $CaCO_3$ and an organic polymer to created nanosegregated amorphous composites. The nanocomposite materials were produced naturally by a simple process in a welcoming environment. These amorphous composites stand out for both their bulk and thin film transparency and stability. By incorporating dye molecules or noble metal nanoparticles into a dispersion at the molecular level, they also demonstrated the functionalization of the amorphous nanocomposites.

In (2009) F. M. Hossain et al., [68] investigated the electrical, optical, and bonding characteristics of $CaCO_3$ (calcite) using first-principles calculations inside density-functional theory. The optical band gap of the Brillouin zone is calculated to be 6.0 eV, which is in agreement with the experiment and shows that the optical band gap is greater than the indirect band gap (M). The estimated indirect energy gap is 5.07 eV. Through the fundamental

absorption edge (optical band gap) of 6.0 Ev, which provides the direct permitted optical transitions along high symmetry directions in the Brillouin zone, the optical band gap is greater than the indirect band gap ( M) and exhibits conformity with the experiment.

The optical anisotropy of the calcite structure shown by the findings is likewise substantial. Mulliken population investigations, which in turn revealed the bonding properties, revealed the existence of concurrent ionic and covalent bonding in calcite.

In (2010) L. Cheng et al., [69] developed a method by solution surface colloidal lithography at the solution surface was employed by to make it simple to fabricate thin films of amorphous calcium carbonate (ACC) and mosaic calcite with honeycomb patterns.
First, thin films with a honeycomb pattern were created employing a polymer-induced ACC coating of the monolayer colloidal crystal (MCC) template at the air/water interface. Due to controlled crystallization of the prepared HP-ACC thin films under certain circumstances, honeycomb-patterned crystalline films with various microstructures have grown. Particularly, the amorphous films were subjected to a thermal treatment at 400 °C, which caused the creation of mosaic calcite thin films with a honeycomb pattern that could develop from single-crystalline calcite plates.

Additionally, the dye molecules were incorporated into the HP-ACC thin film during its production, providing the patterned thin film with additional fluorescence capabilities. The highly ordered HP-ACC thin films also exhibited typical photonic characteristics and had spectacular structural colors.

In (2010) I. Sethmann et al., [70] examined how the degree of lattice mismatch at their interface impacts the growth pattern of the precipitating mineral phase. At $Mg_2/Ca_2$ ratios of 2–7, fast layer-by-layer formation of magnesian calcite was seen utilizing in situ atomic force microscopy on pure calcite (1014) substrates.

The bulging in the epitaxial magnesian calcite thin film under solution conditions of calcite saturation states starting from 33, depending on $Mg_2$: $Ca_2$ ratios and carbonate content, has generated the networks of ridge along the [441], [481], and [421] directions. Eventually, distinct and independently developing crystal segments emerged as a result of stagnant multilayer steps produced at the ridges where monolayer spreading had ceased. Through the use of computational molecular dynamics modeling, it was discovered that the interfacial lattice mismatch between pure alcite and the isostructural magnesium containing phase, which

has smaller lattice constants, is what causes the semicoherent interface and disordered linear zones cutting through the thin film. As a result, the surface swells up in a manner that is consistent with our laboratory data. The behavior of stressed thin films is better understood because strain-induced cleavage frequently produces aggregates of suitable microcrystals.

In (2010) A. Ayoub et al., [71] employed the most recent first principles theory to analyze the structural and mechanical characteristics of calcium carbonates ($CaCO_3$). Through structural relaxation resulting from their calculations, an accurate assessment of material properties at ambient circumstances as well as under hydrostatic pressure was made. The estimated ground state parameters accord reasonably well with experimental data. By completing a structural phase stability study, they were able to anticipate the first and second order phase transitions that calcium carbonate crystals go through under hydrostatic pressure. The first occurs between the calcite and aragonite phases at 3.3 GPa, whereas the second occurs between the aragonite and post-aragonite phases at 40 GPa. The experimental estimate (40 GPa), which was published by Ono et al., and the earlier estimate are in excellent agreement. To confirm the validity of such phase transitions, they investigated the mineral high pressure stability using mechanical property behavior. Both transversal wave velocity and elastic module exhibit an unexpected reduction at phase transition pressure range.

In (2011) M. G. Brik, [72] published in the current study thorough ab computations of the structural, electrical, optical, and elastic properties of two crystals, magnetite ($MgCO_3$) and calcite ($CaCO_3$). Both substances are significant natural minerals that are crucial to the cycling of carbon dioxide. When data from the literature were available, the optimum spectra and refractive index dependence on wavelength were calculated and compared. $MgCO_3$ and $CaCO_3$ both have computed band ga1ps of 5.08 eV and 5.023V, respectively, making them indirect band compounds. Compared to the experimental data, both values are about 1.0 e underestimated. Despite the fact that both crystals have the identical structure, the substitution of Mg and Ca ions causes several variations that are visible in the widths and profiles of the electronic bands, the structure of the estimated absorption spectra, and the values of the elastic constants. Within the pressure range of phase stability, the response of the two crystals to the applied hydrostatic pressure was examined. Variations in the lattice characteristics and typical interionic distances were taken into account. The properties of these two hosts at the high pressures seen in the Earth's mantle can be predicted using the obtained dependence of lattice constants and computed band gap on pressure.

In (2019) G. Chahi et al., [73] were examined the structural and elastic characteristics of the two known hydrated phases of calcium carbonate (i.e., ikaite and monohydrocalcite). Additionally, a comparison study using dispersion-corrected density functional theory (DFTD2) and standard density functional theory (DFT-PBE) based computer simulations of atoms was carried out. Properties like elastic constants, bulk modulus, Young's modulus, shear modulus, Poisson's ratio, acoustic wave velocities, and Debye temperature were analyzed for the first time at the DFT level theoretically. Because the examined properties have not yet been evaluated experimentally, the DFT-PBE and DFT-D2 values offer limitations that permit bracketing of the unknown experimental values. The evolution of the structural and elastic characteristics of ikaite and monohydrocalcite under pressure in the range of 0 to 5 GPa was investigated. Monohydrocalcite is expected to undergo a brittle-ductile transition between 1.3 and 2.2 GPa.

In (2022) S. Zhang et al., [74] was investigated the solid-state transition of ACC thin films using the ammonia diffusion technique (ADM) in the presence of $Mg^{2+}$ ions and poly (acrylic acid) (PAA). According to their findings, the chemical makeup of the ACC precursor and the heating regime used can regulate the structure, composition, and polymorph of the final crystalline films. While films made at ambient temperature feature spherulitic structures, mild-isothermal heating created a mosaic of tabular single crystals that ranged in size from a few hundred micrometers to several hundreds. It's significant that single crystal domain-containing pure aragonite films can be produced at extremely low magnesium concentrations, and that the crystal structure of the annealed films can be regulated in accordance with the magnesium level of the ACC precursor. These tests provide the capacity to describe the thin films using transmission electron microscopy (TEM), which is a useful tool for research of magnesium ACC employing thermal analysis methods like thermogravimetric analysis (TGA).

In (2022) J. H. Mokkath, [75] used simplified TD-DFT with the Tamm-Dancoff approximation and density functional theory with semi empirical dispersion corrections to examine the effects of the adsorption of straight chain alcohol (ethanol and pentanol) molecules on the optical characteristics of a calcite (10.4) surface. Ethanol and pentanol molecules form a well-ordered monolayer on top of the calcite (10.4) surface by chemically attaching to it via their OH functional groups. Intriguing modulations were also discovered in the circular dichroism and photo absorption spectra. The latter was a special optical

fingerprint for a calcite (10.4) surface that had molecules adsorb to it. Their atomic-level discoveries shed light on the structural and optical characteristics of calcite-based systems.

## I.8.2.2 Quartz

In (1989) C. K. Hruska and R. Brendel, [76] employed the thickness modes of plates to calculate the electrostriction of alpha quartz and the third-order piezoelectric constants. By fitting a least-squares model to more than one hundred observations of the change in the resonance frequency of the thickness modes of quartz plates caused by a dc field (the resonator method), it was possible to determine ten linear combinations of the fundamental material constants of third-order piezoelectricity and electrostriction of quartz. The differences between comparable constants are no longer out of proportion with their standard deviation, and there is a very high agreement between our results and their counterparts obtained separately via the transit-time approach (pulse propagation in bulk quartz) with one exception.

In (2001) T. Zeng et al., [77] demonstrated that the development of thin silicon oxide is the foundation for modem IC technologies. The formation of oxide for thick films is effectively explained and predicted by the Deal-Grove model. But thin films are an exception. There are more models based on the Deal-Grove mechanisms that have fitting ranges to thinner films that are similarly non-stretchable. Recent examples of cutting-edge experiments include ion scattering spectroscopy and isotopic labeling, which have discovered a hybrid or transition layer between pure silicon dioxide and pure silicon during silicon oxidation. Their paper had created a physically sound model for the formation of oxide through the volumetric reaction in the transitional layer as well as the reaction at the $SiO_2$/Si contact. For thick films, the Deal-Grove model approaches limitations, whereas for thin films, the volumetric reaction is more significant.

The paper also studied the hybrid layer or transitional layer for the oxide generated in Axcelis' hot-wall based rapid thermal furnace using an enhanced SlMS (secondary ion mass spectrometry). The thickness of the transitional layer varies depending on the growth temperature and ranges from 20 to 40 angstroms. The model used in the study accurately predicts the oxide development rate for both thin and thick films, as well as the thickness of the transition layer.

In (2003) A. G. Revesz and H. L. Hughes, [78] presented a study showing that the growth of vitreous (v) $SiO_2$ films resulting from the thermal oxidation of silicon are non-crystalline (nc), but they have a high degree of short-range-order and bond ordering, which is typically not the case with amorphous solids.

A slight change in the Si-O bond energy results in this combination as the Si-O-Si bond angles (/) range from less than 120 to 180. The flexibility of the nc structure is what causes the very low density of interface states induced by the quasi-epitaxial accommodation of the growing oxide to the Si substrate. The grown oxide is non-elastically compressed, or "densified," which greatly affects a variety of properties. The bond energy increases significantly when / gets closer to _120_. One electrical consequence of these "strained" connections, for instance, is entire trapping. Non-crystalline $SiO_2$ films generated by deposition or O-implantation techniques have certain qualities in common with thermally created oxides, but they also have some highly distinct characteristics.

In (2003) H. Okudera and A. Hozumi, [79] used the Sẗober method to synthesize silica nanoparticles and thin films simultaneously on a flat substrate. They also used atomic force microscopy (AFM) to study the growth kinetics of these precipitates and the fine structure of the film surface. The thin film that was produced on a hydrophilic substrate was flat, homogenous, and had an RMS roughness of less than ≈1 nm.

Because the expansion of the film was slower than that of the particles, the growth of these silica precipitates was constrained by the diffusion of reactive silica species. On the other hand, the thin film that was created on a hydrophobic substrate was not flat, had an RMS roughness of ≈10 nm, and had convex microstructures of two different sizes on its surface. These microstructures and the observed delay in film formation on the hydrophobic surface caused these precipitates, which included spherical Stober colloids, to first form as aggregates of primary particles appearing in the precursor solution, and then to grow as a result of the adhesion of primary particles continuously emerging in the solution.

In (2008) S. M. Antao et al., [80] studied the crystal structures of quartz, sodalite, tremolite, and meionite Me79.6 and compared them with those obtained by single-crystal diffraction (SXTL). From Rietveld refinements using HRPXRD data, the cell parameters obtained appear to be superior to those obtained by SXTL. The structural parameters obtained by HRPXRD are similar if not more accurate than those obtained by the SXTL method.

In (2009) A. L. Pierce et al., [81] demonstrated how to coat silicon-based microelectrodes with a thin film of silica sol-gel and detailed how this alters the properties of the electrodes. To confirm coating adherence to the electrode and for evaluate electrical property changes, they were used fluorescently labeled coatings and cyclic voltammetry and impedance spectroscopy, respectively. The silica sol-gel successfully adhered to the electrodes as a thin coating. Voltammograms after coating revealed a small improvement in the electrodes' ability to transport a charge. The findings of this study demonstrated the viability of putting silica sol-gel coatings to silicon-based microelectrodes and prompted further research into their use to reduce reactive tissue response.

In (2010) K. P. Driver et al., [82] studied silica with quantum Monte Carlo (QMC), the inadequacies of DFT are solved by QMC, which was previously computationally impracticable for such complicated materials. Their findings offer the most accurate equations of state and phase boundaries for silica. The lack of a seismic signal implies that the transition has little to do with the lower mantle's global seismic discontinuities, and QMC shows that it occurs above the D" layer, which insulates the core. However, seismic signals may continue to be produced during the transition by deeply subducted oceanic crust. Additionally, they discovered a precise shear elastic constant for stishovite and its crucial softening under pressure in geophysics.

In (2012) F. Wang et al., [83] used a sintered-diamond multianvil apparatus and synchrotron radiations. Stishovite in situ P-V-T measurements have been made in the stability range of 17 to 54 GPa and 300 to 1700 K. Through the use of the new stishovit equation of state, they demonstrated that the thermo-elastic properties of density, adiabatic mass modulus, thermal expansion, and isobaric heat capacity are consistent with those of the earlier measurements at zero pressure. The equation of state in this work yields a lower density and a higher adiabatic modulus at lower mantle circumstances as compared to that obtained by extrapolating using a previous equation of state derived at upper mantle conditions.
For interpreting seismological evidence and statistically simulating the destiny of subducted silica-rich rocks like MORB and pelagic sediments, they have developed a new equation of state and thermo-elastic characteristics for stishovite at lower mantle conditions.

In (2013) A. C. Genevrier et al., [84] used sol-gel chemistry, heat treatment, and silicon [Si(100)] substrates to create textured low α-quartz piezoelectric thin films. The crystallographic orientation, epitaxial relationship, and microstructure of α-quartz thin films

have been investigated using (XRD) scans and TEM cross-section analysis. They only discovered representative (100) and (200) reflections from α-quartz after scanning the film with an XRD Q-2Q scanner. However, there are no peaks that match to alternative quartz orientations or silica polymorphs. Additionally, they employed a scan, which revealed a rocking curve with a full width at half maximum (FWHM) of 3, which suggested a slight out-of-plane misorientation of the nanostructured α-quartz films. The [100] Q direction, which is at 30° normal to the substrate in their films, has the highest piezoelectric response in α-quartz. By applying either a mechanical deformation (direct effect) or an electric field (converse effect) perpendicular to the film, the piezoelectric effect was measured.

In (2013) W. Pabst and E. Gregorovà, [85] reviewed a study of the silica phases elastic characteristics. The effective elastic constants (Young's module, shear module, bulk module, and Poisson ratios) are computed using the Voigt-Reuss-Hill averaging method. The literature is used to compile monocrystal data for the crystalline $SiO_2$ polymorphs low-quartz, high-quartz, low-cristobalite, high-cristobalite and stishovite.

Both experimental data and simulation results are taken into account. A table of room temperature elastic constants contains the accepted "state-of-the-art" values for crystalline silica polymorphs and silica glass. The cristobalite high-temperature simulation data show auxetic behavior for all temperatures from ambient temperature to more than 1500°C. All information is in line with the cristobalite's well-known auxetic activity at room temperature.

According to the calculations reported in this paper, quartz is also capable of auxetic behavior, but only within a very narrow temperature range at the low-to-high quartz transition temperature (420-577°C). Future research should concentrate on high-temperature measurements of experimental studies of the elastic properties of tridymite and cristobalite.

In (2014) R. Yang and W. Zhongqing, [86] were determined the elastic constant tensors of stishovite and $CaCl_2$-type silica by using first-principles calculations with a local density approximation at Earth's mantle temperature and pressure. They showed that the elastic properties of stishovit appear to be strongly pressure- and temperature-dependent. By raising temperature, stishovite's shear instability shifts to a higher pressure with a slope of 5.41.4 MPa/K. The softening of the shear modulus and the positive Clapeyron slope, which results in the unusually positive temperature dependence of the sound velocities around the phase boundary, cause sound velocities to occur at various temperatures. The change from stishovite to the $CaCl_2$-type silica takes place at a lower mantle temperature and at a depth well beyond

1200 km. This transition is followed by a velocity leap of 0.98–0.8 km/s in the S wave velocity (Vs) and 0.45–0.15 km/s in the P wave velocity (Vp).

In (2017) H. Aramberri et al., [87] gave a study showing the investigation of the thermal properties of silica as it evolves from a stishovite phase into a $CaCl_2$-type structure under hydrostatic compression using first-principles calculations. By iteratively solving the linearized Boltzmann transport equation across a wide temperature range, they calculated the thermal conductivity tensor using pressure-dependent harmonic and an harmonic interatomic couplings derived from fundamental principles. Most remarkably, they find that, $SiO_2$ displays a large peak in the in-plane thermal conductivity at low temperatures, additionally to a highly anisotropic behavior at the structural change. To determine the origin of these characteristics, they examined the phonon contributions to conductivity. They then highlighted the ramifications of their findings in the context of continuous structural alterations in general as well as the potential geological significance of their findings for silica.

In (2017) K. Uchino, [88] studied the quartz crystal's piezoelectric properties and typical uses. The discovery of quartz crystal piezoelectricity, including its structure and distinctions from other piezoelectric materials, is covered in section 5.1. Natural and artificial quartz crystal are contrasted in section 5.2, along with the procedures and requirements for growing artificial quartz crystal. Typical quartz crystal plates for vibrators are introduced in section 5.3, along with actual cutting angles. The frequency and temperature properties of these vibrators, which include the most common AT-cut thickness shear mode and the tuning fork bending mode, are detailed in depth. Additionally, samples of quartz crystal downsizing using a different cutting technique created by River Eletec Corporation are shown in this section. Applications and specifications for the quartz crystal vibrators and oscillators discussed throughout the chapter are shown in section 5.4.

In (2018) R. A. Fische et al., [89] employed synchrotron X-ray diffraction in a diamond-anvil cell that was heated by laser to examine the phase diagram and equations of state of silica at 21-89 GPa and up to approximately 3300 K. The approximate equation for the phase transition between stishovite and $CaCl_2$-type $SiO_2$ is T = 64.6(49)•P - 2830(350), where T is the temperature in Kelvin and P is the pressure in GPa. The stishovite data suggest K0 = 5.24(9) and a quasi-anharmonic T 2 dependence of -6.0(4) 10-6 GPa/mol/K2 for a fixed

q = 1 and K0 = 302 GPa, but for the $CaCl_2$-type phase $K_0$ = 341(4) GPa, $K_0$ = 3.20(16), and g0 = 2.14(4) with other parameters identical to their values for stishovite.

In (2019) J. T. Fonné et al., [90] used SIMS analysis to study the interdiffusion processes between aluminum enriched PVD-sputtered silica thin films and industrial oat sodalime silicate glass substrates are quantitatively. Heat treatments have been carried out at temperatures around or over the oat glass's glass transition temperature. Alkali's migration from the glass substrate to the silica thin film is significantly accelerated by the film's aluminum doping. There was indications of an interdiffusion process between bulk alkali ions and protons coming from a high water content in the as-deposited silica film. They verified that a straightforward thermodynamic model based on the equilibration of sodium activity between the film and the glass substrate agrees with the experimental measurements of the sodium concentration.

In (2019) Q. Zhang et al., [91] presented a study indicated that epitaxial films of piezoelectric α-quartz could enable the fabrication of sensors with unprecedented sensitivity for prospective applications in electronics, biology and medicine. However, the prerequisites for this are the use of the crystallization of epitaxial α-quartz and the tailoring of suitable film microstructures for nanostructuration.

They contributed new knowledge to the crystallization of epitaxial quartz films on silicon (100) by controlling the microstructures of the films and devitrifying porous silica. They demonstrated that by increasing the amount of devitrifying agent (Sr), it was possible to go from an α-quartz microstructure dominated by small, porous crystals to one dominated by larger, fully dense crystals. In addition, they discovered that the microstructure and homogeneity of the films are significantly influenced by the film thickness, relative humidity, and the type of surfactant.

In (2019) Q. Zhang et al., [92] studied the micro/nanostructure engineering of epitaxial piezoelectric α-quartz thin films on silicon. They also described a previously unheard-of large-scale fabrication of ordered arrays of piezoelectric epitaxial quartz nanostructures on silicon substrates using the combination of soft-chemistry and three lithographic techniques: (i) laser interference lithography; (ii) soft nanoimprint lithography on Sr-doped $SiO_2$ sol-gel thin films; and (iii) self-assembled $SrCO_3$ nanoparticle reactive nanomasks. The epitaxial quartz nanopillars were produced in a various of diameters (from 1 m to 50 nm) and heights

(up to 2 m).Their work reported the producing of epitaxial quartz thin films on silicon  has been investigated while preserving its epitaxial crystallinity and piezoelectric properties, through the complementarity of soft-chemistry and top-down lithographic techniques.

In (2020) F. Molaei and S. Hossein, [93] used the non-equilibrium molecular the non-equilibrium molecular dynamics (NEMD) simulation method to investigat the mechanical characteristics and thermal conductivity of α-quartz under uniaxial tensile loading at various temperatures, sizes, and strain rates. They made it possible to estimate mechanical and thermal parameters including tensile strength and thermal conductivity thanks to the MD simulation. While choosing a precise interatomic potential or force field, experiments can nevertheless successfully predict mechanical and thermal properties. Through simulations at various temperatures, we can see that the tension and strain at break decrease as the temperature rises. The Youngs module, however, exhibits a different behavior. The Young's modulus changes with temperature, initially falling and then rising. According to the findings, thermal conductivity is temperature-dependent, with a clear dependence at low temperatures and a minimal dependence at high temperatures.

In (2021) S. B. Khemis et al., [94] used Raman spectroscopy for a structural characterization of sputtered silica films. The Raman signature is difficult to extract due to its dwarfed compared to a glass substrate due to its low cross-section and the thinness of its silicon dioxide layer.

Being able to overcome these restrictions is experimentally difficult and necessitates the development of specific analysis strategies, based on three different methods. As a result, an integrated approach to extracting and interpreting the Raman signature of amorphous silica films deposited on a soda-lime glass substrate was developed. The dependability of each suggested method is shown to be applicable to the extraction of the silica thin film Raman spectra. These different approaches are easily adaptable to other materials, crystalline or amorphous. By using this technology, it has become clearer how sputtered silica thin film and bulk vitreous silica glass (v-SiO$_2$) differ structurally. Additionally, they talk about the benefits and drawbacks of each strategy. The densification ratio ratio of the 7% silica layers from the magnetron sputter film deposit was determined using X-ray reflection.

The network connectivity shift in v-SiO$_2$ is manifested at the medium distance range by an extremely high population of three-membered rings, leading to a more compact structure. The intertetrahedral angle reduction was used to get the short-range transformation, which was

then investigated. These findings might pave the way for more in-depth research to understand the atomic structure of films.

In (2021) T. Saksala, [95] presented a numerical research on the cracking of granitic rock by high frequency-high voltage-alternating current (HF-HV-AC) of quartz mineral's piezoelectric characteristics. In order to do this, a numerical approach based on coupled piezoelectromechanical and 3D embedded discontinuity finite elements for rock fracture is devised. The mineral mesostructure level accounts for the heterogeneity and anisotropy of rocks. With a tensile strength of about 8 MPa, new numerical simulations show that disc-shaped and cylindrical granitic rock specimens can be cracked by a sinusoidal excitation with an amplitude of about 10 kV at a frequency matching one of the specimen's resonance frequencies (for example, 125 kHz in the present case of 30 mm radius and 10 mm height).

The effects of specimen form and electrode placement are tested. When different quartz grain alignment methods are evaluated, even the worst scenario, which consists of a 50/50 mix of right- and left-handed quartz crystals without any preferred orientation, exhibits resonant frequency stresses of roughly 1 MPa. HF-HV-AC piezoelectric excitation of quartz-bearing rocks may be a possible pre-treatment method in comminution, according to the simulation results.

In (2023) Z. Radi et al., [96] were used density functional theory in 0-80 GPa high pressure domain at zero temperature, which is based on reducing an interacting many-electron problem to a single-electron problem to study the elastic properties of two high-pressure polymorphs of $SiO_2$ nanostructure, stishovite and $CaCl_2$-type. The $CaCl_2$-type phase becomes more stable at 40 GPa, however the stishovite phase is more stable using the Gibbs free energy technique. The pressure dependency of density, volume, bulk, and shear modulus was also established for the selected pressure domain.

They were able to analyze distinct $SiO_2$ phases using the density functional theory method, and they will be able to study other oxides by figuring out their elastic properties.

Calcite is not actually piezoelectric material, as we have found in earlier studies. This last characteristic of quartz has already described. According to our knowledge and the literature research that we provided, various techniques are used to study the piezoelectric effect for quartz thin films.

In this thesis, we will look at the quantitative and quantitative composition of the sandstones of this region for the first time at Ouargla University and after that we will create thin films by utilizing natural roots.

Through the extraction of both calcium ($Ca^{2+}$) and silicium (Si), which develops them as precursors for the hydrothermal synthesis to produce calcite and quartz thin films, We suspect that our quartz thin films has the piezoelectric properties.

## I.9 Conclusion

We gave an overview of rocks and their types in this first chapter. The various sandstone formations have been described. After that, certain rock characteristics have been reported. Then the mechanism of the production of thin films are given at the end of this chapter. In the next chapter, we will discuss the different materials and methods. Finally a previous study about calcite-quartz and their physical piezoelectric properties in the literature have been discussion.

# Reference
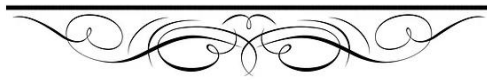
[1] Dearman, W. (1974). "The characterization of rock for civil engineering practice in Britain." Annales de la Société géologique de Belgique.

[2] Aidekoya, J. A. (1995).Negative environmental impact of mineral exploitation in Nigeria. International Journal of the Physical Sciences, 613.

[3] King, H. "Mineral and chemical composition of pure limestone-Missouri Department of Natural Resources., 2005-2015." Geology. com.

[4] King, H. M. (1997). "Interpretation and closure in the historical geology laboratory." Journal of College Science Teaching**26**(5): 329.

[5] Franklin, J. A. (1970). "Classification of rock according to its mechanical properties."

[6] Penuel, B., O. Maitera, et al. (2017). "X-Ray Diffraction Characterization of Sedimentary Rocks in Demsa Local Government Area of Adamawa State, Nigeria." Current Journal of Applied Science and Technology**24**(2): 1-9.

[7] Heyes, G., G. Allan, et al. (2012). "Review of flotation of feldspar." Mineral Processing and Extractive Metallurgy**121**(2): 72-78.

[8] Papike, J. J. and M. Cameron (1976). "Crystal chemistry of silicate minerals of geophysical interest." Reviews of Geophysics**14**(1): 37-80.

[9] Colville, A. A. and P. H. Ribbe (1968). "The crystal structure of an adularia and a refinement of the structure of orthoclase." American Mineralogist: Journal of Earth and Planetary Materials**53**(1-2): 25-37.

[10] Fitz Gerald, J. D., J. B. Parise, et al. (1986). "Average structure of an An48 plagioclase from the Hogarth Ranges." American Mineralogist**71**(11-12): 1399-1408.

[11] Phillipsi, M., A. Colville, et al. (1971). "The crystal structures of two oligoclases: A comparison with low and high albite." Zeitschrift für Kristallographie-Crystalline Materials**133**(1-6): 43-65.

[12] Wenk, H., W. Joswig, et al. (1980). "The average structure of An 62–66 labradorite." American Mineralogist**65**(1-2): 81-95.

[13] Tanner, A.O., (2012). Feldspar and nepheline syenite, U.S. GEOLOGICAL SURVEY MINERALS YEARBOOK—2010: pp. 1–8.

[14] Hu, B., X. Han, et al. (2005). "Distribution of potash feldspar resources in China and its exploitation." Geology of Chemical Minerals**27**(1): 25-32.

[15] Qifeng, Z., Q. Kezhang, et al. (2013). "Mineralogy and significance of micas and feldspars from the Koktokay No. 3 pegmatitic rare-element deposit, Altai." Acta Petrologica Sinica**29**(9): 3004-3022.

[16] Akkal, R. and M. Ouldhamou (2015). Comparative study of mineral processing applied to the local feldspar's assessment. International Mining in Proc. 24th Congress and Exhibition of Turkey-IMCET.

[17]https://www.istockphoto.com/photo/collection-of-minerals-isolated-on-white-gm502424078-81904783.

[18] Barton, C. and A. Karathanasis (2002). Clay Minerals: Encyclopedia of Soil Science, Marcel Dekker, Inc. AH rights reserved.

[19] Martin, R.T., and Baily, S.W., et al. (1991). Report of the clay minerals society nomenclature committee: revised classification of clay materials. Clays Clay Miner. 39 (3) 333-335.

[20] Vaccari, A. (1998). "Preparation and catalytic properties of cationic and anionic clays." Catalysis today**41**(1-3): 53-71.

[21] Carretero, M.I., and Lagaly, G., (2007). Clays and health : an introduction. Applied Clay Science. 36 (1-3), 1-3.

[22] Ding, Z., J. Kloprogge, et al. (2001). "Porous clays and pillared clays-based catalysts. Part 2: a review of the catalytic and molecular sieve applications." Journal of Porous Materials**8**: 273-293.

[23] Carretero, M. I. (2002). "Clay minerals and their beneficial effects upon human health. A review." Applied Clay Science**21**(3-4): 155-163.

[24] Brigatti, M. F., E. Galan, et al. (2006). "Structures and mineralogy of clay minerals." Developments in clay science**1**: 19-86.

[25] Choy, J.-H., S.-J. Choi, et al. (2007). "Clay minerals and layered double hydroxides for novel biological applications." Applied Clay Science**36**(1-3): 122-132.

[26] https://www.shutterstock.com/fr/image-photo/limestone-background-688261813.

[27] Bang, J.-H., Y. N. Jang, et al. (2011). "Effects of sodium laurylsulfate on crystal structure of calcite formed from mixed solutions." Journal of colloid and interface science**356**(1): 311-315.

[28] Bragg, W. L. (1924). "The structure of aragonite." Proceedings of the Royal Society of London. Series A, Containing Papers of a Mathematical and Physical Character**105**(729): 16-39.

[29] Caspi, E. a. N., B. Pokroy, et al. (2005). "On the structure of aragonite." Acta Crystallographica Section B: Structural Science**61**(2): 129-132.

[30] Maslen, E., V. Streltsov, et al. (1993). "X-ray study of the electron density in calcite, CaCO3." Acta Crystallographica Section B: Structural Science**49**(4): 636-641.

[31] Miyauchi, S., H. Imoto, et al. (2016). "Fabrication of polymer-calcite composite thin films by phase transition of vaterite composite particles with octacarboxy-terminated T8-caged silsesquioxane." Polymer Journal**48**(10): 1019-1027.

[32] Gower, L. B. (2008). "Biomimetic model systems for investigating the amorphous precursor pathway and its role in biomineralization." Chemical reviews**108**(11): 4551-4627.

[33] Tanaka, Y. and K. Naka (2010). "A carbonate controlled-addition method for size-controlled calcium carbonate spheres by carboxylic acid-terminated poly (amidoamine) dendrimers." Polymer Journal**42**(8): 676-683.

[34] Antao, S. M. and I. Hassan (2010). "Temperature dependence of the structural parameters in the transformation of aragonite to calcite, as determined from in situ synchrotron powder X-ray-diffraction data." The Canadian Mineralogist**48**(5): 1225-1236.

[35] Hemley, R. J., C. T. Prewitt, et al. (1994). "High-pressure behavior of silica." Reviews in Mineralogy **29**: 41-41.

[36] Parkhomenko, E. I. (2013). Electrification phenomena in rocks, Springer Science & Business Media.

[37] Spearing, D. R., I. Farnan, et al. (1992). "Dynamics of the α-β phase transitions in quartz and cristobalite as observed by in-situ high temperature 29 Si and 17 O NMR." Physics and Chemistry of Minerals**19**: 307-321.

[38] Mason, B. and L. G. Berry (1968). Elements of mineralogy.

study by ICP-MS, electron spin resonance, cathodoluminescence, capillary ion analysis, and gas chromatography." <u>Geochimica et Cosmochimica Acta</u> **68** (18): 3741-3759.

[40] Rusk, B. G., M. H. Reed, et al. (2006). "Intensity of quartz cathodoluminescence and trace-element content in quartz from the porphyry copper deposit at Butte, Montana." <u>American Mineralogist</u> **91**(8-9): 1300-1312.

[41] Jourdan, A.-L., T. W. Vennemann, et al. (2009). "Evidence of growth and sector zoning in hydrothermal quartz from Alpine veins." <u>European Journal of Mineralogy</u> **21**(1): 219-231.

[42] Lehmann, K., A. Berger, et al. (2009). "Growth related zonations in authigenic and hydrothermal quartz characterized by SIMS-, EPMA-, SEM-CL-and SEM-CC-imaging." <u>Mineralogical Magazine</u> **73**(4): 633-643.

[43] Bambauer,*H.,* (1961). <u>Mineralogy and Petrology</u>. *Mitta.*41, 335.

[44] Dennen, W. (1967). "Trace elements in quartz as indicators of provenance." <u>Geological Society of America Bulletin</u> **78**(1): 125-130.

[45] Walenczak, Z. (1969). "Geochemistry of minor elements dispersed in quartz (Ge, Al, Ga, Fe, Ti, Li and Be)." <u>Archiwum Mineralogiezne</u> **28**: 189-335.

[46] Lyakhovich, V. (1972). "Trace elements in rock-forming minerals of granitoids." <u>Izd. Nedra, Moscow</u> **200**.

[47] Carretero-Genevrier, A., M. Gich, et al. (2013). "Soft-chemistry–based routes to epitaxial α-quartz thin films with tunable textures." <u>Science</u> **340**(6134): 827-831.

[48] Trolier-McKinstry, S. and P. Muralt (2004). "Thin film piezoelectrics for MEMS." <u>Journal of electroceramics</u> **12**: 7-17.

[49] Roy, S. S. (2016). "Characterization of copper oxide, titanium oxide and copper doped titanium oxide thin films prepared by spray pyrolysis technique."

[50] Kachroudi, A. (2016). Développement de nouveaux matériaux polymères pour micro-capteurs de vibrations, Université de Tunis El-Manar. Faculté des Sciences de Tunis (Tunisie).

[51] Le Dren, S. (2000). Elaboration de couches épaisses piézoélectriques déposées sur substrats pour des applications microtechniques, Lyon, INSA.

[52] Houf, L. (2011). Développement de nanocomposites à propriétés piézoélectriques et optiques non-linéaires, Université de Grenoble.

[53] Arıkan, F., R. Ulusay, et al. (2007). "Characterization of weathered acidic volcanic rocks and a weathering classification based on a rating system." Bulletin of Engineering Geology and the Environment **66**: 415-430.

[54] Mohammed, T. A. M. (2012). "Composition and phase mineral variation of Portland cement in Mass Factory Sulaimani Kurdistan Region NE-Iraq." International Journal of Basic and Applied Sciences **12**: 109-118.

[55] Penuel, B., O. Maitera, et al. (2017). "X-Ray Diffraction Characterization of Sedimentary Rocks in Demsa Local Government Area of Adamawa State, Nigeria." Current Journal of Applied Science and Technology **24**(2): 1-9.

[56] Al-Ghamdi, A. (2019). "X-ray diffraction and gamma-ray analysis of rock samples from Haradh Region in Saudi Arabia." Journal of Radiation Research and Applied Sciences **12**(1): 87-92.

[57] Abdelhedi, M., R. Jabbar, et al. (2020). "Ultrasonic velocity as a tool for geotechnical parameters prediction within carbonate rocks aggregates." Arabian Journal of Geosciences **13**: 1-11.

[58] Sabri, M. M. (2020). "Chemical and structural analysis of rocks using X-ray fluorescence and X-ray diffraction techniques." ARO-The Scientific Journal of Koya University **8**(1): 79-87.

[59] Bazzine, Z., A. Dobbi, et al. (2021). "Alteration effect on petrophysical properties of reservoirs rocks by drilling fluid emulsifiers." Journal of Petroleum Exploration and Production Technology **11**: 3203-3212.

[60] Dreybrodt, W. (1980). "Deposition of calcite from thin films of natural calcareous solutions and the growth of speleothems." Chemical Geology **29**(1-4): 89-105.

[61] Xu, G., N. Yao, et al. (1998). "Biomimetic synthesis of macroscopic-scale calcium carbonate thin films. Evidence for a multistep assembly process." Journal of the American Chemical Society **120**(46): 11977-11985.

[62] Kato, T. (2000). "Polymer/calcium carbonate layered thin-film composites." Advanced Materials **12**(20): 1543-1546.

[63] Hosoda, N. and T. Kato (2001). "Thin-film formation of calcium carbonate crystals: effects of functional groups of matrix polymers." <u>Chemistry of Materials</u> **13**(2): 688-693.

[64] Ajikumar, P. K., R. Lakshminarayanan, et al. (2004). "Controlled deposition of thin films of calcium carbonate on natural and synthetic templates." <u>Crystal growth & design</u> **4**(2): 331-335.

[65] Xu, X., J. T. Han, et al. (2004). "Formation of amorphous calcium carbonate thin films and their role in biomineralization." <u>Chemistry of Materials</u> **16**(9): 1740-1746.

[66] Medeiros, S., E. Albuquerque, et al. (2007). "Electronic and optical properties of CaCO3 calcite, and excitons in Si@ CaCO3 and CaCO3@ SiO2 core-shell quantum dots." <u>Journal of Physics D: Applied Physics</u> **40**(18): 5747.

[67] Oaki, Y., S. Kajiyama, et al. (2008). "Nanosegregated amorphous composites of calcium carbonate and an organic polymer." <u>Advanced Materials</u> **20**(19): 3633-3637.

[68] Hossain, F. M., G. E. Murch, et al. (2009). "Electronic, optical and bonding properties of CaCO3 calcite." <u>Solid state communications</u> **149**(29-30): 1201-1203.

[69] Li, C., G. Hong, et al. (2010). "Facile fabrication of honeycomb-patterned thin films of amorphous calcium carbonate and mosaic calcite." <u>Chemistry of Materials</u> **22**(10): 3206-3211.

[70] Sethmann, I., J. Wang, et al. (2010). "Strain-induced segmentation of magnesian calcite thin films growing on a calcite substrate." <u>Crystal growth & design</u> **10**(10): 4319-4326.

[71] Ayoub, A., A. Zaoui, et al. (2011). "High-pressure structural phase transitions and mechanical properties of calcite rock." <u>Computational Materials Science</u>**50**(3): 852-857

[72] Brik, M. (2011). "First-principles calculations of structural, electronic, optical and elastic properties of magnesite $MgCO_3$ and calcite $CaCO_3$." <u>Physica B: Condensed Matter</u> **406**(4): 1004-1012.

[73] Chahi, G., D. Bradai, et al. (2020). "Structural and elastic properties of CaCO3 hydrated phases: A dispersion-corrected density functional theory study." <u>Journal of Physics and Chemistry of Solids</u>**1 38**: 109295.

[74] Zhang, S. and Nahi, O., et al., (2022). Magnesium Ions Direct the Solid-State Transformation of Amorphous Calcium Carbonate Thin Films to Aragonite, Magnesium-Calcite, or Dolomite. Advanced Function Mater, 32: 2201394.

[75] Mokkath, J. H. (2022). "Impact of Adsorption of Straight Chain Alcohol Molecules on the Optical Properties of Calcite (10.4) Surface." Nanomaterials **12**(9): 1460.

[76] Hruska, C. K. and R. Brendel (1989). Determination of the third-order piezoelectric constants and electrostriction of alpha quartz using the thickness modes of plates. Proceedings of the 43rd Annual Symposium on Frequency Control, IEEE.

[77] Zeng, T., H. Doumanidis, et al. (2001). Growth of ultrathin silicon dioxide films during rapid-thermal oxidation. 9th International Conference on Advanced Thermal Processing of Semiconductors, RTP 2001, IEEE.

[78] Revesz, A. and H. Hughes (2003). "The structural aspects of non-crystalline SiO2 films on silicon: a review." Journal of Non-Crystalline Solids **328**(1-3): 48-63.

[79] Okudera, H. and A. Hozumi (2003). "The formation and growth mechanisms of silica thin film and spherical particles through the Stöber process." Thin Solid Films **434**(1-2): 62-68.

[80] Antao, S. M., I. Hassan, et al. (2008). "State-of-the-art high-resolution powder X-ray diffraction (HRPXRD) illustrated with Rietveld structure refinement of quartz, sodalite, tremolite, and meionite." The Canadian Mineralogist **46**(6): 1501-1509.

[81] Pierce, A. L., S. Sommakia, et al. (2009). "Thin-film silica sol–gel coatings for neural microelectrodes." Journal of Neuroscience Methods **180**(1): 106-110.

[82] Driver, K., R. Cohen, et al. (2010). "Quantum Monte Carlo computations of phase stability, equations of state, and elasticity of high-pressure silica." Proceedings of the National Academy of Sciences**107**(21): 9519-9524.

[83] Wang, F., Y. Tange, et al. (2012). "P-V-T equation of state of stishovite up to mid-lower mantle conditions." Journal of Geophysical Research: Solid Earth **117**(B6).

[84] Carretero-Genevrier, A., M. Gich, et al. (2013). "Soft-chemistry–based routes to epitaxial α-quartz thin films with tunable textures." Science **340**(6134): 827-831.

[85] Pabst, W. and E. Gregorová (2013). "Elastic properties of silica polymorphs–a review." Ceramics-Silikaty **57**(3): 167-184.

[86] Yang, R. and Z. Wu (2014). "Elastic properties of stishovite and the CaCl2-type silica at the mantle temperature and pressure: An ab initio investigation." Earth and Planetary Science Letters **404**: 14-21.

[87] Aramberri, H., R. Rurali, et al. (2017). "Thermal conductivity changes across a structural phase transition: the case of high-pressure silica." Physical Review B**96**(19): 195201.

[88] Uchino, K. (2017). Advanced piezoelectric materials: Science and technology, Woodhead Publishing.

[89] Fischer, R. A., A. J. Campbell, et al. (2018). "Equations of state and phase boundary for stishovite and CaCl2-type SiO2." American Mineralogist**103**(5): 792-802.

[90] Fonné, J. T., E. Burov, et al. (2018). "Aluminum-enhanced alkali diffusion from float glass to PVD-sputtered silica thin films." Journal of the American Ceramic Society **101**(4): 1516-1525.

[91] Zhang, Q., D. Sánchez-Fuentes, et al. (2019). "Tailoring the crystal growth of quartz on silicon for patterning epitaxial piezoelectric films." Nanoscale Advances **1**(9): 3741-3752.

[92] Zhang, Q., D. Sanchez-Fuentes, et al. (2019). "Micro/nanostructure engineering of epitaxial piezoelectric α-quartz thin films on silicon." ACS applied materials & interfaces **12**(4): 4732-4740.

[93] Molaei, F. and H. Siavoshi (2020). "Molecular dynamics studies of thermal conductivity and mechanical properties of single crystalline α-quartz." Solid state communications **320**: 114020.

[94] Ranieri, V. (2009). Amélioration des performances du quartz par substitution de germanium au silicium dans le réseau cristallin, Université Montpellier II-Sciences et Techniques du Languedoc.

[95] Saksala, T. (2021). "Cracking of granitic rock by high frequency-high voltage-alternating current actuation of piezoelectric properties of quartz mineral: 3D numerical study." International Journal of Rock Mechanics and Mining Sciences 147: 104891.

[96] Radi, Z., and Tlili, S., et al., (2023). Elastic properties of $SiO_2$ nanostructure in high-pressure conditions. Digest Journal of Nanomaterials and Biostructures, 18 pp: 263 – 272.

# Chapter two

# Materials and Methods

## II.1 Introduction:

In this chapter we have focused on products (Natural and commercial resources), solvents, there is also a discussion of the numerous characterization techniques used to examine and characterize the various characteristics of rock samples and grown thin films.

## II.2 Materials

Two types of starting product (commercial and natural resources) were used in thin films synthesis as describe below.

## II.2.1 Commercial Resources

The metals and the solvents have been used as commercial resources are listed in Table II.1.

*Table II.1:* List of commercial resources.

| Product | Formula | Molar Mass |
|---|---|---|
| **The Metals** | | |
| Serium carbonate | $SrCO_3$ | 147,63 g/mol |
| **The Solvents** | | |
| Distilled water | $H_2O$ | 18,01g/mol |
| Ethanol | $C_2H_5OH$ | 46,07 g/mol |
| Royal solution | $HNO_3HCl$ | |

## II.2.2 Natural Products (rocks)

## II.2.2.1 Collecting of Rocks

On the road between Ouargla and Hassi Messaoud, the rocks are found on the Earth's surface. The rocks were sampled in 2019 (Figure II.1-2). They were of different size, color and irregular shape as shown in (Figure II.3).
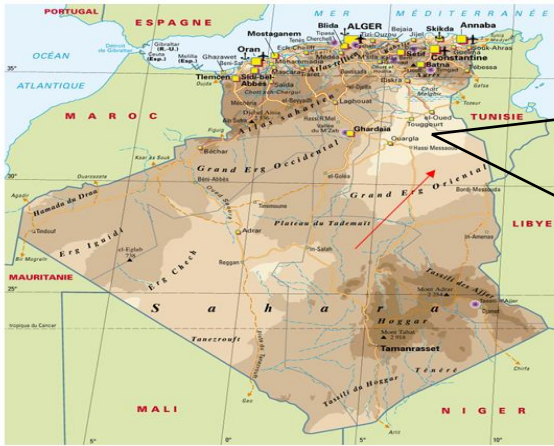
**Figure II.1:** Map of Algeria https://www.google. com/url?sa=i&url=http%3A%2F%2Fthesis.univ-biskra. Showing Ouargla region location
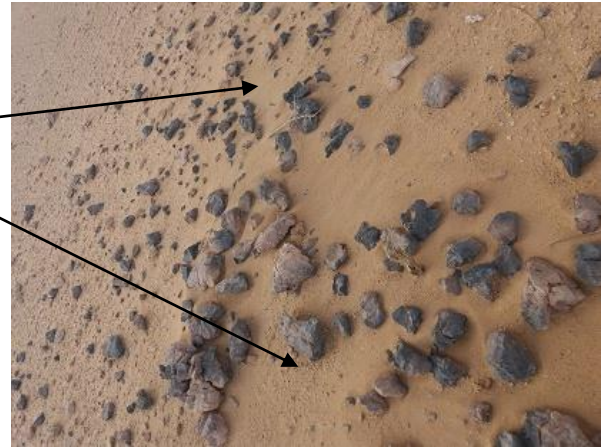
**Figure II.2:** An outline of the area from which the sample was brought



**Figure II.3:** The samples of studied rocks.

## II.2.2.2 Rock Polishing and Grinding

The collected rocks were cleaned, polished using a Mecapol P 255 U device to eliminate some impurities, and properly dried at room temperature before being crushed with a Retsch device for a short period of time (V= 950 rpm) to produce a powdery substance. The substance was then stored in a plastic box for later use.

## II.3 Methods

The devices which used in this work are:

## II.3.1 The mechanical polishing device

In the polishing process, a slurry containing abrasive grit and chemically reactive chemicals is used to smooth the top surface of a wafer. Both mechanical and chemical processes are involved in the polishing process. The mechanical's process component exerts

downward pressure, and the chemical reaction that results in faster material removal. The method is adjusted based on the kind of material being treated (Figure II.4, Annex ).

## II.3.2 The mechanical grinding device

Grinding or a grinding machine is a process that involves removing rough surfaces and smoothing them (Figure II.5, Annex).

## II.3.3 Autoclave

The thin film synthesis reaction was carried out in the autoclave by the hydrothermal method (Figure II.6, Annex). The advantages of this method are a higher synthesis temperature (our maximum hydrothermal temperature is 500°C) and temperature control, but its disadvantages are the internal pressure, which depends on the nature of the solvent and a significant temperature gradient.

## II.3.4 Electric oven

The electrical oven used is shown in (Figure II.7, Annex)

## II.3.5 Hydrothermal synthesis

Hydrothermal synthesis is a process that uses reactions in homogeneous or heterogeneous phase in aqueous medium at high temperature and pressure to crystallize materials directly from solution.

## II.4 Media Tools

## II.4.1 Used laptop

The laptop used in this work is DESKTOP-VIPGTFF (hp), it characterize by: Intel(R) Core(TM) i7-5600U CPU @ 2.60 GHz    2.60 GHz, 8.00 Go, 64-bit operating system, x64 processor.

## II.4.2 High-Score Plus Software

After identifying all the phases present in your sample with the Malvern Panalytical High-Score, you can continue to use this all-in-one software package with the Plus option to aid in your analysis. Whether you concentrate on figure processing, profile modification, or quantification with or without the Rietveld method, High-Score Plus is the solution that enables you to carry out your daily studies [1].

## II.4.3 Vesta program

VESTA is a 3D visualization program for crystal morphologies, electron/nuclear densities and structural models.

## II.5 Analysis techniques

X-ray diffraction (XRD), scanning electron microscopy (SEM-EDS) and infrared spectroscopy (FT-IR) were used to characterize the rock samples and the thin films that were produced. While the piezoelectric properties were measured using Polyk Quasi-Statie Piezoelectric Constant $d_{33}$ Meter device, we used also Raman measurements for the rock samples.

## II.5.1 Chemical analysis

## II.5.1.1 Fourier transform infrared spectroscopy (FT-IR)

A simple method known as infrared spectroscopy (FT-IR), which used for determine the chemical bands in organic, inorganic, crystalline or amorphous materials [2] and provide information on the kind of bonding that occurs between atoms in molecules.

## II.5.1.2 Principle of FT-IR

FT-IR is based on the absorption of infrared radiation by the material analyzed. It enables the analysis of the chemical functions existing in the material by detecting the distinctive vibrations of chemical bonds [3]. Absorption by a sample of infrared radiation affects the energy levels of the interatomic bonds of the phase's present [4].

The molecule whose vibration energy is close to the wavelength (energy) provided by infrared radiation will be absorbed, and also there will be a decrease in reflected or transmitted intensity as showing in Figure II.8 [5].
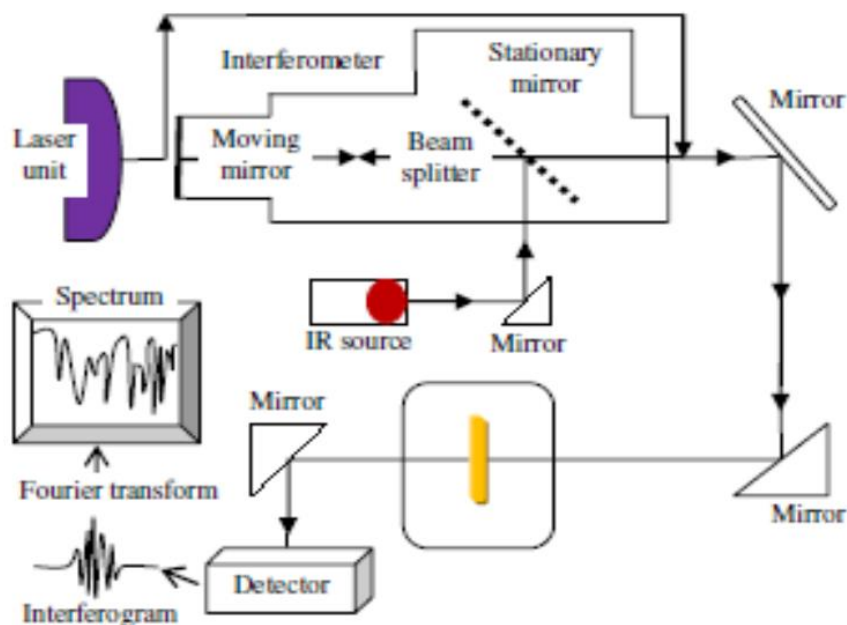
**Figure II.8:** Schematic diagram of FT-IR spectrophotometer

The information obtained from the spectra is of two kinds:

✓ Qualitative information: The chemical groups present in the material analyzed are characterized by the wavelengths in which the sample is absorbed, tables are also used to attribute the absorptions to the different chemical groups present where the same group can lead to several types of vibrations and therefore to absorptions at different frequencies [3]:

✓ Quantitative information: The concentration of the chemical group responsible for absorption is correlated with the strength of absorption at the characteristic wavelength [4].

## II.5.2 Structure study by Raman spectroscopy

The three-dimensional chemical and molecular structures of a sample can be known using the Raman spectroscopy technique. Chemistry and mineralogy are where it is primarily employed. The sample is exposed to laser light to accomplish this. The majority of the light beam enters the substance while only a little portion is dispersed. We can determine the chemical composition of the sample by analyzing the scattered light and looking for peaks at particular wavelengths that are different from the wavelength of the incident beam. We employed Raman spectroscopy to confirm the findings from FT-IR spectroscopy.

## II.5.2.1 Principle of Raman

In Raman spectroscopy, sample is illuminated with a monochromatic laser beam which interacts with the molecules of sample and originates a scattered light. The scattered light having a frequency different from that of incident light (inelastic scattering) is used to construct a Raman spectrum. Raman spectra arise due to inelastic collision between incident monochromatic radiation and molecules of sample. When a monochromatic radiation strikes at sample, it scatters in all directions after its interaction with sample molecules. Much of this scattered radiation has a frequency which is equal to frequency of incident radiation and constitutes Rayleigh scattering [6]. Schematic diagram of Raman spectrophotometer is showing in Figure II.9 [7].
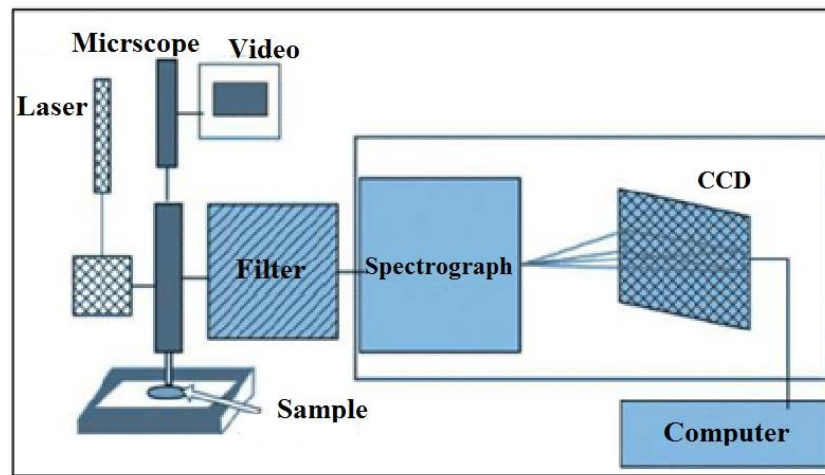


**Figure II.9:** Schematic diagram of Raman spectrophotometer

## II.5.3 Elemental analysis

By looking at the energy dispersive table or the net counts and net weight %, we can analyze the elemental percentage using energy dispersive X-ray spectroscopy (EDS), which is the elemental analysis of the sample. We can learn more about the components of the sample by looking at the EDS table.

## II.5.3.1 Energy dispersive X-ray spectroscopy (EDS)

The chemical composition of a solid item was examined using energy dispersive X-ray spectroscopy (EDS). While noting that the measurement depth does not exceed a few hundred nm [8]. The sample and the electron beam interact, an X-ray is produced that is detected. Additionally, it allows the mapping of the distribution of the various chemical components of the sample and any contaminants or particles can be retrieved as an addition to the SEM images [9, 10].

When an electron from a higher energy state bombards a sample, electron vacancies are filled and an X-ray is released to balance the two energy states. As a result, the electron is ejected from the atoms making up the sample surface. This characteristic of the X-ray beam corresponds to a particular elemental makeup. As a function of energy, the detector determines the relative frequency of X-rays that are released.

A charge sensitive preamplifier transforms the charge pulse that is created when an incident X-ray reaches the detector, which is correlated to the X-ray energy—into a voltage pulse (that still corresponds to the X-ray energy).

The pulses are then sorted by voltage on a multichannel analyzer after the signal has been sent there. A voltage measurement was used to determine the energy of each incident X-ray and the findings were promptly uploaded to a computer for visual display and additional analysis. It is predicted that the chemical elements of the sample can be identified from the X-ray energy spectrum versus counts [11], as it is showing in Figure II.10 [12].
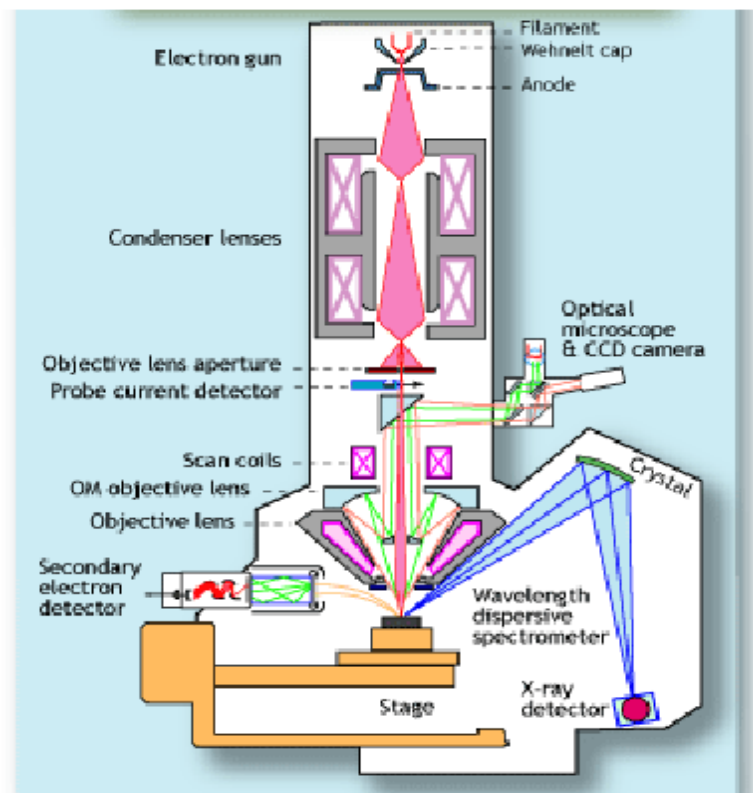


**Figure II.10:** Schematic diagram of Energy dispersion X-Ray spectroscopy (EDS)

## II.5.4 Surface characterization

## II.5.4.1 Scanning electron microscopy (SEM)

Using a high-energy electron beam by raster-scan the specimen surface, the SEM model of microscope produces images of the surface. The schematic diagram of SEM is presented from Figure II.11 [13]. It is a potent microscope that creates an image of items like broken metal pieces, employing electrons instead of light to separate foreign particles and residues, polymers, thin-film electrical components, biological samples, and countless others. Compared to conventional light microscopy's maximum magnification of roughly 2,000X, the shorter wavelength of electrons allows for picture magnifications of up to 100,000X. Additionally, compared to a light microscope, a SEM offers a broader field of view that keeps intricate, three-dimensional objects clear and in focus [14].
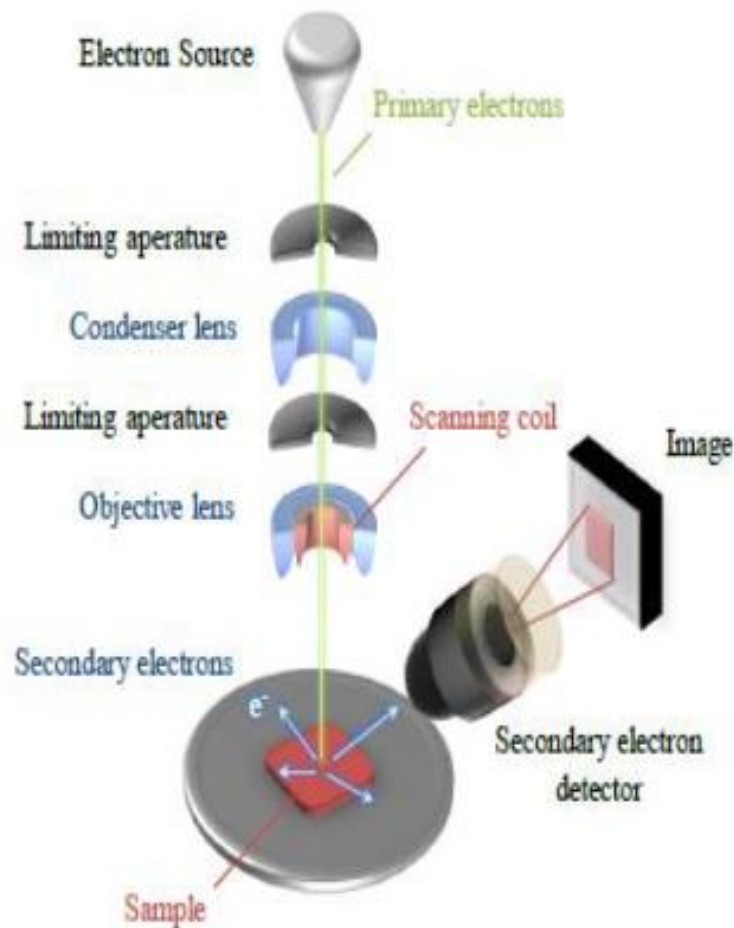
**Figure II.11:** Schematic diagram of scanning electron microscopy (SEM)

## II.5.4.2 Principle of operation of the SEM

The tungsten filament cathode-equipped electron cannon in a traditional SEM thermionically emits an electron beam. The electron beam is concentrated into a spot with a

diameter of between 0.4 and 5 nm using one or two condenser lenses and an energy range of merely a few hundred electron volts to 40 KeV.

The final lens in the electron column normally causes the beam to diverge in the x and y axes so that it scans in raster mode through a rectangular area of the sample. The electron column's electron beam subsequently passes through pairs of scanning coils or pairs of deviator plates. The electron's energy drop, the specimen's atomic number, and its density all affect how large the interaction volume is. The energy gap that forms between the sample and the electron beam is filled by secondary electron emission from inelastic scattering, with the aid of modern detectors, high-energy electron reflection and electromagnetic emission can all be discovered. Additionally, the beam current that is absorbed over the sample can be found and functionally altered to provide visualizations of the sample current distribution. To boost the signals, electronic amplifiers are used, which are visible as a shift in brightness on a cathode ray tube.

As a result of the CRT display's raster scanning being coordinated with the beam on the specimen in the microscope, the image created is a distribution drawing of the signal intensity radiating from the scanned surface of the specimen. Modern devices digitally capture and display the image, which was likely captured via photography from a high-resolution cathode ray tube [14].

## II.5.5 Structural characterization

# II.5.5.1 X-ray diffraction (XRD)

The Bragg's law, which he developed, allows scientists to infer the location of atoms within a crystal from the way an X-ray is diffracted by the crystal lattice. He made this discovery in 1912, his first year as a research student at Cambridge. In addition to his father, who built the X-ray spectrometer, he refined his concepts. Numerous forms of crystals can be analyzed with this method [15, 16]. The schematic diagram of the device is represented in Figure II.12 [17].

The crystal structure of NaCl and many other metal salts were discovered via X-ray analysis in 1913 by William Lawrence Bragg and his father Sir William Henri Bragg. The German physicist Röntgen developed various medical technologies based on these rays in 1895. In accordance with the size of an atom, these electromagnetic radiations have wavelengths on the order of the Angström (1 = $10^{-10}$ m).
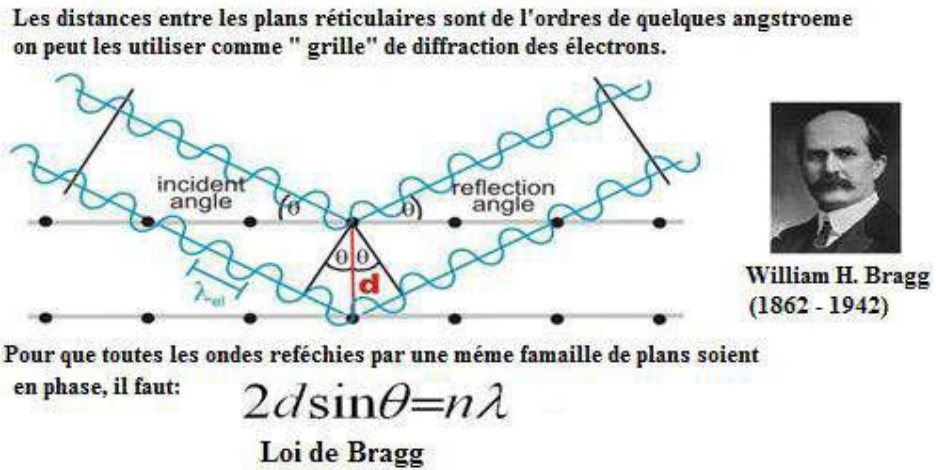
**Figure II.12:** Schematic diagram of DRX by a family of reticular planes: Bragg's law

## II.5.5.2 X-ray powder diffraction

X-ray powder diffraction is a powerful method of analysis, not destructive. It allows the qualitative and quantitative determination of the phases and their polymorphs and crystallinity [18], solve crystal structures from diagrams of powder [19], follow the evolution of the crystalline phases over time as a function of the temperature [20] for deduce the behavior of materials outside of industrial use.

## II.5.5.3 Identification of phases

To identifying phases, recorded diffractograms have been processed with the help of the High-Score Plus program by which are consulted the database (Crystallography Open Database (COD) standard data file and Inorganic Crystal Structure Database (ICSD) standards data file), that have been used for peak identification and selection of isostructural phases. Equations from Bragg's law are used to obtain the lattice parameters for the unit cell of the current phase. The lack of reflection peaks suggests that the material is amorphous [21].

## II.5.5.3.1 Structural Parameters

## Interplanar spacing

The following formula was used to determine interplanar distance $d_{hkl}$ from X-ray diffraction profiles:

$$2 \times d \times \sin\theta = n \times \lambda \qquad\qquad (II.1)$$

Where $\lambda$ is the employed X-ray wavelength, n is the order of diffraction and $\theta$ is the diffraction angle.

The sequence of lattice planes (h k l) were found from standard data using d values. When the Bragg condition is met, strong peaks are anticipated. The following formula can be used to calculate the lattice parameter values for various crystallographic systems [22].

- Cubic systems

$$\frac{1}{d^2} = \frac{h^2+k^2+l^2}{a^2}$$ (II.2)

- Tetragonal systems

$$\frac{1}{d^2} = \frac{h^2+k^2}{a^2} + \frac{l^2}{a^2}$$ (II.3)

- Hexagonal systems

$$\frac{1}{d^2} = \frac{4(h^2+hk+k^2)}{3a^2} + \frac{l^2}{c^2}$$ (II.4)

- Othorhombic systems

$$\frac{1}{d^2} = \frac{h^2}{a^2} + \frac{k^2}{b^2} + \frac{l^2}{c^2}$$ (II.5)

## II.5.5.3.2 Cristallite size (Grain size)

The Scherrer formula can be used to determine the crystallite or grain size of samples:

$$D = \frac{0.9\lambda}{\beta cos\theta}$$ (II.6)

where D is the mean crystallite size, which supposedly equal or smaller to the grain size, Bragg angle $\theta$ in radians, $\beta$ is the line broadening at half maximum intensity (FWHM) in radians and $\lambda$ is the wavelength applied for X-ray of ($\lambda$ = 1.5406Å) [22].

## II.5.6 Measurements of piezoelectric coefficient $d_{33}$

Many methods have been applied in the past to characterize the piezoelectric coefficient $d_{33}$ including:

An alternative PFM mode, direct piezoelectric force microscopy (DPFM), recently developed by Gomez et al. [23]. A piezoelectric d33-meter (Piezotest PM 200) at a frequency of 100 Hz [24], also a $d_{33}$-meter (YE2730A) [25]; high precision PM300 Piezometer, Piezosystems, at

110 Hz and a static and dynamic force of 10 N and 0.25 N respectively [26] and the piezometer method in the Piezotest (PM200) at 100 Hz and a dynamic force of 1 N [27]

The direct piezoelectric measurements of our quartz rocks and their thin films were estimated using Polyk Quasi-Statie Piezoelectric Constant $d_{33}$ Meter ($d_{33}$ Piezometer) device at Applied Physics Laboratory of Science Faculty in Sfax University. The device is characterized by: Dynamic Force 250 mN, Frequency 110 Hz, resolution 0.1 pC/N and range 1-200 pC/N.

The piezoelectric effect reflects the coupling between mechanical effects and electrical effects. The value of $d_{33}$ is obtained with the following relation [27]:

$$\mathbf{d_{33}} = \frac{q}{F} \qquad\qquad\qquad (\text{II}.7)$$

q: the electric charge (pC)

F: force (N)

# Reference
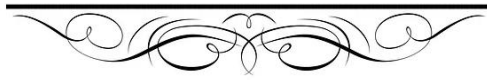
# Reference

[1] ChemSketch, version (2022).1.2, Advanced Chemistry Development, Inc. (ACD/Labs), Toronto, ON, Canada, www.acdlabs.com

[2] Reig, F. B., J. G. Adelantado, et al. (2002). "FTIR quantitative analysis of calcium carbonate (calcite) and silica (quartz) mixtures using the constant ratio method. Application to geological samples." Talanta **58**(4): 811-821.

[3] A. Samiya, A. (2015). Elaboration and characterization of composite materials based on nanoparticles of the semiconductor CuO and the rare earth oxide Dy2O3 dipersed in the dielectric matrices KBr, KCl and NaCl, ph. D. Thesis, University of Constantine.

[4] Haure, T. (2003). "Multi-functional layers developed by several techniques." Multifunctional Layers by Multitechnique Process, PhD. Thesis, Fachlty of Sciences, University of Limoges, France.

[5] S. Kumar, S. (2014). Structural, morphological, optical and magnetic properties of Pure and transition metal doped cadmium sulphide nanofilms at room temperature, PhD. Thesis, Jaypee University of Information Technoloy, Solan.

[6] Bumbrah, G. S. and R. M. Sharma (2016). "Raman spectroscopy–Basic principle, instrumentation and selected applications for the characterization of drugs of abuse." Egyptian Journal of Forensic Sciences **6**(3): 209-215.

[7] Colomban, P. (2002). "Imagerie Raman de matériaux et dispositifs hétérogènes." Techniques de l'Ingénieur 4: 1-13.

[8] Habiba and Amaara. B (2013). The effect of substrate temperature and molarity on the properties of zin sulfide thin films deposited by ultrasonic spray, Mohamed Khider-Biskra University.

[9] A. Douayar, A. (2013). Contribution to the study of the structural, optical and electrical properties of thin layers of doped zinc oxide (ZnO) (fluorine, indium, aluminum and neodymium), PhD. Thesis, University of Rabat.

[10] Benkara, S. S. (2014). Study of the electronic and photonic properties of thin layers based on nanostructured oxides, Ph. D. Thesis, University of Skikda.

[11] Ghosh, A. (2010). Growth and effect of Shi irradiation on structural and opto-electricalproperties of nanocrystalline pure and doped zinc oxidesemiconductorthin film for gassensor application, PhD. Thesis, Babasahebambedkar Marathwada University.

[12] http://www.mcswiggen.com/TechNotes/WDSvsEDS.htm

[13] Yaacob, M. H. (2012). Investigation of metal oxide nanostructured thin films based optical hydrogen sensors, RMIT University.

[14] Sharmin, M. (2015). "Characterization of boron doped zinc oxide thin films prepared by spray pyrolysis deposition technique."

[15] Bragg, W. H. (1912). "X-rays and crystals." Nature **90**(2243): 219-219.

[16] Bragg, W. L. (1913). "The structure of some crystals as indicated by their diffraction of X-rays." Proceedings of the Royal Society of London. Series A, Containing Papers of a Mathematical and Physical Character **89**(610): 248-277.

[17] Hirose, S., M. A. M. Aoyagi, et al. (1993). "Dielectric loss in a piezoelectric ceramic transducer under high-power operation; increase of dielectric loss and its influence on transducer efficiency." Japanese journal of applied physics **32**(5S): 2418.

[18] Glasser, F. P. (1998). "The burning of Portland cement." Lea's chemistry of cement and concrete**240**.

[19] Louër, D. (1996). "La diffraction des rayons X par les poudres cent ans après Röntgen." Le Journal de Physique IV**6**(C4): C4-57-C54-69.

[20] Erer, H., O. Z. Yeşilel, et al. (2010). "One-dimensional coordination polymers of Co (II) and Cd (II)-squarate with 2-methylimidazole and 4 (5)-methylimidazole ligands." Polyhedron **29**(3): 1163-1167.

[21] Neves, N. M. P. (2015). "Al-doped ZnO ceramic sputtering targets based on nanocrystalline powders produced by emulsion detonation synthesis–deposition and application as a transparent conductive oxide material."

[22]Ragina, A. (2012). "Preparation and characterization of tin based semiconducting thin films."

[23] Gomez, A., M. Gich, et al. (2017). "Piezo-generated charge mapping revealed through direct piezoelectric force microscopy." Nature communications **8**(1): 1113.

[24] Lidjici, H., B. Lagoun, et al. (2015). "XRD, Raman and electrical studies on the (1−x)(Na0. 5Bi0. 5) TiO3− xBaTiO3 lead free ceramics." Journal of alloys and compounds **618**: 643-648.

[25] Turki, O., A. Slimani, et al. (2019). "Enhancement of dielectric, piezoelectric, ferroelectric, and electrocaloric properties in slightly doped (Na0. 5Bi0. 5) 0.94 Ba0. 06TiO3 ceramic by samarium." Journal of Applied Physics **125**(17).

[26] Khanbareh, H., S. van der Zwaag, et al. (2017). "In-situ poling and structurization of piezoelectric particulate composites." Journal of Intelligent Material Systems and Structures **28**(18): 2467-2472.

[27] HADJADJ, S. Élaboration et caractérisation diélectrique de céramique ferroélectriques à structure pérovskite complexe, Université de Kasdi Merbah Ouargla.

# Chapter three

# Characterizations of rocks
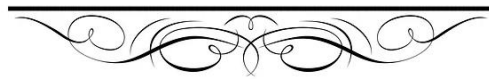
## III.1 Introduction

In this chapter we have focused on characterization of rocks and discussed their analysis by using infrared spectroscopy (FTIR), Raman measurements, energy dispersive X-ray spectroscopy (EDS), X-ray diffraction (XRD) and piezoelectric measurements.

## III.2 Characterization of rocks

The structural characteristics of rocks were examined using the X-ray diffractometer BTX-716. Using K radiation from a room-temperature copper anticathode ($\lambda = 1,5406$ Å), running at 40 KV and a current of 40 mA. A step of 0.0500 °/s and 250 exposures were used to evaluate all samples from 5 ° to 55 °. The expert High-Score Plus software [1] set with the COD and ICSD file were used to identify the phase's structural elements. In order to study the microstructure and elemental composition of our sandstones, SEM-EDS diffractometer TESCAN VEGA3 was used. An Agilente Cary 660 FT-IR spectrometer was used to record the functional group that was present in the sample between the wavelengths of 4000 to 400 cm$^{-1}$ and LabRAM HR 800, excitation: red laser wavelength 633 nm for Raman measurements. To measure the piezoelectric $d_{33}$ coefficients, to provide this effect in rocks was recorded using Piezoemeter device with dynamic force 250 mN, frequency 110 Hz, range 1-200 pC/N and resolution 0.1 pC/N. (Figures III.1, 2, 3, 4 and 5, Annex ).

## III.3 Analysis of rocks
## III.3.1 Fourier-transform infrared (FT-IR) analysis

The quality and composition of the rock samples were examined by FT-IR qualitative analysis to support the XRD findings. By comparing our findings to those of other studies, we found that the vibration bonds values obtained were well in agreement with those found in the literature [2- 4], indicating that the majority of the bands are attributed to quartz and calcite as shown in Figure III.6 and as indicated in Table III.1.

All rock samples contain quartz, as shown by the absorption peaks measured between 425.14 and 429.47 cm$^{-1}$, 440.49 and 449.81 cm$^{-1}$, 467.13 and 483.19 cm$^{-1}$, 693.9 and 694.004 cm$^{-1}$, and 777.17 and 798.38 cm$^{-1}$ in Figure III.5. With the exception of OH7, none of the samples had the characteristic peaks between 1081.85 and 1096.83 cm$^{-1}$ and 2357.08 and 2361.79 cm$^{-1}$ that revealed to the formation of carbonate ions of of calcite [2, 5].

The symmetrical stretching of the Si-O-Si bond appears to match with the strong absorption band that has been seen between 1081.85 and 1096.83 cm$^{-1}$ [4, 6, 7]. The

characteristic peaks at 1088 and 1090 cm$^{-1}$, which point to the formation of carbonate ions [5] and the vibrations of the carbonate ions [7] respectively, have been reported by Flemming A. Andersen (1991) and Chengli Yao (2013).
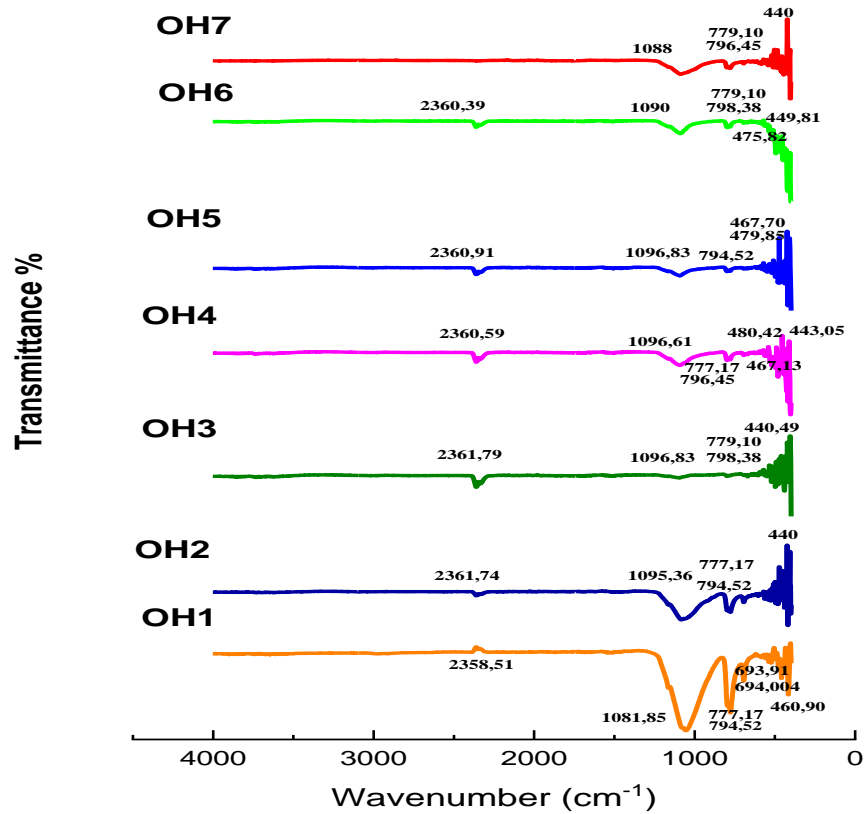


**Figure III.6:** FT-IR transmittion spectrum of OH1-OH7 sandstones

The observed absorption bands between 777.17 and 798.38 cm$^{-1}$, which are associated with Si-O symmetrical bending vibration, provide further evidence of the existence of α-SiO$_2$ [3, 4]. Also, we found other bands that correlate with Si-O-Si symmetrical bending in the range 693.91-694.004 cm$^{-1}$. These peaks provide more evidence that quartz was present in our samples. In all samples, quartz is crystalline according to 694.004 cm$^{-1}$ band [8]. The asymmetrical vibrations of Si-O-Al, symmetrical stretching of Si-O, asymmetrical bending of the Si-O-Si band and bending vibrations of Si-O-Fe, respectively, cause the absorption peaks between 500 and 530 cm$^{-1}$, 467.13 and 483.19 cm$^{-1}$, 440.49 and 449.81 cm$^{-1}$ and 425 and 429.47 cm$^{-1}$ [4, 9-11].

**Table III.1:** Sandstone's primary IR absorption bands and related bond vibration

| Band ($cm^{-1}$) | Bond (vibration mode) | Compound |
|---|---|---|
| 2357.08-2361.79 | $CO_3^{-2}$ (indicating the emergence of calcite) | Calcite |
| 1081.85-1096.83 | Si–O–Si (symmetrical stretching) | Quartz |
| 1088 | $CO_3^{-2}$ (indicating the emergence of calcite) | Calcite |
| 1090 | vibrations of the carbonate ions | Calcite |
| 777.17-798.38 | Si-O (symmetrical bending vibration) | Quartz |
| 693.91-694.004 | Si–O–Si (symmetrical bending) | Quartz |
| 694.004 | Quartz bonds | Quartz |
| 467.13-483.19 | Si-O (symmetrical streching) | Quartz |
| 440.49-449.81 | Si-O-Si (asymmetrical bending) | Quartz |
| 425.14-429.47 | Si-O-Fe (bending vibrations) | Quartz |

## III.3.2 Spectroscopy Raman characterization

Figure III.7 is represented by the Raman spectra resulting from the sandstones (OH1-OH7) studied and after disposing of the sixth sample (OH6). Raman measurements indicated only the maximum acute values in intensity appeared at approximately 500 $cm^{-1}$ before 600 $cm^{-1}$, this spectrum was not caused by bonds but rather by the rotation of a part containing carbon atoms.
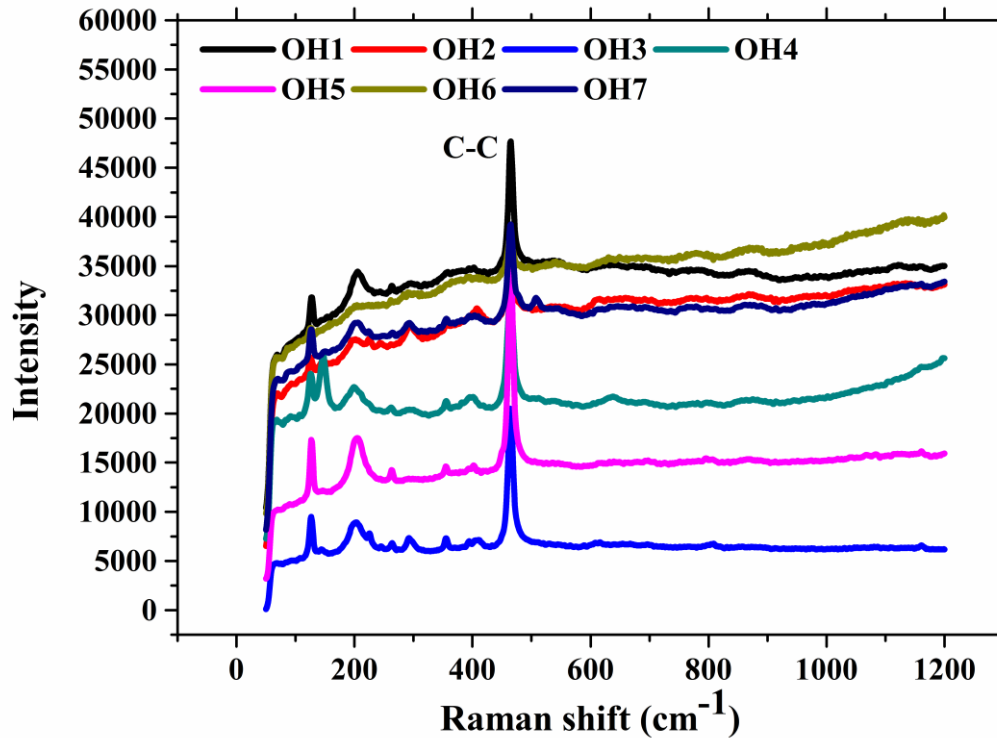
**Figure III.7:** Shows the Raman spectra of OH1-OH7 sandstones

## III.3.3 Energy dispersive spectrometry analysis (EDS)

The qualitative and quantitative compositin that make up our sandstones (OH1-OH7) found via energy dispersive spectrometric (EDS) analysis, as well as whether secondary phases are present or not. The Table III.2 and Figure III.8 (more details about it are listed in Table III.3) provide a summary of the analytical findings for all samples. The similar significant elements (O, Si, C, and Ca) found in some samples confirm the presence of the rocks' native quartz/calcite structure. While there were noticeable changes in the presence and concentrations of particular trace metals (Na, Al, K, Fe, and Ag) for each sample with the exception of rock 7, this suggests that the quartz/calcite structure may have been altered. These components Na, K, Al, and Li are some of the most impurities found in hydrothermal $SiO_2$ according to research done by Shanling, Qing and Jun in southern China [12].

It is obvious that the rock 7 is pure that is a result of a superficial observation of the EDS, but there is a possibility of some impurities but the EDS did not detect them.

**Table III.2:** Analysis of the elements in (OH1-OH7) sandstones

| Samples | O (%) | Si (%) | C (%) | Fe (%) | Al (%) | Ag (%) | Na (%) | K (%) | Ca (%) |
|---------|-------|--------|-------|--------|--------|--------|--------|-------|--------|
| OH1 | 66.59 | 21.65 | 9.97 | 0.85 | 0.55 | 0.41 | | | |
| OH 2 | 67.69 | 31.28 | | 0.36 | 0.67 | | | | |
| OH 3 | 61.83 | 25.39 | 9.48 | 1.70 | 1.13 | | 0.47 | | |
| OH 4 | 61.88 | 22.86 | 11.94 | 1.75 | 0.89 | | | | 0.68 |
| OH 5 | 68.66 | 24.51 | | 0.74 | 2.98 | | 1.77 | 0.90 | 0.44 |
| OH 6 | 61.32 | 36.69 | | 1.20 | 0.35 | | | | 0.44 |
| OH 7 | 61.87 | 1.46 | 19.54 | | | | | | 17.14 |

**Table III.3:** Elemental analysis more details of OH1-OH7 sandstones

```
El AN  Series  unn. C norm. C Atom. C Error (1 Sigma)
               [wt.%]  [wt.%]  [at.%]          [wt.%]
       -------------------------------------------------
O   8  K-series  47.50   56.08   66.58           5.67
Si 14  K-series  27.11   32.01   21.65           1.18
C   6  K-series   5.34    6.30    9.97           1.19
Fe 26  K-series   2.12    2.50    0.85           0.10
Ag 47  L-series   1.97    2.33    0.41           0.10
Al 13  K-series   0.66    0.78    0.55           0.06
       -------------------------------------------------
       Total:  84.70  100.00  100.00
```

OH1

```
El AN  Series  unn. C norm. C Atom. C Error (1 Sigma)
               [wt.%]  [wt.%]  [at.%]          [wt.%]
       -------------------------------------------------
O   8  K-series  38.38   54.15   67.69           4.66
Si 14  K-series  31.14   43.93   31.28           1.36
Fe 26  K-series   0.72    1.01    0.36           0.06
Al 13  K-series   0.64    0.90    0.67           0.06
       -------------------------------------------------
       Total:  70.88  100.00  100.00
```

OH2

```
El AN   Series   unn. C norm. C Atom. C Error (1 Sigma)
                  [wt.%]  [wt.%]  [at.%]            [wt.%]
---------------------------------------------------------
O  8   K-series   35.56   50.66   61.83              4.34
Si 14  K-series   25.64   36.52   25.39              1.12
C  6   K-series    4.09    5.83    9.48              1.01
Fe 26  K-series    3.41    4.86    1.70              0.13
Al 13  K-series    1.10    1.57    1.13              0.08
Na 11  K-series    0.39    0.55    0.47              0.06
---------------------------------------------------------
```

```
El AN   Series   unn. C norm. C Atom. C Error (1 Sigma)
                  [wt.%]  [wt.%]  [at.%]            [wt.%]
---------------------------------------------------------
O  8   K-series   40.39   51.45   61.88              4.90
Si 14  K-series   26.19   33.36   22.86              1.14
C  6   K-series    5.85    7.45   11.94              1.29
Fe 26  K-series    3.98    5.07    1.75              0.15
Ca 20  K-series    1.11    1.42    0.68              0.07
Al 13  K-series    0.98    1.25    0.89              0.08
---------------------------------------------------------
       Total:     78.50  100.00  100.00
```

0H4

```
El AN   Series   unn. C norm. C Atom. C Error (1 Sigma)
                  [wt.%]  [wt.%]  [at.%]            [wt.%]
---------------------------------------------------------
O  8   K-series   38.14   54.87   68.66              4.61
Si 14  K-series   23.90   34.38   24.51              1.05
Al 13  K-series    2.79    4.02    2.98              0.16
Fe 26  K-series    1.43    2.06    0.74              0.08
Na 11  K-series    1.41    2.04    1.77              0.13
K  19  K-series    1.22    1.76    0.90              0.07
Ca 20  K-series    0.61    0.88    0.44              0.05
---------------------------------------------------------
       Total:     69.51  100.00  100.00
```

0H5

```
El AN   Series    unn. C norm. C Atom. C Error (1 Sigma)
                   [wt.%]  [wt.%]  [at.%]            [wt.%]
-------------------------------------------------------------
Si 14  K-series    36.85   48.94   36.69              1.60
O   8  K-series    35.09   46.59   61.32              4.40
Fe 26  K-series     2.40    3.18    1.20              0.10
Ca 20  K-series     0.63    0.84    0.44              0.05
Al 13  K-series     0.34    0.45    0.35              0.05
-------------------------------------------------------------
       Total:      75.31  100.00  100.00
```
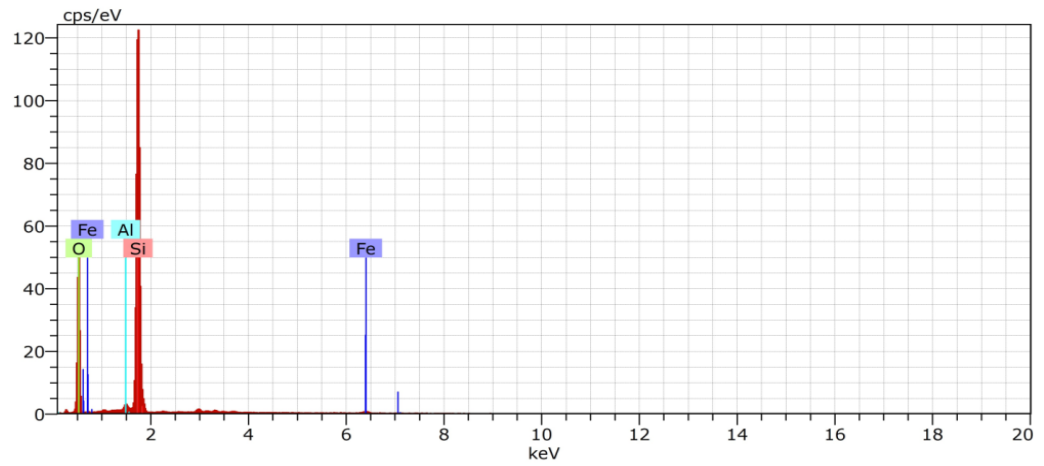
0H6

```
El AN   Series    unn. C norm. C Atom. C Error (1 Sigma)
                   [wt.%]  [wt.%]  [at.%]            [wt.%]
-------------------------------------------------------------
O   8  K-series    53.01   50.71   61.87              6.81
Ca 20  K-series    36.77   35.18   17.14              1.10
C   6  K-series    12.56   12.02   19.54              1.90
Si 14  K-series     2.19    2.10    1.46              0.12
-------------------------------------------------------------
       Total:     104.53  100.00  100.00
```
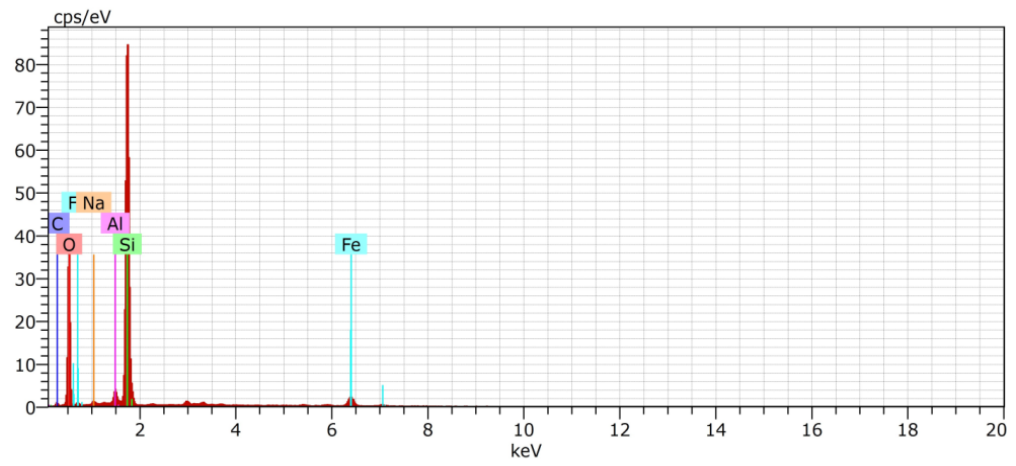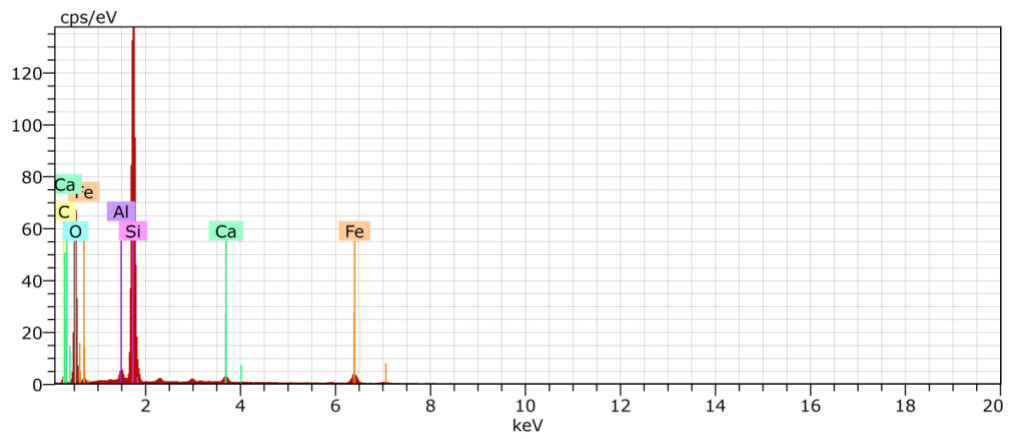
OH7



OH1

OH2



OH3



OH4

OH5



OH6



OH7
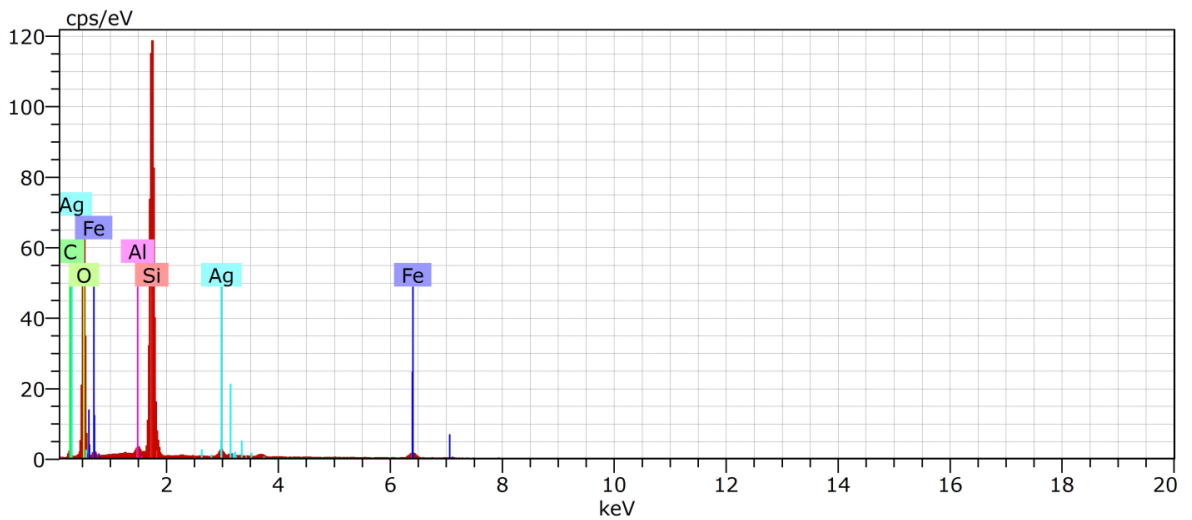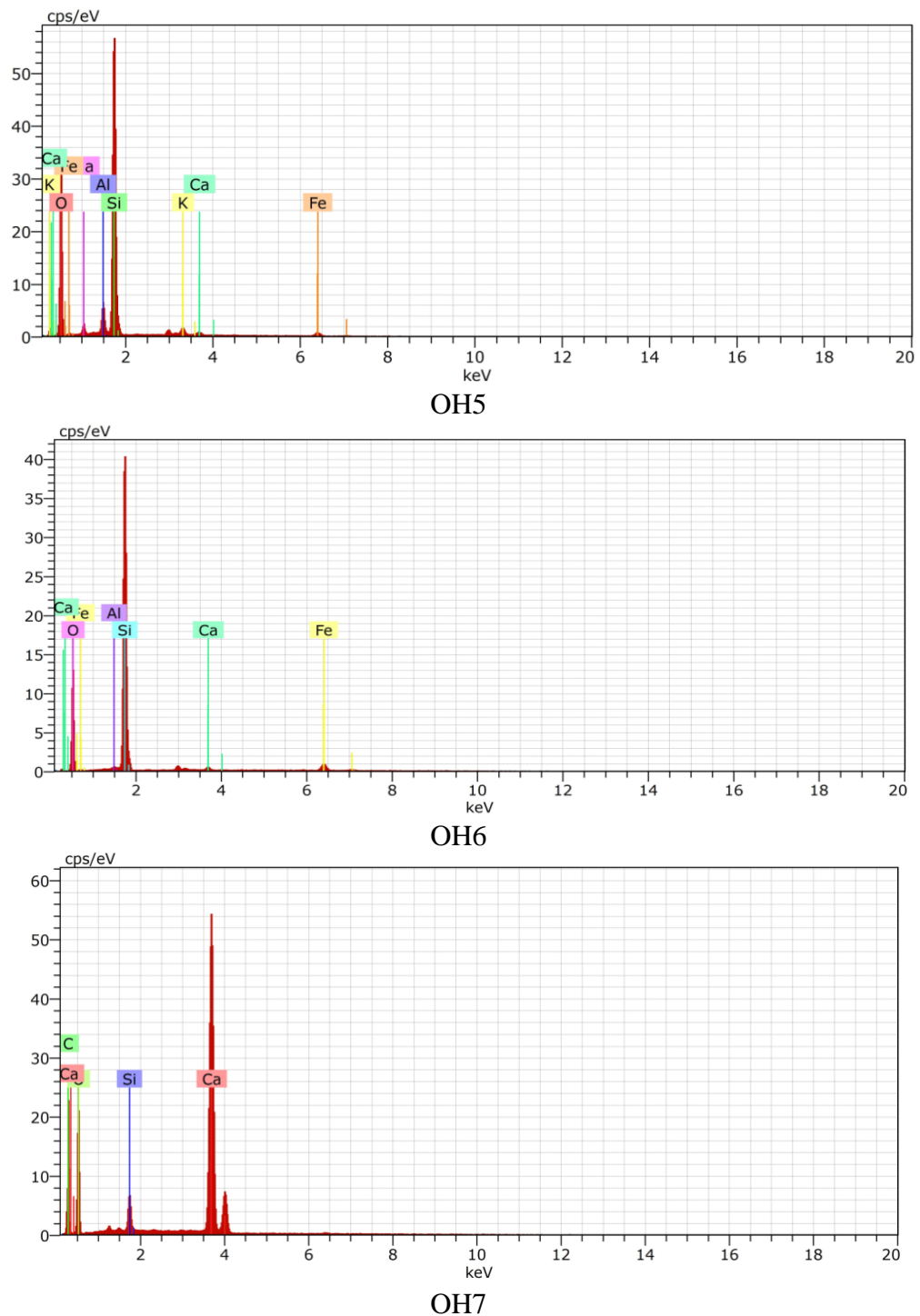
**Figure III.8:** Spectra of elemental analysis of (OH1-OH7) sandstones

## III.3. 4 X-ray diffraction (XRD) analysis

In order to ascertain the rock structure, XRD tests were conducted on the sandstones (OH1-OH7) to estimate the qualitative and quantitative phase analysis. Strong diffraction peaks in the observed XRD show that the sandstones (OH1-OH7) are highly crystalline, which is consistent with the findings of Meftah and Mahboub 2020 [14]. According to Figure III.9 and Tables (III.3, III.4, III.5, III.6, III.7, III.8 and III.9) the findings of the X-pert High-

Score software matching revealed that the majority of the rock samples included quartz and that the remainder contained calcite.

Figures III.9, 10 and Figure IV.11 show the crystalline structures of quartz ($SiO_2$), calcite ($CaCO_3$) and sodium chloride ($NaCl$), respectively, which draw them by using Vesta program, by downloaded crystallography international file (cif) from Crystallography Open Database (COD) standard data file.
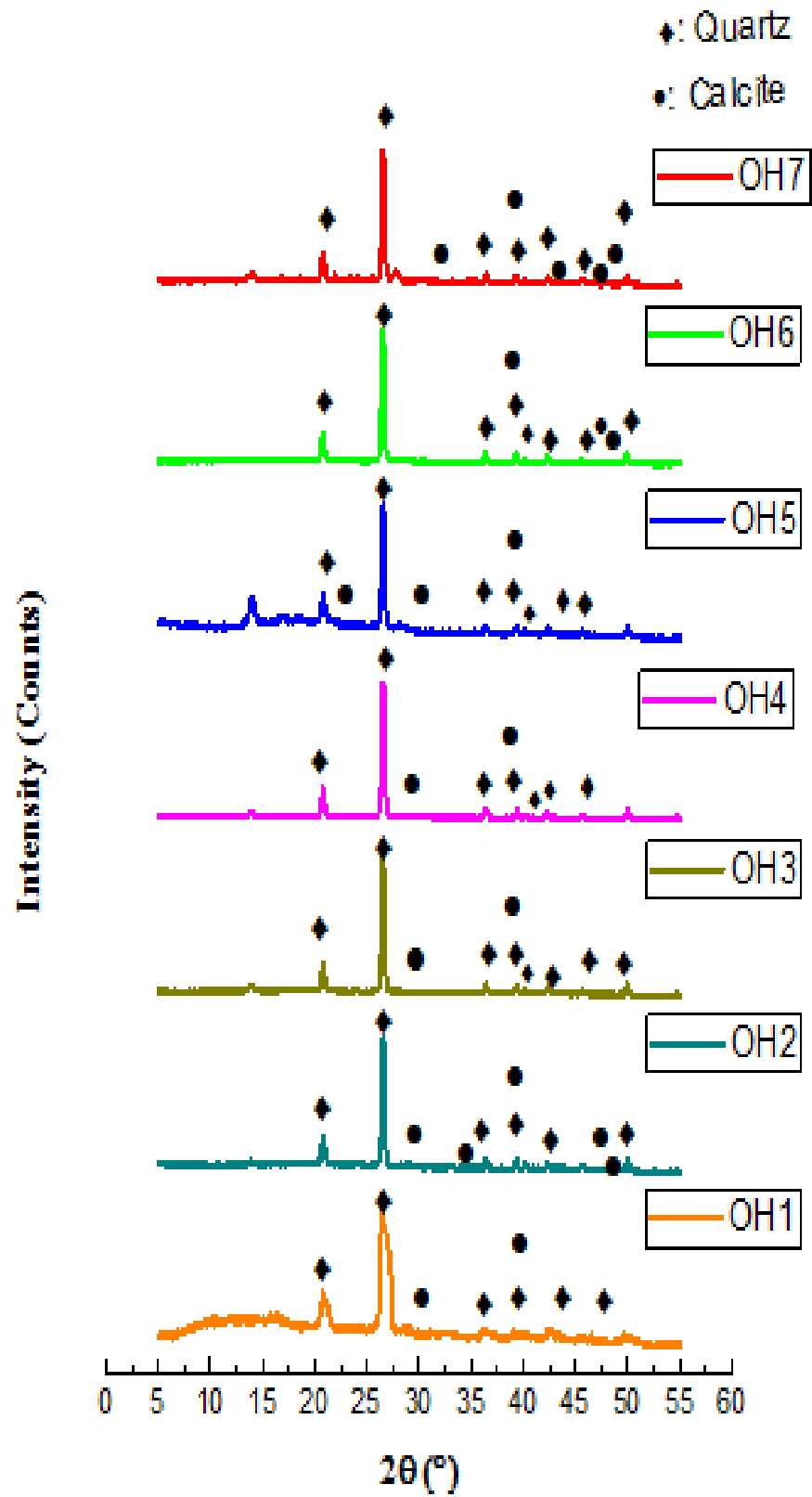
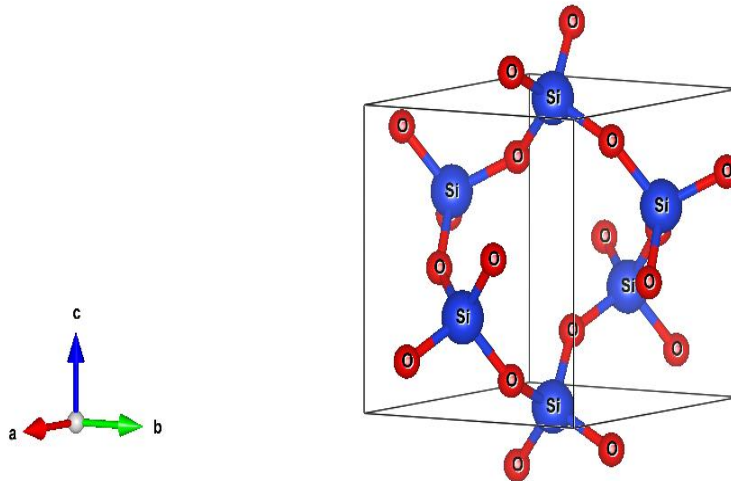**Figure III.9:** The XRD pattern of OH1-OH7 sandstones

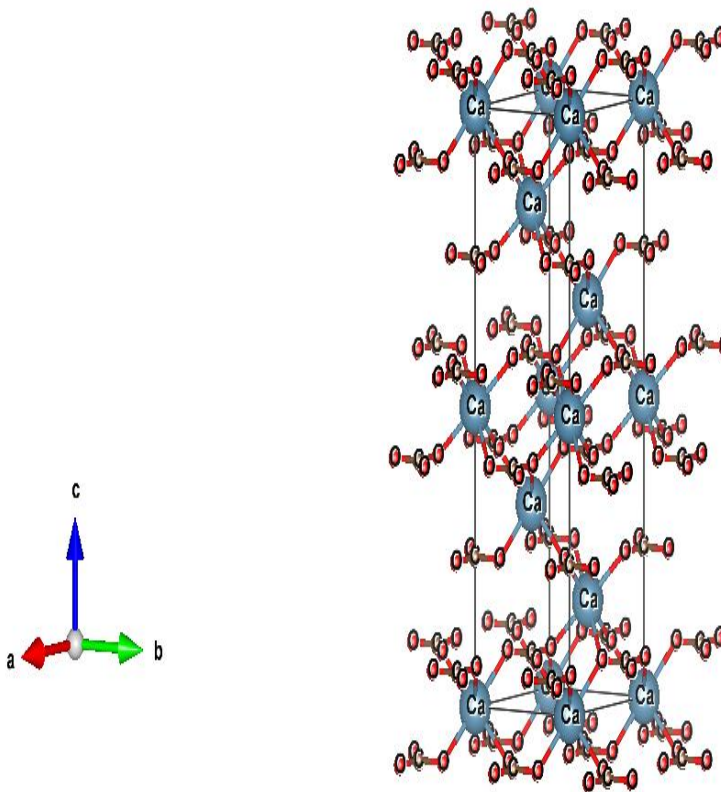**Figure III.10:** Structure crystalline of $SiO_2$



**Figure III.11:** Structure crystalline of $CaCO_3$

**Table III.4:** Indexed Powder XRD Pattern for OH1 sandstones

| 2θ(°) | Intensity (a.u) | Mineral | $(d_{hkl})$ cal (Å) | Hkl |
|---|---|---|---|---|
| 20.7709 | 1556.38 | Quartz | 4.27305 | 100 |
| 26.5832 | 5789.14 | Quartz | 3.35048 | 101 |
| 29.2773 | 443.325 | Calcite | 3.04801 | 104 |
| 31.5967 | 324.419 | Calcite | 2.82935 | 006 |
| 35.8935 | 279.252 | Calcite | 2.49989 | 110 |
| 36.4035 | 635.429 | Quartz | 2.46603 | 110 |
| 39.3111 | 682.268 | Quartz, Calcite | 2.29007 | 102/113 |
| 40.2535 | 385.766 | Quartz | 2.23860 | 111 |
| 42.3029 | 555.187 | Quartz | 2.13477 | 200 |
| 47.1143 | 244.788 | Calcite | 1.92737 | 024 |
| 48.6941 | 221.515 | Calcite | 1.86847 | 116 |
| 49.9412 | 613.894 | Quartz | 1.82469 | 112 |

The following observations can be made by comparing the COD cards to the reported XRD peaks (Table III.4):

The space group P3221 (154) is attributed to the hexagonal crystal structure of $SiO_2$, which is responsible for the peaks at 2θ = 20.7709°, 26.5832°, 36.4035°, 39.3111°, 40.2535°, 42.3029°, and 49.9412°. The diffraction angles for the crystallographic planes (104), (006), (110), (113), (024), and (116) are 2θ = 29.2773°, 31.5967°, 35.8935°, 39.3111°, and 48.6941°, respectively, which correspond to the R3c (167) space group's rhombohedral crystal structure of calcite ($CaCO_3$) [15-17]. These structures are consistent with COD file

The greatest, highest intensity and most noticeable diffraction of quartz is at 2θ= 26.5832°, whereas calcite has its maximum intensity and most noticeable diffraction at 2θ= 29.2773. Additionally, the presence of various percentages of metal traces in the crystal lattice of the rocks, known as defects, which affect the crystal size and consequently the d-spacing between lattice planes, can be the cause of the right or left shifts at the 2θ positions of the peaks (26.5832°, 26.5548°, 26.5773°, 26.5544°, 26.5409° and 26.5598°) in whole samples. If they are tiny, the metal traces may be interstitial or may occupy the locations of replacement atoms [18, 19]. The results of the energy dispersive spectrometry and Fourier-transform

infrared analysis for Si-O-Al at 500–530 cm$^{-1}$ and Si-O-Fe at 425–429.47 cm$^{-1}$, respectively, support it.

The spacing distances d$_{hkl}$ of 4.27305, 3.35048 and 2.46603 (Å) / 3.04801, 2.82935 and 2.49989 (Å), respectively, support the existence of the α-quartz phase, as shown in Table III.3 and calcite in whole samples. To acquire data that supports the same findings, the same computations were conducted for all the rocks in the same manner. The same notes are recorded for the other tables (III.4, 5, 6, 7, 8 and 9) but there are a little difference in values.

**Table III.5:** Indexed Powder XRD Pattern for OH2 sandstones

| 2θ(°) | Intensity (a.u) | Mineral | (d$_{hkl}$) cal (Å) | Hkl |
|---|---|---|---|---|
| 20.7427 | 28.70 | Quartz | 4.27880 | 100 |
| 23.4061 | 0.73 | Calcite | 3.79758 | 012 |
| 26.3761 | 100.00 | Quartz | 3.37631 | 101 |
| 28.8459 | 2.72 | Calcite | 3.09260 | 104 |
| 31.3550 | 0.94 | Calcite | 2.85061 | 006 |
| 36.2340 | 5.21 | Quartz, Calcite | 2.47718 | 110 |
| 39.1299 | 6.62 | Quartz, Calcite | 2.30026 | 102/113 |
| 42.6201 | 7.70 | Quartz, Calcite | 2.11962 | 200 |
| 45.8353 | 1.38 | Quartz | 1.97813 | 201 |
| 46.5674 | 7.07 | Calcite | 1.94872 | 024 |
| 49.7343 | 8.53 | Quartz | 1.83180 | 112 |

**Table III.6:** Indexed Powder XRD Pattern for OH3 sandstones

| 2θ(°) | Intensity (a.u) | Mineral | (d$_{hkl}$) cal (Å) | Hkl |
|---|---|---|---|---|
| 20.7974 | 20.79 | Quartz | 4.26767 | 100 |
| 26.5548 | 100.00 | Quartz | 3.35400 | 101 |
| 29.4562 | 0.63 | Calcite | 3.02991 | 104 |
| 36.4127 | 6.46 | Quartz | 2.46543 | 110 |
| 39.3049 | 6.33 | Quartz | 2.29042 | 102 |
| 39.3049 | 6.33 | Calcite | 2.29042 | 113 |
| 40.0686 | 2.36 | Quartz | 2.24851 | 111 |
| 42.2153 | 3.04 | Quartz | 2.13900 | 200 |

| | | | | |
|---|---|---|---|---|
| 45.6785 | 3.08 | Quartz | 1.98455 | 201 |
| 49.9670 | 7.46 | Quartz | 1.82381 | 112 |

**Table III.7:** Indexed Powder XRD Pattern for OH4 sandstones

| $2\theta(°)$ | Intensity (a.u) | Mineral | $(d_{hkl})$ cal (Å) | Hkl |
|---|---|---|---|---|
| 21.8049 | 20.74 | Quartz | 3.26614 | 110 |
| 27.5773 | 100.00 | Quartz | 4.35121 | 121 |
| 28.3848 | 0.15 | Calcite | 4.03710 | 114 |
| 36.4243 | 6.59 | Quartz | 2.46467 | 110 |
| 39.3850 | 5.87 | Quartz, Calcite | 3.28594 | 102/113 |
| 41.1631 | 2.60 | Quartz | 3.24343 | 111 |
| 42.3373 | 4.01 | Quartz | 2.13311 | 200 |
| 45.7306 | 2.34 | Quartz | 1.98242 | 201 |
| 50.0213 | 7.67 | Quartz | 1.82196 | 112 |
| 54.6710 | 0.71 | Quartz | 1.67748 | 202 |

**Table III.8:** Indexed Powder XRD Pattern for OH5 sandstones

| $2\theta(°)$ | Intensity (a.u) | Mineral | $(d_{hkl})$ cal (Å) | Hkl |
|---|---|---|---|---|
| 20.8004 | 24.02 | Quartz | 4.26705 | 100 |
| 22.9420 | 0.50 | Calcite | 3.87335 | 012 |
| 26.5544 | 100.00 | Quartz | 3.35404 | 101 |
| 29.3961 | 0.99 | Calcite | 3.03596 | 104 |
| 36.3215 | 5.72 | Quartz | 2.47141 | 110 |
| 39.2634 | 5.90 | Quartz, Calcite | 2.29274 | 102/113 |
| 40.1582 | 3.07 | Quartz | 2.24369 | 111 |
| 42.3124 | 5.24 | Quartz | 2.13432 | 200 |
| 45.6943 | 3.19 | Quartz | 1.98391 | 201 |
| 50.0022 | 9.24 | Quartz | 1.82261 | 112 |
| 54.6710 | 0.71 | Quartz | 1.67748 | 202 |

**Table III.9:** Indexed Powder XRD Pattern for OH6 sandstones

| $2\theta(°)$ | Intensity (a.u) | Mineral | $(d_{hkl})$ cal (Å) | Hkl |
|---|---|---|---|---|
| 21.7959 | 20.66 | Quartz | 3.26796 | 110 |
| 27.5409 | 100.00 | Quartz | 4.35572 | 101 |
| 36.3311 | 5.40 | Quartz | 2.47078 | 110 |
| 39.2229 | 5.42 | Quartz, Calcite | 3.29502 | 102/113 |
| 41.0931 | 2.53 | Quartz | 3.24719 | 111 |
| 42.2102 | 3.24 | Quartz | 2.13925 | 200 |
| 45.4650 | 1.57 | Quartz | 1.99338 | 201 |
| 47.1227 | 0.23 | Calcite | 1.92704 | 024 |
| 48.5939 | 0.12 | Calcite | 1.87208 | 116 |
| 49.8947 | 7.71 | Quartz | 1.82628 | 112 |
| 54.5556 | 0.76 | Quartz | 1.68075 | 202 |

**Table III.10:** Indexed Powder XRD Pattern for OH**7** sandstones

| $2\theta(°)$ | Intensity (a.u) | Mineral | $(d_{hkl})$ cal (Å) | Hkl |
|---|---|---|---|---|
| 21.7728 | 19.31 | Quartz | 3.27267 | 110 |
| 27.5598 | 100.00 | Quartz | 4.35338 | 101 |
| 31.5260 | 0.12 | Calcite | 2.83554 | 06 |
| 36.4236 | 6.21 | Quartz | 2.46472 | 110 |
| 39.3104 | 5.97 | Quartz, Calcite | 2.29011 | 102/113 |
| 40.0795 | 2.45 | Quartz | 2.24792 | 111 |
| 42.2948 | 4.12 | Quartz | 2.13516 | 200 |
| 43.1512 | 0.69 | Calcite | 2.09475 | 202 |
| 45.7897 | 2.06 | Quartz | 1.97999 | 201 |
| 47.0158 | 0.16 | Calcite | 1.93118 | 024 |
| 48.2627 | 0.23 | Calcite | 1.88415 | 116 |
| 49.8696 | 5.53 | Quartz | 1.82714 | 112 |
| 54.6427 | 1.54 | Quartz | 1.67828 | 202 |

**Table III.11:** Crystalline sizes D for quartz and calcite in OH sandstones and lattice parameters a, c.

| Mineral | Standard lattice parameters (Å) | Calculated lattice parameters (Å) | | | | FWHM (°) | Crystalline sizes (nm) (D) |
|---------|--------------------------------|-----------------------------------|---|---|---|----------|----------------------------|
| | | a | $\Delta a = a_0-a$ | c | $\Delta c = c_0 -c$ | | |
| Quartz | $a_0 = 4.9134$[a] | 4.93206 | -0.0187 | 5.4741 | −0.0689 | 0.18 | 35.44 |
| | $c_0 = 5.4052$[a] | | | | | | |
| Calcite | $a_0 = 4.9890$[b] | 4.99978 | -0.01078 | 16.9761 | 0.0859 | 0.36 | 43.4 |
| | $c_0 = 17.0620$[b] | | | | | | |

[a]data from COD (N° 46–1045)

[b]data from COD (N° 05–0586)

Using the Bragg law, the $d_{hkl}$ inter-planar spacing has been measured from the X-ray diffraction profile:

$$2d_{hkl}\, sin\theta = n\lambda \qquad\qquad\qquad (III.1)$$

We observe that computed values of $d_{hkl}$-spacing (Table III.3, 4, 5, 6, 7, 8, and 9) closely matched those of the standard COD data. From XRD findings and by using the following equation, the lattice constants a, b, and c for the hexagonal phase structure was calculated [14]:

$$\frac{1}{d^2} = \frac{4(h^2+hk+k^2)}{3a^2} + \frac{l^2}{c^2} \qquad\qquad\qquad (III.2)$$

Where (h k l) are the Miller indexes and 'a', 'c' are the lattice constants. The calculated and standard COD lattice constants for quartz and calcite are indicated in Table III.10. As we can see, the calculated lattice parameters for the quartz (a = b = 4.93206 Å and c = 5.4741 Å) and calcite (a = b = 4.99978 Å and c = 16.9761 Å) agree well with the standard values ($a_0$ and $c_0$). We can further calculate the crystallite sizes D of the quartz and calcite of our rocks from the strongest peaks by using Scherrer's formula [20]:

$$D = \frac{0.9\lambda}{\beta cos\theta} \qquad\qquad\qquad (III.3)$$

Where D is the crystallite size, $\lambda$ (=1.5406 Å) is the wavelength of X-rays, $\beta$ is the width full at half maximum (FWHM) of the most intense diffraction peak, usually measured in radian and $\theta$ is the Bragg angle.

The crystallite sizes of quartz and calcite are both less than 100 nm, which makes them of great interest to the nanometric industries and nanotechnologies. The crystallite sizes of

$SiO_2/CaCO_3$ are: D (nm) = 19.94 / 13.85 (rock 1), 35.44 / 43.40 (rock 2), 24.66 / 22.88 (rock 3), 24.79 / 30.75 (rock 4), 33.80 / 38.18 (rock 5), 25.24 / 41.48 (rock 6) and 26.33 / 27.65 (rock 7), respectively.

## III.4 Measurements of $d_{33}$ piezoelectric coefficients in rocks

Figure III.12 shows $d_{33}$ coefficients changes of $SiO_2$ by increasing the proportion of the quartz in the rock samples, where we notice that this coefficient reduces in a linear manner by increasing the proportion of the quartz in four bands, which is an estimated 71% - 72% with 0.05 miles, 72% - 80% with 0.56 miles, 95% - 97% with 0.05 miles and between 97% - 98% with 0.5 miles; which shows that this decrease is faster between the two ratios 97% - 98% and slower between 71% -72% and 95% - 97%.

In the remaining ranges, the coefficient $d_{33}$ decreases increasingly linear by increasing the proportion of quartz between 80% - 91% with 0.005 miles and between 91% - 95% with 8.75 miles; where we note that the latter is faster than the other.

The appearance of a piezoelectric phenomenon in such rocks is not subject to quartz ratio only, the piezoelectric phenomenon can be affected by the presence of other elements as well as calcite, but we believe that the effect of impurities such as Iron (Fe), Aluminum (Al), Silver (Ag), sodium (Na), and Potassium (K) is worth noting. The increase in quartz is supposed to increase the coefficient's value of $d_{33}$, but this does not mean that the coefficient's value of $d_{33}$ will necessarily increase because of the increase in impurities, which can do away with some quartz polarization and therefore decrease the coefficient's value.

In another hand, there is a possibility that the percentage of quartz might affect the increase or decrease in the value of the piezoelectric coefficient.
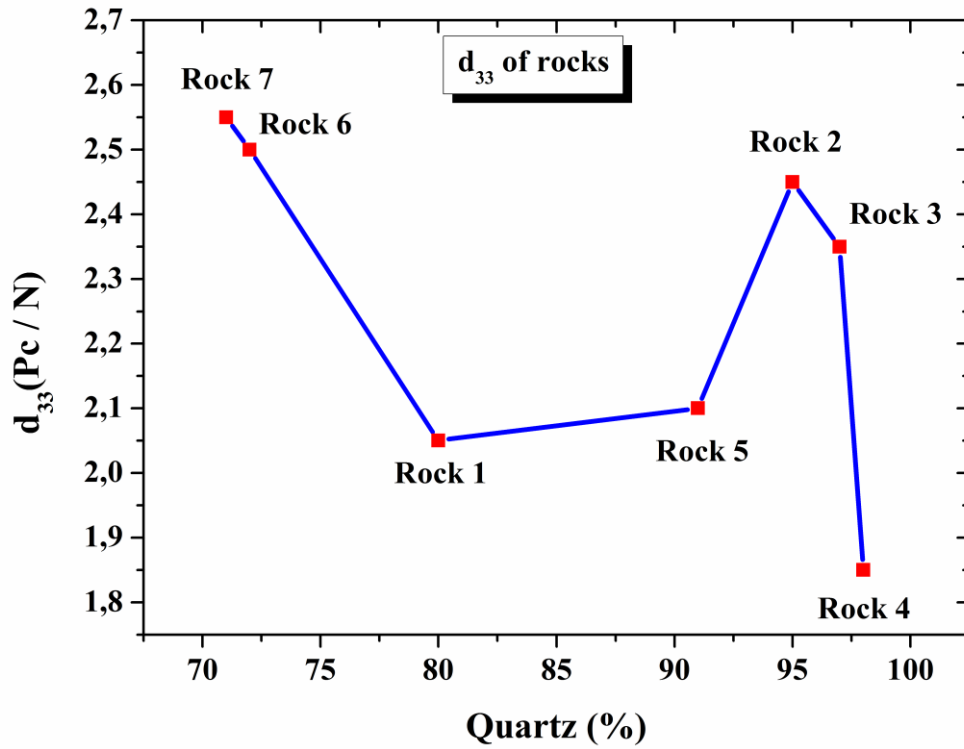
**Figure III.12:** Shows $d_{33}$ coefficients of $SiO_2$ in rocks

According to Table III.11, the strongest piezoelectric coefficients value of crystal quartz is $d_{33} = 2.55 \pm 0.1 Pc/N$ for (71 % of $SiO_2$). There are some differences between our value and the value reported by Bechmann $d_{33}=$ 2.31 $\pm$ 0.1Pc/N [21].

**Table III.12:** Shows $d_{33}$ coefficients of $SiO_2$ in rocks

| Quartz (%) | $d_{33}$(pC / N) |
|---|---|
| 71 % | 2.55 |
| 72 % | 2.50 |
| 80 % | 2.05 |
| 91 % | 2.1 |
| 95 % | 2.45 |

# Reference

# Reference

[1] Reig, F. B., J. G. Adelantado, et al. (2002). "FTIR quantitative analysis of calcium carbonate (calcite) and silica (quartz) mixtures using the constant ratio method. Application to geological samples." Talanta 58(4): 811-821.

[2] Munawaroh, F., L. K. Muharrami, et al. (2019). "Synthesis and characterization of precipitated CaCO3 from ankerite prepared by bubbling method." KnE Engineering: 98–104-198–104.

[3] Saikia, B. J., G. Parthasarathy, et al. (2008). "Fourier transform infrared spectroscopic estimation of crystallinity in SiO 2 based rocks." Bulletin of materials science**31**: 775-779.

[4] Pedersen, B. F. and D. Semmingsen (1982). "Neutron diffraction refinement of the structure of gypsum, CaSO4. 2H2O." Acta Crystallographica Section B: Structural Crystallography and Crystal Chemistry **38**(4): 1074-1077.

[5] Yao, C., A. Xie, et al. (2013). "Green synthesis of calcium carbonate with unusual morphologies in the presence of fruit extracts." Journal of the Chilean Chemical Society **58**(4): 2235-2238.

[6] Anbalagan, G., A. Prabakaran, et al. (2010). "Spectroscopic characterization of Indian standard sand." Journal of applied spectroscopy **77**: 86-94.

[7] Andersen, F. A., L. Brecevic, et al. (1991). "Infrared spectra of amorphous and crystalline calcium carbonate." Acta Chem. Scand **45**(10): 1018-1024.

[8] Mahdadi, N., S. Chihi, et al. (2017). "Chromatic classification of Ouargla (Algeria) dunes sand: determination of main compositions and color causes, by using XRD, FTIR and XRF." Silicon **9**(2): 211-221.

[9] Frost, R. L., J. T. Kloprogge, et al. (2002). "The Garfield and Uley nontronites—An infrared spectroscopic comparison." Spectrochimica Acta Part A: Molecular and Biomolecular Spectroscopy **58**(9): 1881-1894.

[10]Madejová, J. (2003). "FTIR techniques in clay mineral studies." Vibrational spectroscopy **31**(1): 1-10.

[11] Böke, H., S. Akkurt, et al. (2004). "Quantification of CaCO3–CaSO3· 0.5 H2O–CaSO4· 2H2O mixtures by FTIR analysis and its ANN model." Materials Letters **58**(5): 723-726.

[12] Sh. Fu, Q. Lan and J. Yan, Trace element chemistry of hydrothermal quartz and its genetic significance: A case study from the Xikuangshan and Woxi giant Sb deposits in southern China, Ore. Geolo. Rev., 126, 103732 (2020).

[13] Davidson, P. M., G. H. Symmes, et al. (1993). "Synthesis of the new compound CaFe (CO3) 2 and experimental constraints on the (Ca, Fe) CO3 join." Geochimica et Cosmochimica Acta 57(23-24): 5105-5109.

[14] Meftah, N. and M. S. Mahboub (2020). "Spectroscopic characterizations of sand dunes minerals of El-Oued (Northeast Algerian Sahara) by FTIR, XRF and XRD analyses." Silicon 12(1): 147-153.

 [15] Chraibi, S., H. Moussout, et al. (2016). "Utilization of calcined eggshell waste as an adsorbent for the removal of phenol from aqueous solution." Journal of Encapsulation and Adsorption Sciences 6(4): 132-146.

[16] Liu, Y., H. Xu, et al. (2020). "Synthesis of calcite superstructures using water reducer as adjuster." Chemistry Select 5(31): 9709-9713.

[17] Kodeh, F. S., I. M. El-Nahhal, et al. (2020). "Synthesis of CaO–Ag-NPs@ CaCO3 nanocomposite via impregnation of aqueous Sol Ag-NPs onto calcined calcium oxalate." Chemistry Africa 3(3): 679-686.

[18] Weil, J. A. (1984). "A review of electron spin spectroscopy and its application to the study of paramagnetic defects in crystalline quartz." Physics and Chemistry of Minerals 10(4): 149-165.

[19] Weil, J. A. (1993). "A review of the EPR spectroscopy of the point defects in α-quartz: The decade 1982–1992." The Physics and Chemistry of SiO 2 and the Si-SiO 2 Interface 2: 131-144.

[20] Scherrer, P.(1918). Nachrichten von der Gesellschaft der Wissenschaften zu Göttingen, Mathematisch-Physikalische Klasse., 2, 98.

[21] Bechmann, R. (1958). "Elastic and piezoelectric constants of alpha-quartz." Physical review 110(5): 1060.

# Chapter four

## Synthesis and characterization of thin films

## Introduction

In this chapter we have focused on synthesis of thin films using hydrothermal reactor and their characterization, then we discussed their analysis by using infrared spectroscopy (FTIR), scanning electron microscopy (SEM/EDS), x-ray diffraction (XRD) and piezoelectric measurements.

## IV.2 Experimental procedure

## IV.2.1 Synthesis of thin films

Thin films of $CaCO_3/SiO_2$ were produced in a hydrothermal reactor at 150, 200, 250 and 300°C , took place using electric oven for 2 hours. The pulverized rocks having a mass of around 3 mg were immersed for two days at room temperature, around 25°C, in a solution of 3 ml $HNO_3$ and 9 ml HCl (aqua regia). After 48 hours, the solution was extracted and we added 3 mg of serium carbonate ($SrCO_3$) to 15 ml of distilled water after taking only 3 ml of the extracted solution. The solution mixture was placed within a hydrothermal reactor made of stainless steel and equipped with a tiny glass substrate (R217102) with a size of ($75 \times 25 \times 1.1$ mm$^3$). The glass substrates were cleaned with acetone, rinsed with distilled water and dried in the air before to the deposition procedure. While, after deposition, the films were filtered out, let to cool gradually at room temperature and then repeatedly washed in distilled water and acetone. The schematic of synthesis thin films is illustrated in Figure IV.1.
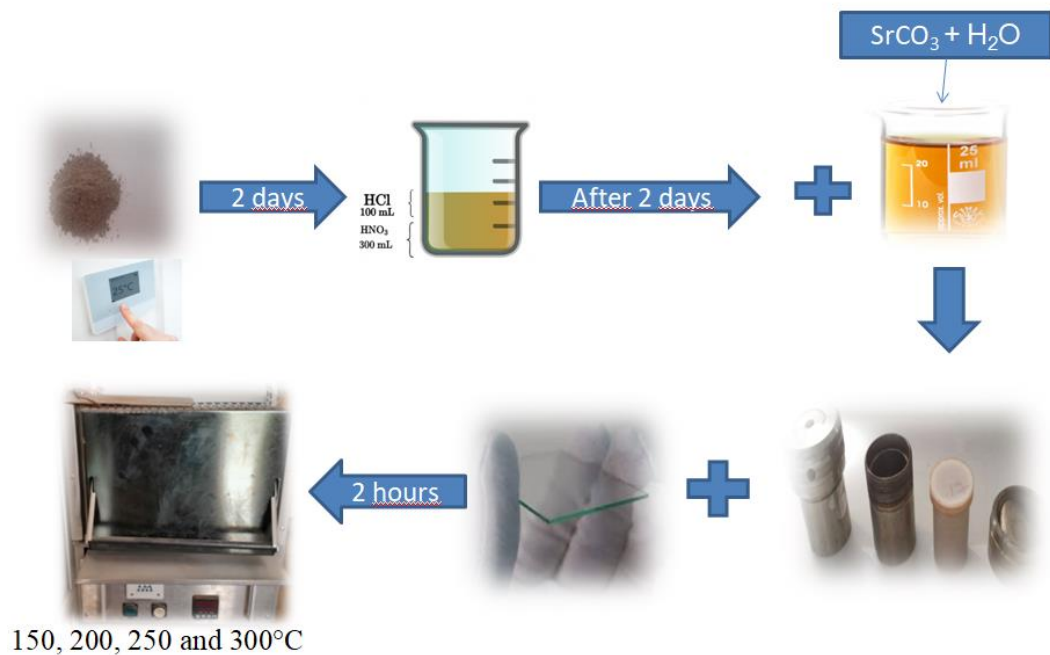


**Figure IV.1:** The schematic of synthesis thin films

One of the disadvantages of hydrothermal synthesis is that it is dark and tightly sealed that is why there is no chance to know the chemical reaction that is happening inside it.

## IV.2.2 Characterization of thin films

The X-ray diffraction BRUKER-binary V3 technique was used to examine the structural characteristics of produced thin films, using $K_\alpha$ radiation from a room temperature copper anticathode ($\lambda$ = 1,5406), running at 35 KV, and 30 mA of electric current. All samples were examined at a step of 0.019 °/s from 20 to 90 °. An Agilente Cary 660 FT-IR spectrometer was used to record the functional group that was present in the sample, between the wavelengths of 4000 to 400 $cm^{-1}$. In order to study the microstructure and elemental composition of our elaborated $CaCO_3$ /$SiO_2$ thin films, SEM-EDS images were obtained using TESCAN VEGA3 electron microscope. Piezoemeter $d_{33}$ device was used to provide the piezoelectric effect in thin films (Figures IV.2 and 3, Annex).

## IV.3 Analysis of synthesis thin films

## IV.3.1 Fourier-Transform Infrared (FT-IR) analysis

Figure IV.4 and Table IV.1 display the FT-IR transmission of the thin films synthesized at different temperature in 400–4000 $cm^{-1}$ range. According to the bands at 428.11, 524.54, and 983.73 $cm^{-1}$ [1, 2, 3, 4] which indicate to quartz bonds, so all thin films contain quartz. The additional distinct peaks for the $CO3^{-2}$ ion at 711.60, 875.52, 1430.92 and 2354.66 $cm^{-1}$ show that calcite is present across the entire thin films [4, 5, 6].

The peaks at 428.11, 524.54 and 983.73 $cm^{-1}$ are attributed, respectively, to Si-O-Fe, Si-O-Al lattice flexing vibrations and bending vibrations [1, 2, 3]. Quartz vibration is responsible for the absorption band at 983.73 $cm^{-1}$ [4]. At 150°C, the absorption band at 2354.66 $cm^{-1}$ is defined; however, the band's mode of motion or vibration was not given [5]. The carbonate ion $CO3^{-2}$'s asymmetrical stretching vibrations are represented by the absorption band at 1430.92 $cm^{-1}$; the band at 875.52 $cm^{-1}$ represents its out-of-plane bending, whereas the band at 711.60 $cm^{-1}$ represents its in-plane bending [4].
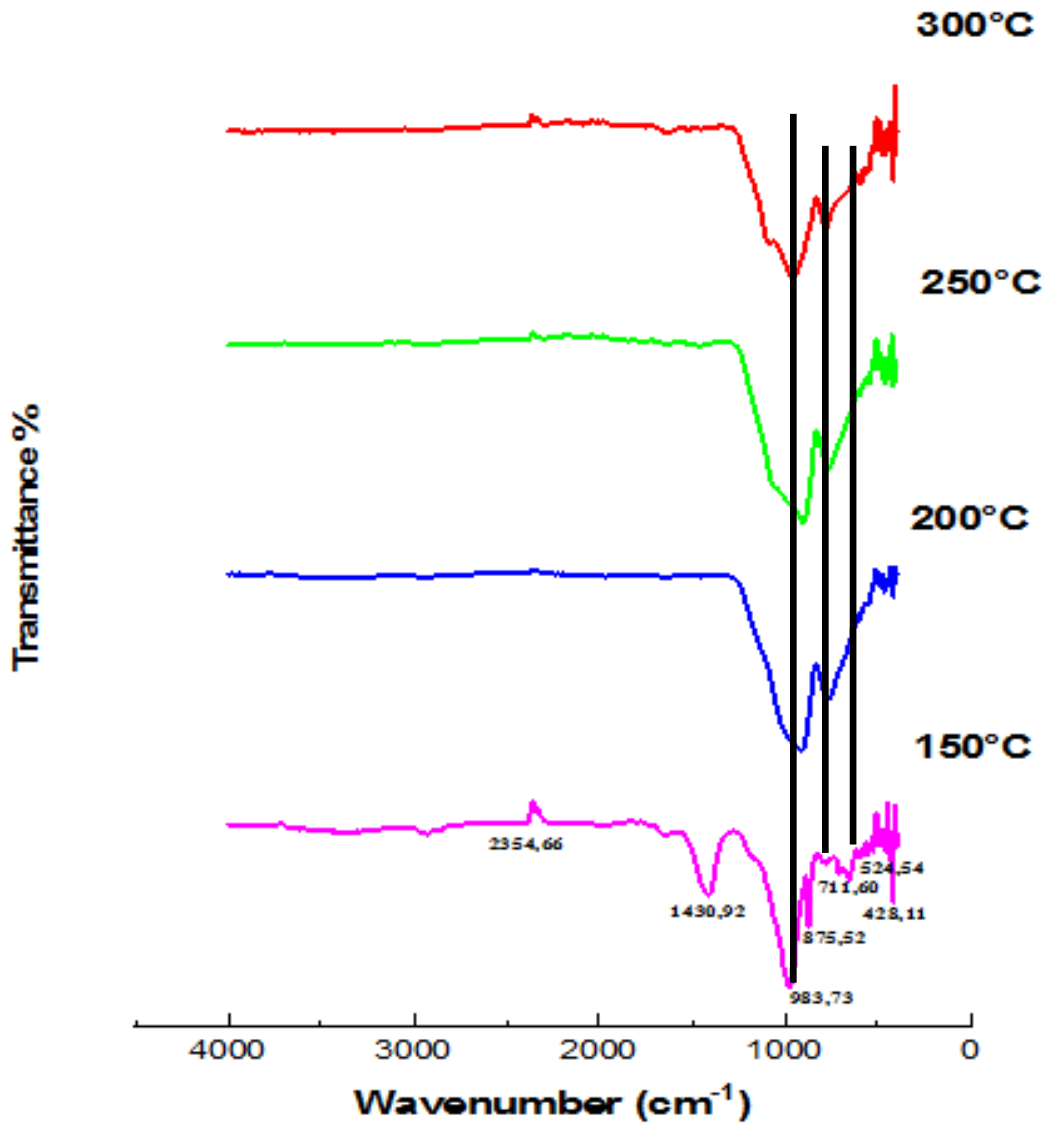
**Figure IV.4:** FTIR transmittion spectrum of our thin films

**Table IV.1:** The primary IR absorption bands of our thin films and the corresponding bond vibration

| Wave number (cm$^{-1}$) | | Assignement |
|---|---|---|
| Calcite | Quartz | |
| | 428.11 | Si-O-Fe bending vibrations |
| | 524.54 | Si-O-Al asymmetrical vibrations |
| 711.60 | | $CO_3^{-2}$ (in-plane bending) |
| 875.52 | | $CO_3^{-2}$(out-of-plane bending) |
| 983.73 | | The vibration of quartz |
| 1430.92 | | $CO_3^{-2}$ A symmetrical stretching vibrations |
| 2354.66 | | Calcite |

## IV.3.2 Microstructural study of thin films

Scanning electron microscopy (SEM) and energy dispersive spectrometric analysis (EDS) are employed to analyze the microstructure of the calcite-quartz thin films and identify the most compact structure.

## IV.3.2.1 Morphological analysis by scanning electron microscope (SEM)

Figures IV.5, 6, 7 and 8 display the surface morphology of the calcite-quartz thin films. In Figures IV.5, 7 and 8 the $CaCO_3$ thin films have three different surface morphologies: thin, wool-like bristles, a circular disk of unknown thickness and scattered bits with an uneven structure, respectively. While the material in $SiO_2$ thin films at 150, 200 and 300°C is in the form of granules and have particles that reflect light that are roughly the same size; at the temperature of 250°C, $SiO_2$ contains a quantity of particles of roughly varying sizes. The NaCl thin films have a consistent particle shape and a soft surface at 200°C. We come to the conclusion that 250°C is the ideal temperature for producing calcite thin films and that temperature affects the shape of our hydrothermally synthesized films.
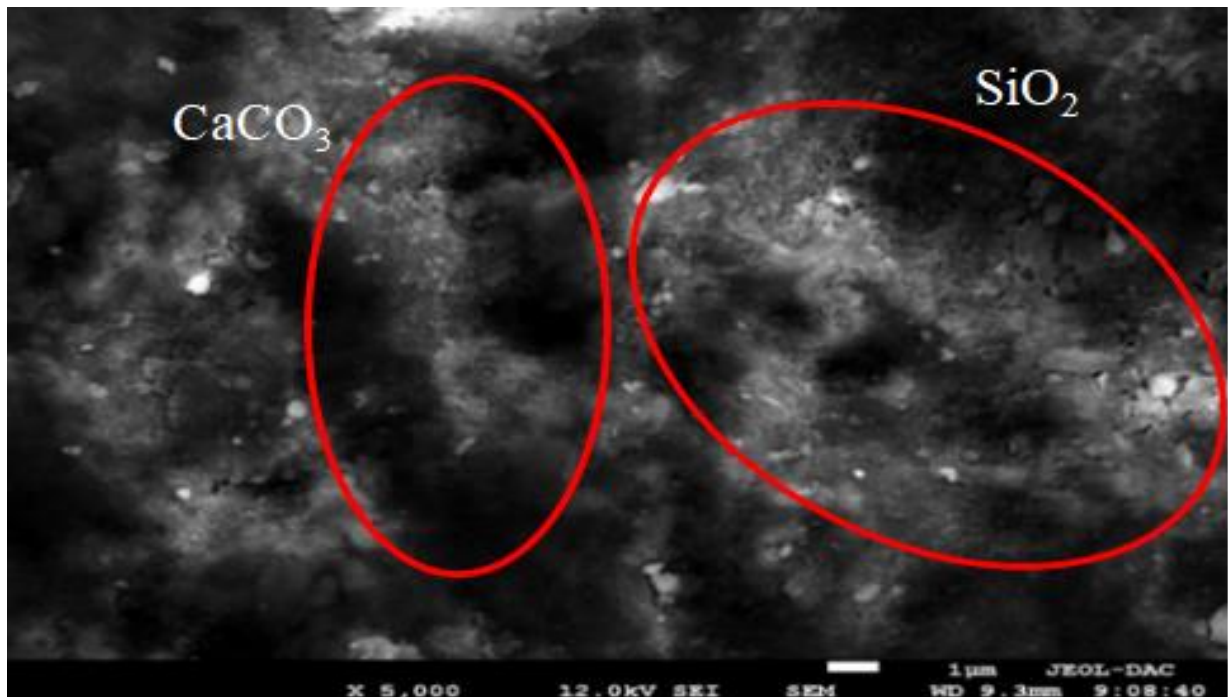


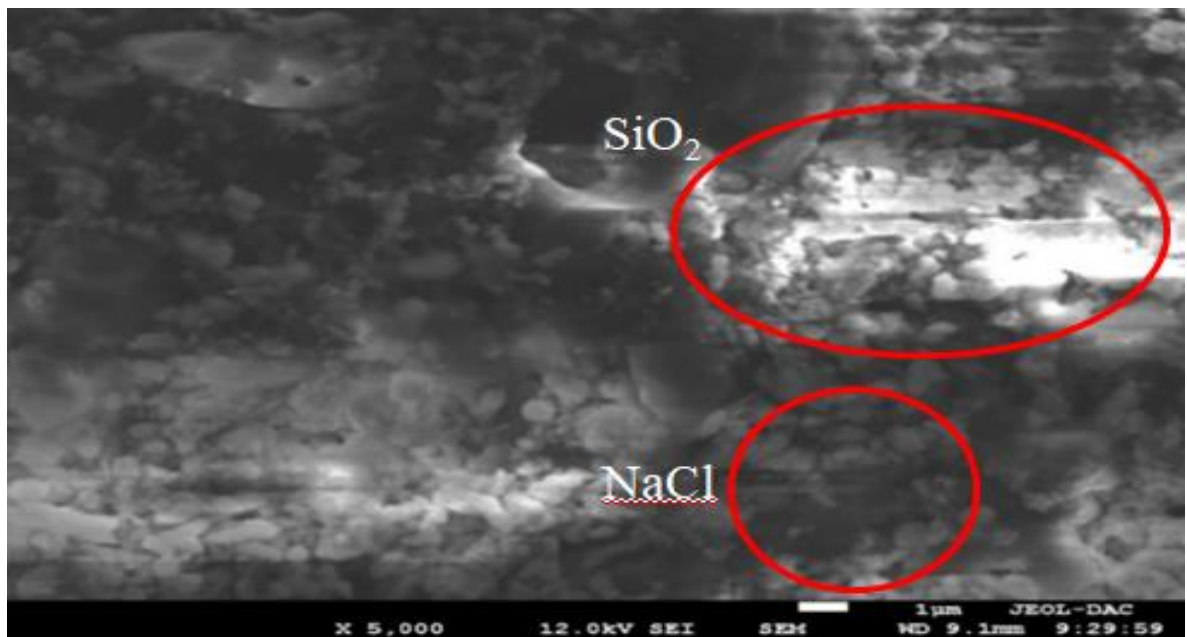**Figure IV.5:** Morphology of thin films at 150°C
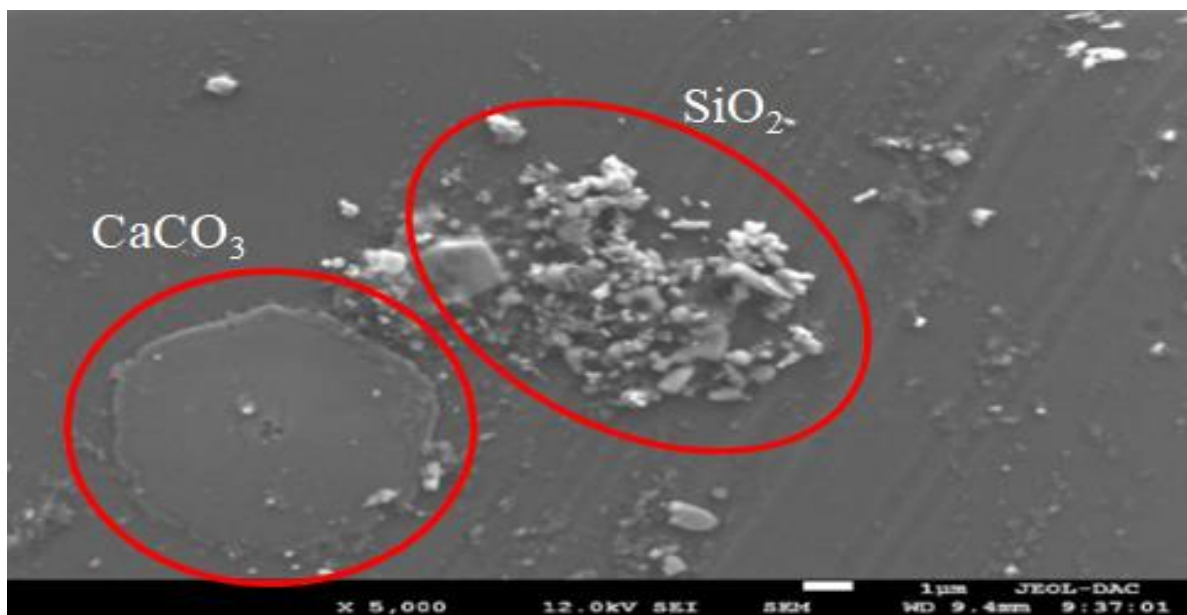
**Figure IV.6:** Morphology of thin films at 200°C



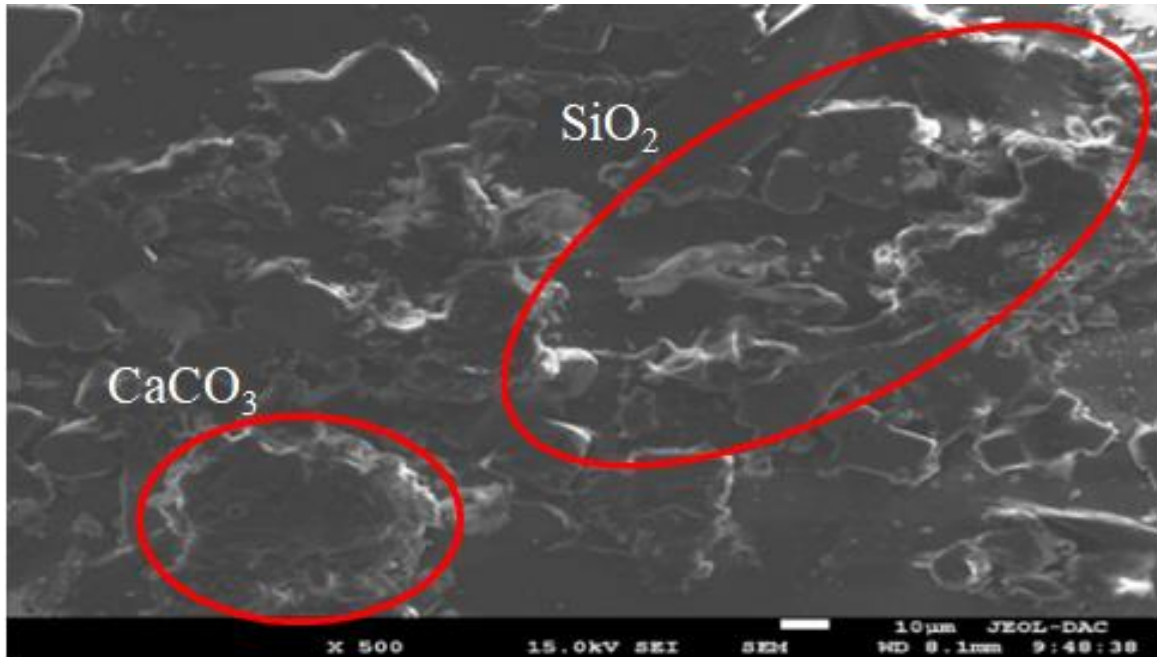**Figure IV.7:** Morphology of thin films at 250°C

**Figure IV.8:** Morphology of thin films at 300°C

## IV.3.2.2 Energy dispersive spectrometric analysis (EDS)

Table IV.2 displayed the representative O, Si, and Ca peaks from the EDS results for thin films, the EDS of the synthetic films is mostly composed of O (68.267%), Si (15.521%), Mg (6.065%), Ca (5.476%), and Al (0.863%), whereas at 200°C, the EDS is composed of O (31.278%), Na (23.156%), Si (16.796%), P (12.351%), Ca (8.576%), Ag (5.168%), Al (2.242%), and Mg (2.546), O (68.594%), Si (11.161%), Na (9.418%), Mg (5.649%), Ca (2.501%), P (1.612%), Ag (0.491%), and Al (0.454%) were the most abundant elements at 300°C.

$CaCO_3/SiO_2$ thin films have comparable peaks that match the spectra of $CaCO_3/SiO_2$, proving that they were successfully formed.

**Table VI.2:** Analysis of the constituents of synthesis thin films

| Thin films | O % | Si % | Ca % | Na % | Al % | Ag % | Mg % | P % |
|---|---|---|---|---|---|---|---|---|
| 150°C | 68.267 | 15.521 | 5.476 | 5.503 | 0.863 | 0.205 | 6.065 | |
| 200°C | 31.278 | 16.796 | 8.576 | 23.156 | 2.242 | 5.168 | 2.546 | 12.351 |
| 300°C | 68.594 | 11.161 | 2.501 | 9.418 | 0.454 | 0.581 | 5.649 | 1.612 |

## IV.3.3 X-ray diffraction (XRD) analysis

Figure IV.9 and Tables IV.3, 4, 5 and 6 show the XRD patterns of the thin films formed at different temperatures. The observed peaks at 150, 250 and 300°C formed the $(CaCO_3/SiO_2)$ with (98/2), (89/11) and (85/15) ratios, respectively which match those in the COD file numbers 00-005-0586 and 00-046-1045. Furthermore, at 200°C formed the $(SiO_2/NaCl)$ with (69/31) ratio with COD file (N° 00-005-0628).

While the temperature of the reaction rose from 150°C to 250°C and then to 300°C, the intense peaks of calcite phases at $2\theta= 29.4104°$ (150°C) shifted to 31.67 due to the trace elements linked to the crystal lattice that were previously reported by SEM-EDS analysis as different types and values, and this may be the slight too to the deformation of the crystal lattice due to the temperature.

The peaks at $2\theta = 39.1435°$ (150°C), 39.3120° (250°C) and 39.5531° (300°C) demonstrate the presence of calcite, as reported in [7, 8], as well as the simultaneous existence of quartz phases, as reported in [9, 10]. In addition, there are peaks for quartz and calcite at 42.3814° (150°C), 42.1829° (250°C), 42.4938° (300°C), 58.9443° (68.7348°C), and 79.6060° (200°C). The thin films also include sodium chloride, at 200°C displays two sharp peaks at $2\theta = (30.7266°$ and 65.1949°). These two peaks, with a = b = c = 5.636176 Å, are caused by the cubic system with the Fm3m symmetry space group as described in the COD (N° 00-005-0628 card) [11]. They are corresponding to the (200) plane and its harmonic (400), respectively. While it appears that excellent crystallization occurs at 150°C based on the fact that peak intensity decreases as reaction heat increases.

With the exception of 200°C, where calcite is absent, the data show the development of thin films of calcite and quartz at various reaction temperatures. It is possible that the quartz/calcite structure has changed, as suggested by the previous analysis (EDS) and this has caused a slight shift in the position of the spectra's explanation due to variations in mineral beads' radii. The presence of specific trace metals in each sample as well as the obvious variances support this.

Quartz has a crystallite size of 113.64 nm (150°C), 116.15 nm (200°C), 101.26 nm (250°C), and 109.07 nm (300°C), while calcite has a crystallite size of 65.68 nm (150°C), 101.98 nm (250°C), and 121.77 nm (300°C), and sodium chloride has a crystallite size of 97.08 nm (200°C), Since the calcite and sodium chloride thin films are of great importance to the nano-metric industries and nano-technologies because they are less than 100 nm at 150°C and

200°C, respectively; even though the fact that at any reaction temperatures, the thin films of calcite and quartz are not nanometric.
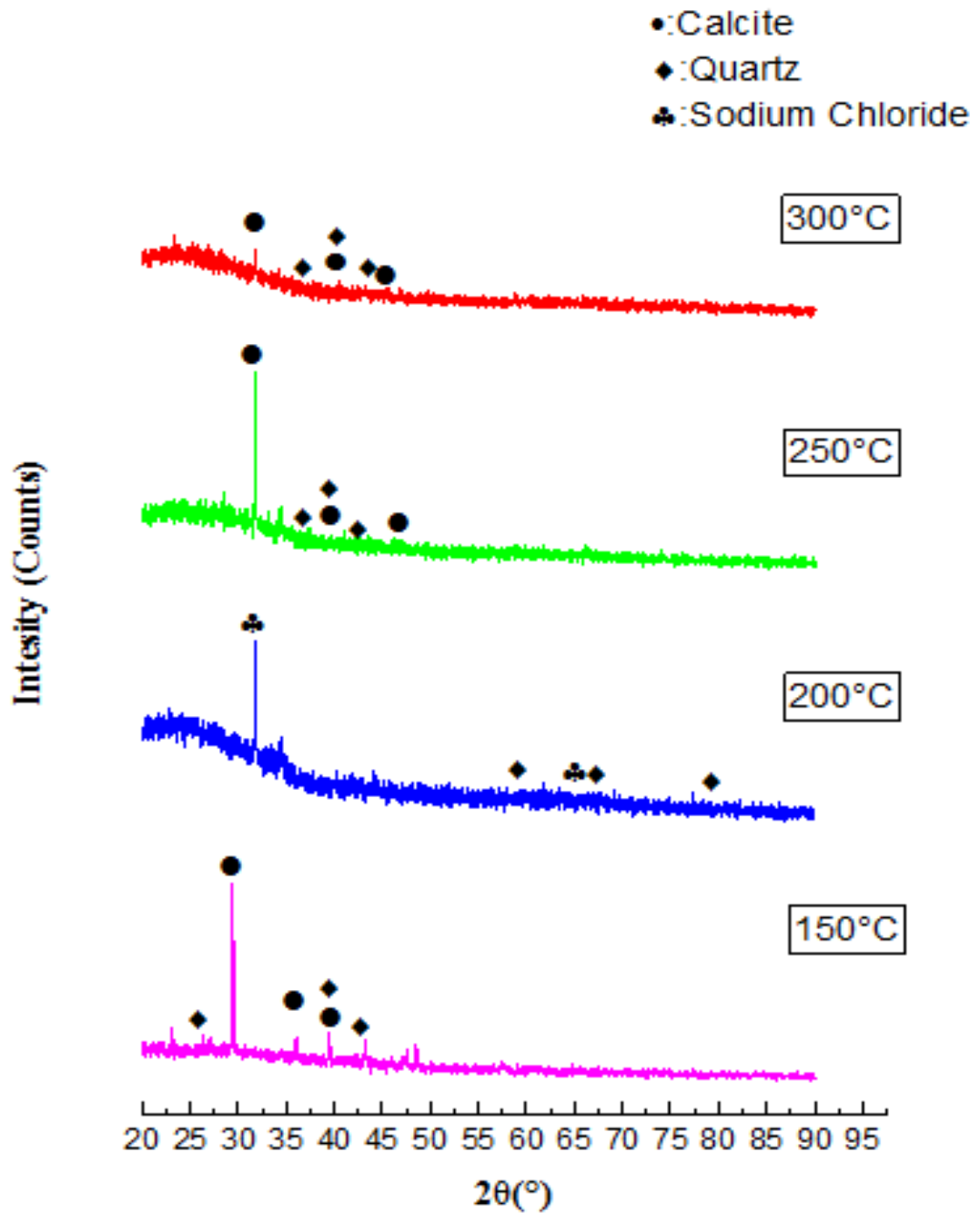


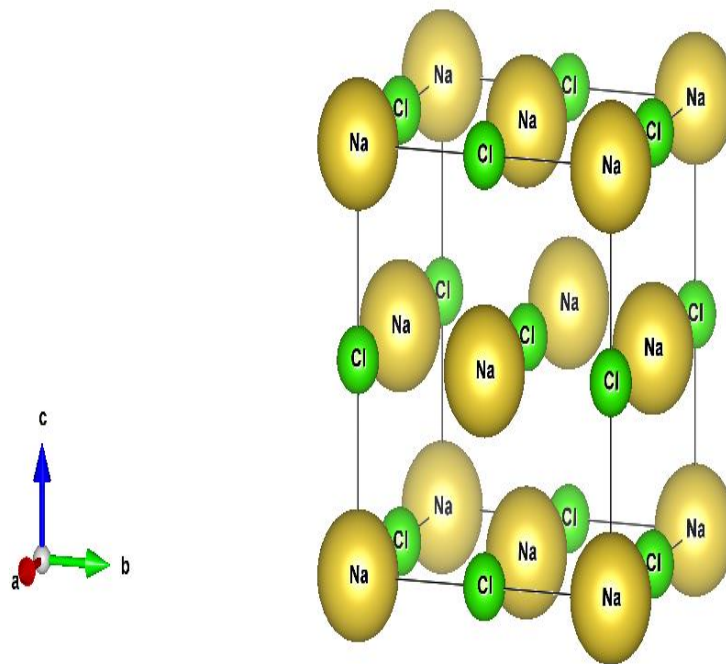**Figure IV.9:** The XRD pattern of our thin films

**Figure IV. 10:** Structure crystalline of NaCl

**Table IV.3:** Indexed Powder XRD Pattern for thin film at 150°C

| 2θ(°) | Intensity (a.u) | Mineral | $(d_{hkl})$ cal (Å) | Hkl |
|-------|-----------------|---------|---------------------|-----|
| 23,1113 | 14,15 | Calcite | 3,84853 | 012 |
| 29,4104 | 100.00 | Calcite | 3,03704 | 104 |
| 31,3741 | 1.82 | Calcite | 2,85128 | 006 |
| 36,0435 | 12.55 | Quartz | 2,48983 | 110 |
| 39,1435 | 16.74 | Quartz, Calcite | 2,28305 | 102/113 |
| 42,3814 | 5.60 | Quartz | 2,13059 | 200 |
| 45,8437 | 4.00 | Quartz | 1,97779 | 201 |
| 47,5811 | 9.76 | Calcite | 1,90954 | 018 |
| 48,5034 | 13.38 | Calcite | 1,87537 | 116 |

**Table IV.4:** Indexed Powder XRD Pattern for thin film at 200°C

| 2θ(°) | Intensity (a.u) | Mineral | $(d_{hkl})$ cal (Å) | Hkl |
|---|---|---|---|---|
| 30.7266 | 100.00 | Quartz | 3.37631 | 100 |
| 40,3373 | 6.55 | Quartz | 2,23600 | 101 |
| 53,8017 | 3.03 | NaCl | 1,70392 | 311 |
| 58,9443 | 8.22 | Quartz | 1,54187 | 211 |
| 65,1949 | 3.56 | NaCl | 1,41035 | 400 |
| 68,7348 | 9.41 | Quartz | 1,38227 | 301 |
| 79.6060 | 2.42 | Quartz | 1.17869 | 213 |

**Table IV.5:** Indexed Powder XRD Pattern for thin film at 250°C

| 2θ(°) | Intensity (a.u) | Mineral | $(d_{hkl})$ cal (Å) | Hkl |
|---|---|---|---|---|
| 20,7419 | 2.20 | Quartz | 4,26219 | 100 |
| 26.8411 | 3.19 | Quartz | 3,34610 | 101 |
| 31,3700 | 4.29 | Calcite | 2,46561 | 006 |
| 39,3120 | 1.95 | Quartz, Calcite | 2,28445 | 102/113 |
| 42,1829 | 3.14 | Quartz | 2,12606 | 200 |
| 47,4759 | 1.93 | Calcite | 1,91353 | 018 |
| 50,2511 | 2.14 | Quartz | 1,81416 | 112 |
| 55,2533 | 4.41 | Quartz | 1,66117 | 103 |
| 57,4651 | 1.27 | Calcite | 1,60238 | 122 |

**Table IV.6:** Indexed Powder XRD Pattern for thin film at 300°C

| 2θ(°) | Intensity (a.u) | Mineral | $(d_{hkl})$ cal (Å) | Hkl |
|---|---|---|---|---|
| 31.3700 | 100.00 | Quartz | 3.37631 | 100 |
| 39,5531 | 7.83 | Quartz, Calcite | 2,46015 | 102/113 |
| 42,9328 | 5.51 | Calcite | 2,09203 | 202 |
| 45,7374 | 5.16 | Quartz | 1,98214 | 201 |
| 47,5698 | 1.70 | Calcite | 1,90997 | 018 |
| 50,1694 | 4.58 | Quartz | 1,81692 | 112 |
| 64,7268 | 4.07 | Calcite | 1,43904 | 104 |
| 65,8243 | 6.64 | Quartz | 1,41768 | 300 |

## IV.4 Measurements of $d_{33}$ piezoelectric coefficients in thin films

Figure IV.11 shows $d_{33}$ coefficients changes of $SiO_2$ by increasing the proportion of the quartz in the thin films that were produced at various temperatures. From this graph we notice that it's only decreasing between 2% - 11% while it's increasing in the two remaining bands, namely 11% - 15% and 15% - 69% by miles 0.01 and 0.001, respectively. We notice that the increase in the first range is faster.

Here quartz crystals may be affected by temperature; specifically when the temperature rises, there is a slight change in quartz structure (in cell constants only without changing its crystal structure).

In rocks we find quartz crystals inappropriately geared, but in thin films the orientation is more proportional, because when we do heat treatment, we also improve the orientation of the crystals and therefore increase polarization, but by raising quartz, this does not mean that the compression coefficient will necessarily increase because of the increase in impurities that can do some polarization. Heat treatment can also corrupt the orientation of crystals, thereby decreasing polarization resulting in a decrease in the coefficient's value of $d_{33}$.
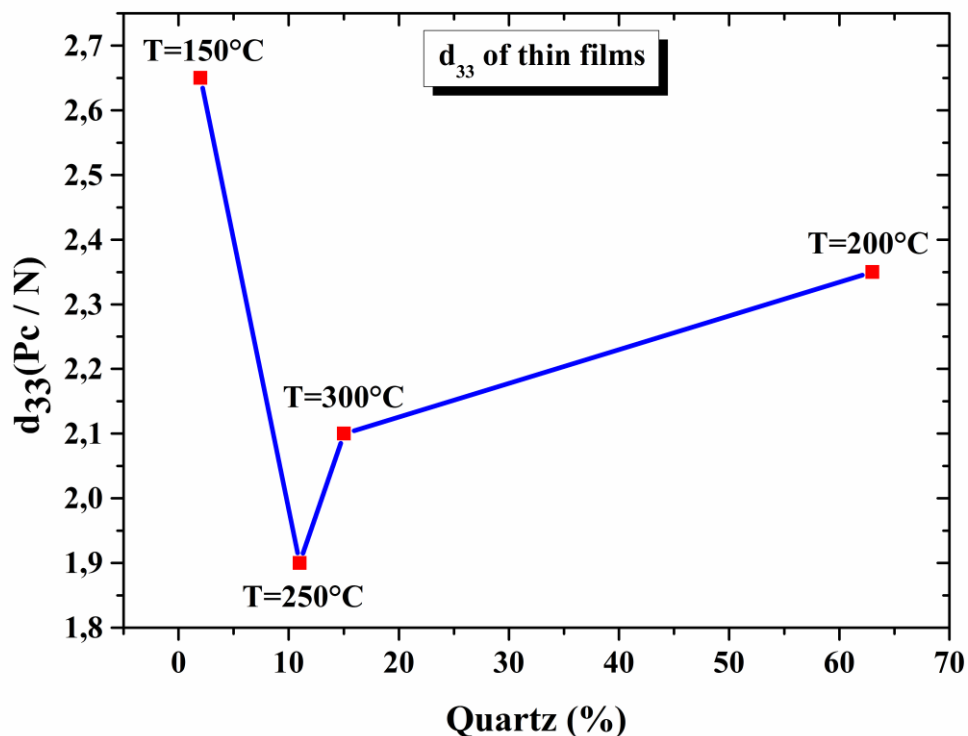


**Figure IV.11:** shows $d_{33}$ coefficients of $SiO_2$ in thin films

From Table IV.7, note that the strongest piezoelectric coefficients value of crystal quartz thin films is $d_{33} = 4.18 \pm 0.1$Pc/N for (69 % of $SiO_2$), there are some differences between our value and the value reported by Bechmann and Zhang $d_{33}= 2.31 \pm 0.1$Pc/N, $d_{33} = 2 \pm 0.5$ pm/V and 4 $\pm$ 2 pC/N, respectivelly [12, 13].

**Table IV.7:** Shows $d_{33}$ coefficients of $SiO_2$ in the thin films

| Quartz (%) | $d_{33}$(pC / N) |
|------------|------------------|
| 2 % (at 150°C) | 4.18 |
| 69 % (at 200°C) | 4.18 |
| 11 % (at 250°C) | 4.06 |
| 15 % (at 300°C) | 4.1 |

# Reference
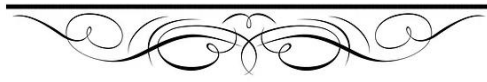
# Reference

[1] Frost, R. L., J. T. Kloprogge, et al. (2002). "The Garfield and Uley nontronites—An infrared spectroscopic comparison." Spectrochimica Acta Part A: Molecular and Biomolecular Spectroscopy 58(9): 1881-1894.

[2] Madejová, J. (2003). "FTIR techniques in clay mineral studies." Vibrational spectroscopy 31(1): 1-10.

[3] Munawaroh, F., L. K. Muharrami, et al. (2019). "Synthesis and characterization of precipitated CaCO3 from ankerite prepared by bubbling method." KnE Engineering: 98–104-198–104.

[4] Sdiri, A., T. Higashi, et al. (2010). "Mineralogical and spectroscopic characterization, and potential environmental use of limestone from the Abiod formation, Tunisia." Environmental Earth Sciences 61: 1275-1287.

[5] Yao, C., A. Xie, et al. (2013). "Green synthesis of calcium carbonate with unusual morphologies in the presence of fruit extracts." Journal of the Chilean Chemical Society 58(4): 2235-2238.

[6] Andersen, F. A., L. Brecevic, et al. (1991). "Infrared spectra of amorphous and crystalline calcium carbonate." Acta Chem. Scand 45(10): 1018-1024.

[7] Kodeh, F. S., I. M. El-Nahhal, et al. (2020). "Synthesis of CaO–Ag-NPs@ CaCO3 nanocomposite via impregnation of aqueous Sol Ag-NPs onto calcined calcium oxalate." Chemistry Africa 3(3): 679-686.

[8] Weil, J. A. (1993). "A review of the EPR spectroscopy of the point defects in α-quartz: The decade 1982–1992." The Physics and Chemistry of SiO 2 and the Si-SiO 2 Interface 2: 131-144.

[9] Benchaa, S., R. Gheriani, et al. (2021). "Structural characterizations of dune sand and construction sand of Sidi Slimane and Zaouia El Abidia areas in the Touggourt region in southeast Algeria." Arabian Journal of Geosciences 14: 1-11.

[10] Hadjadj, K. and S. Chihi (2020). "Rietveld refinement based quantitative phase analysis (QPA) of Ouargla (part of grand erg oriental in Algeria) dunes sand." Silicon: 1-9.

[11] Addala, S., L. Bouhdjer, et al. (2013). "Structural and optical properties of a NaCl single crystal doped with CuO nanocrystals." <u>Chinese Physics B</u> 22(9): 098103.

 [12] Bechmann, R. (1958). "Elastic and piezoelectric constants of alpha-quartz." <u>Physical review</u> 110(5): 1060.

[13] Zhang, Q., D. Sanchez-Fuentes, et al. (2019). "Micro/nanostructure engineering of epitaxial piezoelectric α-quartz thin films on silicon." <u>ACS applied materials & interfaces</u> 12(4): 4732-4740.

# General Conclusion
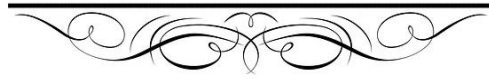
# General Conclusion and prospects

In this thesis, we have studied qualitative and quantitative composition of sandstones collected from Ouargla desert, these samples have been investigated in thin films synthesis by hydrothermal method.

The exanimate parameters in this study was temperature.

All characterization methods were; FT-IR, Raman spectra, EDS-SEM, XRD and Piezometer $d_{33}$ device, whereas software used are: High-Score Plus to identification phases and Vesta program to draw the crystalline structures.

Fourier-transform infrared (FT-IR) spectra showed the characteristic vibration bond peaks for the sandstones and thin films documenting the existence of quartz and calcite, while Raman measurements gave only a rotation of a part containing carbon atoms.

OH sandstones and thin films characterization were found mainly consist of about 86.86%, 9.33% quartz in α-phase, respectively with hexagonal crystal structure with space group P3221 (154), minor calcite mineral (about 13.14%, 90.66%), respectively with a rhombohedral crystal system with space group R3c (167), which has been authenticated by XRD analysis in addition they hold some trace elements (Al, Fe, Na, Ag, K), this indicates a high purity of the quartz and calcite of these sandstones and their thin films.

The most intense peaks are 26.5832 and 29.4104 corresponding to (101) and (104) respectively, these planes indicating the preferential orientation of quartz and calcite growth in these sandstones and thin films, respectively.

XRD has been used for the qualitative and quantitative analysis of multi-component mixtures such as rocks, which is the most commonly used technique.

OH sandstones could be important sources of quartz and calcite which are primary materials for many industrial applications such as glass fabrication, semiconductors and the production of pigments. In addition, rock has a great importance in many fields of science, earth sciences, geophysics and geology.

The crystallite size of quartz and calcite are D = 27.17 nm and 31.17 nm, respectively, demonstrating the nanometric aspect of the OH sandstones.

The variety of sandstones colors is directly related to their chemical composition and the traces of metal they contain.

150°C or less is thought to be ideal for producing nano-scale calcite thin films. At 250°C, calcite was a continuous thin films, cohesive and crystallized, but not on a nano-scale.

Finally, the piezoelectric measurements were well in agreement with those found in the literature. There are some differences in piezoelectric coefficients value of crystal quartz between our value and between value reported.

We may suggest a number of works that need more research and are covered by this work, such as:

After the success of converting the nano-scale raw material ($SiO_2/CaCO_3$) into a non-nano-scale thin films, as a future prospect, we will try to improve the particle size of the thin films to successfully produce them from a natural material by changing the experimental conditions, to make quartz thin films on a nano-scale and with piezoelectric properties from natural precursor rocks known to possess these properties; which can not be used in the industrial and nanotechnology fields, and therefore transform them to thin films can be used. Finding a suitable  application for the sample we produced.

There are numerous errors made during experimental work, including errors related to the environment of the experiment, such as we suspect that some impurities were introduced during sample preparation, or errors related to sample diagnostic conditions, such as issues with XRD, EDS …. brought on by malfunctioning equipment.

From solving the problems presented above, accuracy can be used in the results in order to improve the quality of the thin films and reduce the incidence of impurities for exploitation in several areas, including nanotechnology fields.

Our results can be further identified by experimentation or calculation of other characteristics such as elasticity properties, electrical properties, thermodynamic properties, and others. This addition can relate to each individual rock component or rock in general.
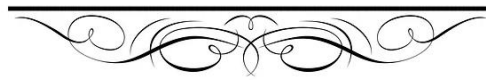
*Annex*

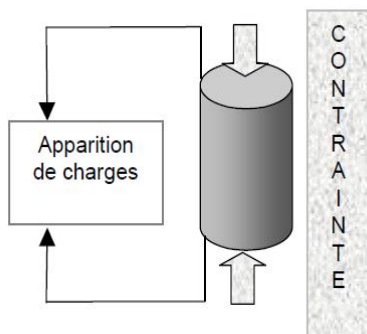**Figure II.4:** The mechanical polishing device used to clean the sample



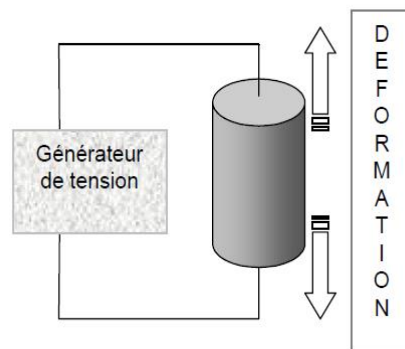**Figure II.5:** The mechanical grinding device used to crush the sample



**Figure II.6 :** Autoclave



**Figure II.7:** Electric oven



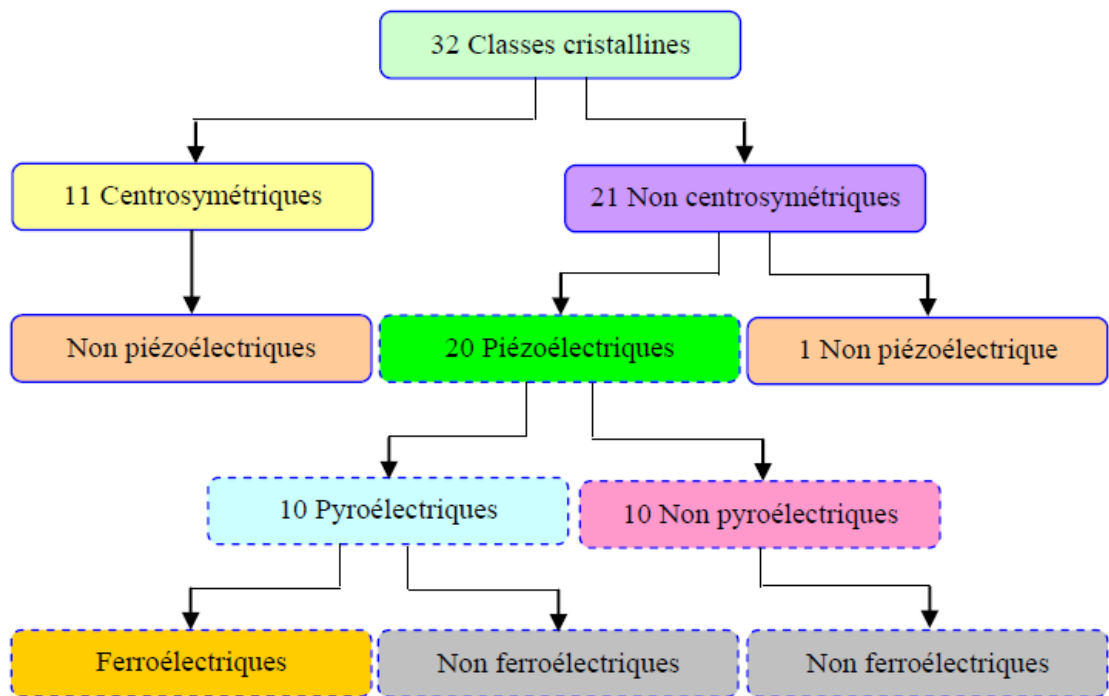**Figure I.22:** Illustration of Piezoelectric Effects

111

**Figure I.23:** Represents the organization of the different crystalline classes



**Figure III.1:** X-ray diffractometer BTX-716

**Figure III.2:** SEM-EDS diffractometer TESCAN VEGA3



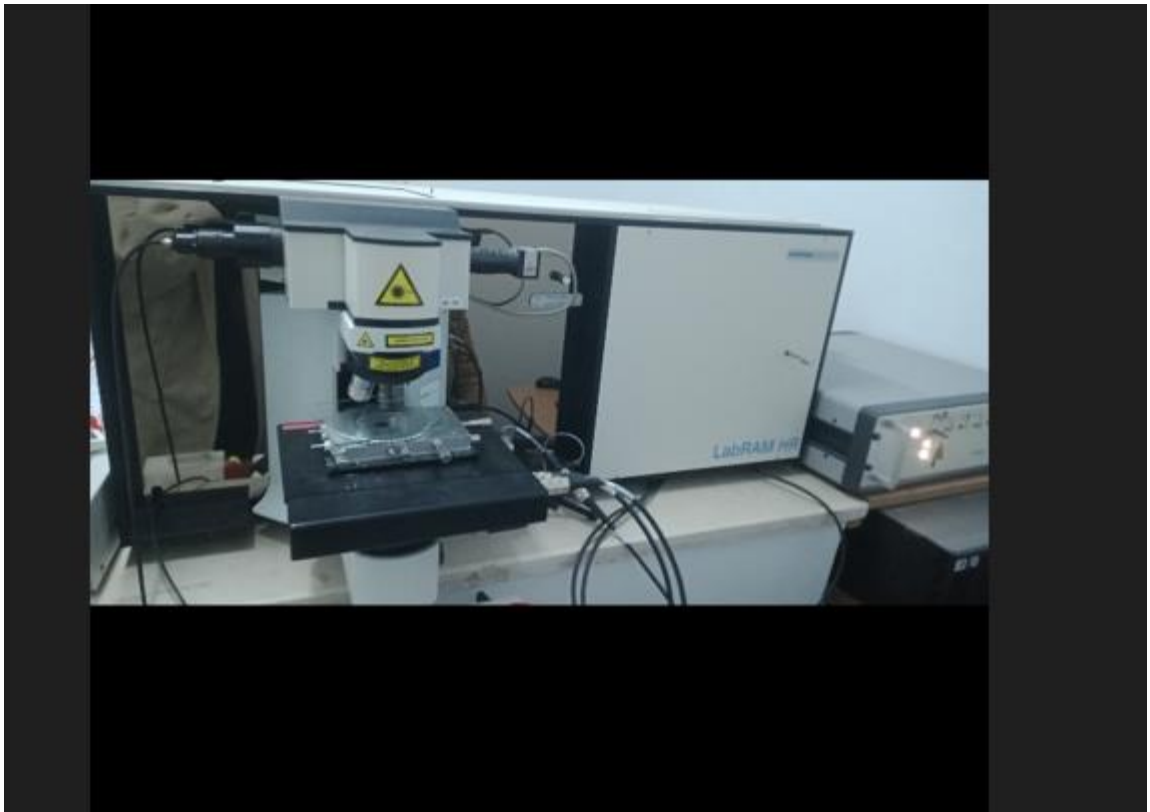**Figure III.3:** Cary 660 FT-IR spectrometer

**Figure III.4:** Raman diffractometer LabRAM HR 800



**Figure III.5 :** Piezometer $d_{33}$device

**Figure IV.1:** X-ray diffractometer BRUKER-binary V3



**Figure IV.2:** SEM-EDS diffractometer TESCAN VEGA3